

A Thesis for the Degree of Ph.D. in Engineering

**Anomalous dynamics of water molecules around
cell membranes: Molecular dynamics simulation
study**

March 2016

Graduate School of Science and Technology
Keio University

Eiji Yamamoto

©2016
Eiji Yamamoto
All Rights Reserved

Acknowledgment

I first met my supervisor, Professor Kenji Yasuoka, through his class on computational simulations. In his class, he looked extremely serious, so I had a preconception that he would be difficult to converse with, which made me keep my distance from him. When I had to select a laboratory to do my bachelor thesis, I had already decided to acquire a Ph.D. degree. At first, I visited numerous laboratories except for Yasuoka laboratory. I could not find a lab that was intriguing to me. Coincidentally, I browsed through his research topics on his website, and then I decided to visit his group. His lab was my first and last choice. After talking with him at length, my negative image about him disappeared, and my realization of him became positive. I was sure that I wanted to get my Ph.D. from his group, which meant the next 6 years of my future would be set. I would like to express my deepest gratitude for his continuous academic and financial support. I learned not only about research but I also grew in character. Life in the lab was very exciting. For example, one day he asked me “Do you want to go to Russia?” I said “yes.” Six months later, I was giving an oral presentation at the Joint Institute of Nuclear Research in Dubna, Russia, which is surrounded by a forest, where many wild dogs lived, and people drank vodka. Since I had already decided to get my Ph.D., in accordance with Professor Yasuoka’s education philosophy, I had to find my own research topic once I completed the first research theme on general anesthesia, which was initially given to me. He implicitly made me aware of the qualities that I lacked about myself. Thanks to Professor Yasuoka, I was able to continue my research freely and vigorously without any constraints.

I also express my deepest gratitude to Project Associate Professor Takuma Aki-moto. He joined Yasuoka laboratory at the same time as me, and we have collaborated in many research topics. I learned the basic skills as a researcher and became interested in physics thanks to him. The turning point in my young research career was at a celebratory party after my bachelor’s thesis defense. At that time, I had

almost finished the first research theme that was given to me from Professor Yasuoka, and I had yet to find my next research topic on my own. Dr. Akimoto told me “I think you should not stay on this path. You must read many papers if you want to become a good scientist. If not, you can only do what you are told”. After that talk, I started to read various journals every week.

I would also like to thank Professor Masato Yasui in the department of pharmacology for valuable discussions and encouragement on my research. He was the person that made me realize to love water in biological systems. I also acknowledge Dr. Yoshinori Hirano in RIKEN for the support in starting my MD simulations.

Furthermore, I extend my gratitude to all of the past and present laboratory members. I especially would like to thank Assistant Professor Noriyoshi Arai in Kinki University, Dr. Daisuke Takaiwa, Mr. Winarto, Mr. Katsufumi Tomobe, and Mr. Kento Inoue for research collaborations. Moreover, I spent long time in the laboratory with Mr. Kentaro Nomura, Mr. Takuma Nozawa, and Mr. Daisuke Yuhara. They made my laboratory life enjoyable. I also express my gratitude for Dr. Donguk Suh, Dr. Taizo Shibuya, and Dr. Masaki Hiratsuka. When I was down and discouraged, they brightened my day. We chatted many times.

The six month experience in 2015 at the University of Oxford was very stimulating. I am very grateful to Professor Mark S. P. Sansom, Dr. Antreas C. Kalli and everyone else in his group. I could learn biological approaches and the importance of conducting research globally. I also thank Japanese scientists in the monthly OJARU meeting in Oxford. I was able to share my woes living overseas. Particularly, from Dr. Seiji Ura, I learned how to improve the taste of *ankou-nabe* using the cabbages there instead of the original Chinese cabbage, which was unobtainable.

I wish to thank my thesis examining committee members: Professor Youhei Fujitani, Professor Koji Fukagata, and Assistant Professor Keita Ando, for their thorough comments.

I acknowledge the support by MEXT Grant-in-Aid for the Program for Leading Graduate Schools “Global Environmental System Leaders (GESL) Program”, Keio University Program for the Advancement of Next Generation Research Projects, and Japan Society for the Promotion of Science (JSPS).

And finally, I would like to express my great thanks to my parents, Machiko and Taku, for their encouragement and unending support.

Abstract

Water molecules play important roles in maintaining the cell membrane functions and providing unique environments for biological reactions on cell membranes. In this study, all-atom molecular dynamics simulations were performed to investigate the dynamics of water molecules around cell membrane surfaces.

Firstly, we showed that temperature dependencies of water translational and rotational motions near a membrane surface are different from those in bulk. Decreasing temperature enhances the water retardation on the membrane surface, and the lateral motions of water molecules are correlated with the vertical motions. Next, we found anomalous dynamics of water molecules on membrane surfaces. The translational and rotational diffusion of water molecules on the membrane surfaces exhibit subdiffusion and aging. The anomalous diffusion is attributed to both divergent mean trapping time (continuous-time random walk) and long-correlated noise (fractional Brownian motion). Moreover, we found that hydration dynamics on the lipid membranes exhibits $1/f$ noise. Constructing a dichotomous process for the hydration dynamics, we provided an evidence that the origin of the $1/f$ noise is a combination of a power-law distribution with cutoff of interoccurrence times of switching events and a long-term correlation between the interoccurrence times. Finally, water permeation through an Aquaporin, which exclusively permeates water molecules across cell membranes and regulate the osmotic pressure of the cell, was investigated. Analyzing the effects of the conformational fluctuations of amino acids on water permeation, we found that $1/f$ fluctuations of amino acids generate non-Poisson water permeation in AQP1.

These results provide new insights on the water molecules that play important roles for the function of cell membranes.

Contents

Acknowledgment		i
Abstract		iii
Chapter 1	Introduction	1
1.1	Cell membrane	1
1.2	Water molecules around lipid membranes	2
1.3	Aquaporin	6
1.4	Thesis objective and outline	9
Chapter 2	Computational methods: Molecular dynamics simulation	10
2.1	Numerical integration	10
2.1.1	Verlet algorithm	10
2.1.2	Velocity-Verlet algorithm	11
2.2	Constrained molecular dynamics simulation	11
2.2.1	SHAKE algorithm	12
2.2.2	RATTLE algorithm	13
2.3	Control of pressure and temperature	14
2.3.1	Berendsen's algorithm	15
2.4	Boundary condition	16
2.5	Force and potential	16
2.5.1	Bonded interaction	17
2.5.2	Non-bonded interaction	19
Chapter 3	Temperature dependence of water dynamics near membrane surfaces	21
3.1	Introduction	21
3.2	Methods	23
3.3	Results and Discussion	26

3.3.1	Residence of water molecules on the POPE membrane surface	26
3.3.2	Diffusivities of water molecules near the POPE membrane surface	27
3.3.3	Rotational motion of water molecules near the POPE membrane surface	32
3.3.4	Anomalous diffusion of water molecules on the POPE membrane surface	35
Chapter 4	Anomalous diffusion of water molecules on membrane surfaces	37
4.1	Introduction	37
4.2	Methods	41
4.3	Results and Discussion	42
4.3.1	Diffusion of water molecules on membrane surfaces	42
4.3.2	Translational and rotational subdiffusion of water molecules on membrane surfaces	46
4.3.3	Origin of subdiffusive motion of water molecules on membrane surfaces	49
Chapter 5	$1/f$ noise in hydration dynamics on lipid membrane surfaces	60
5.1	Introduction	60
5.2	Methods	61
5.2.1	Molecular dynamics simulations	61
5.2.2	Degree of non-Markovianity	62
5.3	Results and Discussion	62
5.3.1	Fluctuations of water molecules on the lipid head group	62
5.3.2	Origin of the $1/f$ noise	66
Chapter 6	$1/f$ fluctuations of amino acids regulate water permeation in AQP1	80
6.1	Introduction	80
6.2	Methods	81
6.2.1	Molecular dynamics simulations	81
6.2.2	Detrended fluctuation analysis	82
6.3	Results and Discussion	84
6.3.1	Fluctuations of amino acids in AQP1	84

6.3.2	Water dynamics within AQP1	85
6.3.3	Stochastic model of water permeation	89
Chapter 7	Conclusion	92
	Abbreviations and symbols	95
	Appendix	96
	References	98

List of Figures

1.1	Schematic diagram of the cell membrane	3
1.2	Structure of phospholipids	4
1.3	Snapshot of interfacial water on the POPC lipid membrane by MD simulation	5
1.4	Structure of aquaporins	7
2.1	Boundary condition	16
2.2	Schematic diagram of bonded interactions	17
2.3	Van der Waals potential	20
3.1	Schematic view of the simulation system	24
3.2	Area per lipid at different temperature	25
3.3	Residence of water molecules on the POPE membrane surface	27
3.4	Translational motion of water molecules near the POPE membrane surface (mean exit times in the case $L^2 = 0.5 \text{ nm}^2$)	29
3.5	Differences of translational motion of water molecules between the first layer and bulk	30
3.6	Mean exit times in the case $L^2 = 0.1 \text{ nm}^2$	31
3.7	Rotational motion of water molecules on the POPE membrane surface	33
3.8	Differences of rotational motion of water molecules between the first layer and bulk	33
3.9	Ensemble-averaged MSD of water molecules in the first layer	36
4.1	Schematic view of observing the aging process	38
4.2	Diffusion of water molecules on lipid membrane surfaces	44
4.3	Residence of water molecules on membrane surfaces	45
4.4	Subdiffusion and aging of water molecules on membrane surfaces	47

4.5	Ensemble-averaged MSDs of water molecules with different measurement starting times	48
4.6	Quantitative analysis of trajectories of water molecules on the POPC membrane surface	50
4.7	Quantitative analysis on trajectories of water molecules on the POPE membrane surface	51
4.8	Translational and rotational TAMSDs of water molecules on the POPC membrane surface	53
4.9	Translational and rotational TAMSDs of water molecules on the POPE membrane surface	53
4.10	Mean TAMSDs	54
4.11	Relative standard deviation of TAMSDs	55
4.12	Equilibration of the systems	57
4.13	Exit times of water molecules	58
5.1	Fluctuation of number of water molecules on the POPC membrane	64
5.2	Ensemble-averaged PSD of number of water molecules in regions near the POPC membrane surface	65
5.3	$1/f$ noise in dichotomous process on the POPC membrane	67
5.4	Alternating renewal process	68
5.5	Correlation between residence times on the POPC membrane	70
5.6	$1/f$ noise in the hydration dynamics on the POPC membrane with using different hydrogen bond distance 0.3 nm	72
5.7	$1/f$ noise in the hydration dynamics on the POPE membrane	73
5.8	$1/f$ noise in the dichotomous process on the POPE membrane	74
5.9	Correlation of residence times on the POPE membrane	75
5.10	$1/f$ noise in the hydration dynamics on the POPC/POPS membrane	76
5.11	$1/f$ noise in the dichotomous process on the POPC/POPS membrane	77
5.12	Universality of the hydration dynamics with different force field, thermostat, and barostat	78
5.13	Ensemble-averaged PSD of temporal fluctuations of perpendicular position of lipid molecules in the POPC membrane	79
6.1	The system used for MD simulations of AQP1 in a POPE lipid bilayer	81
6.2	Fluctuations of amino acids in AQP1	85

6.3	Water permeation in AQP1	87
6.4	Restrained MD simulations of AQP1	88
6.5	Stochastic model of water permeation in AQP1	91

List of Tables

3.1	The factor of the orientational correlation function fitting curves of water molecules: (τ'_i, τ_i, A_i)	34
4.1	Summary of confirming the origin of subdiffusive motions	56

Chapter 1

Introduction

1.1 Cell membrane

The cell membrane, also known as the plasma membrane or cytoplasmic membrane, is a biological membrane which is mainly composed with lipid molecules and membrane proteins [see Fig. 1.1]. The cell membrane surrounds the cell and controls the interior environment segregating the intracellular environment from the extracellular environment. It is involved in a variety of biological process such as molecular transport, energy conversions, biological reactions, membrane remodeling, and cell signaling. Lipid molecules and membrane proteins have diffusivities in the cell membrane [1], where encounter and interaction of these biomolecules result in physiological control of cell functions.

The most abundant component in cell membranes is phospholipids [2], which have a single hydrophilic head group (glycerol, phosphate, and choline) and two hydrophobic hydrocarbon tails [see Fig 1.2]. The amphipathic lipids spontaneously aggregate and form micelles or liposomes depending on conditions, where hydrophilic head group interacts with aqueous environment and with each other, and hydrophobic tails are isolated from water. The lipid bilayer, which constitutes the cell membrane and intracellular organelle membranes, works as a barrier rejecting the permeation of hydrophilic solutes across the membrane but accepting the permeation of hydrophobic solutes [3–6]. Lipids adopt fluid and gel phases, which are characterized by a different spatial freedom of each lipid with respect to its neighbors. The rheological properties of the lipid membrane enable coexistence of fluidity and rigidity: the former is essential for the membrane protein assemblies and trafficking, and the latter for stabilizing the structure of the lipid bilayer. Although the mechanical properties of phospholipid monolayers have been investigated by microrheology

experiments [7, 8], for the limited experimental window the rheological properties of lipids have been controversial, viscosity [7, 9] or viscoelasticity [8, 10, 11]. Single particle tracking can characterize the rheological properties of a medium if the diffusion process is characterized by time-dependent memory function [12], i.e. the current state is influenced by the past state. Single particle tracking of lipid bilayers using simulations has shown the viscoelastic feature [13, 14].

The lipid composition is different between intracellular organelles. The tail is made of fatty acids, and length is varied (number 14-24 carbons). Typically one of two contains cis-unsaturated fatty chains of varying lengths, and the other is saturated fatty chains. There are more than 1000 kinds of lipids in a variety of combinations of hydrophilic head group and hydrophobic tails. The lipids are mainly sorted into three types: phospholipid, cholesterol, and glycolipid. The main composition of lipids in mammalian cell membranes is glycerophospholipids such as phosphatidylcholine (PC), phosphatidylethanolamine (PE), and phosphatidylserine (PS) [see Fig. 1.2]. The other important compositions of the membrane are sphingomyelin (SM) and cholesterol. These two lipids are concentrate in the lipid raft domain [15]. The laterally segregated nanoscale domain also contains many proteins which have function in membrane signaling and trafficking. The acyl chains of lipids are accommodated in hydrophobic pockets of transmembrane proteins and contribute to the protein function via protein lipid interactions, e.g. structural stability, regulating channel opening and closing, and controlling the oligomer of protein complexes [16, 17]. Lipids can act as not only second messengers but also regulator of the function of transmembrane proteins.

1.2 Water molecules around lipid membranes

Approximately 70 % of human body is filled with water. Water in biology is not a simple solvent but plays more active and essential roles with biomolecules in complex and subtle ways [18, 19]. The function of biomolecules depends on the structure and dynamics of the hydration shell. Moreover, disruption of such interfacial water, which reflects the abnormality of the well-balanced system, can be used as a biomarker of diseases [20, 21].

Water molecules around the lipid membranes are believed to be playing important roles in biological reactions and maintaining the cell functions, which are affected by the structure and dynamics of water molecules in the hydration layer

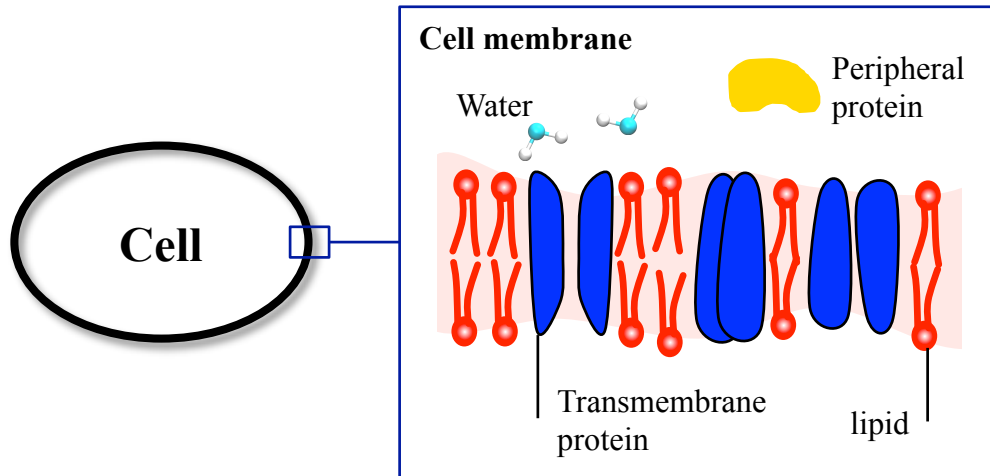


Fig. 1.1 Schematic diagram of the cell membrane.

of membranes [22–24]. The properties of the water molecules have been studied by variety of experimental techniques, e.g. X-ray [25], nuclear magnetic resonance (NMR) [26–28], neutron scattering techniques [28, 29], infrared spectroscopy [30–33], terahertz time-domain spectroscopy (THz-TDS) [33–35], pump-probe spectroscopy [36], Overhauser dynamic nuclear polarization (ODNP) NMR relaxometry technique [37–39], and vibrational sum frequency generation spectroscopy [40–44]. Unique properties of water have been found in the interfacial region up to 1.2 nm away from the membrane surfaces. Various types of spectroscopy studies suggested inhomogeneous water structures at lipid interfaces [27, 30, 31, 33, 36], and those are weakly aligned by charges on the lipid head group [41–44]. These spectra reflect the difference in orientation and hydrogen bond network on negatively charged phosphate, positively charged choline, and hydrophobic region of the lipid [43].

About the translational diffusivity, ODNP NMR relaxometry technique enables to measure the diffusivity of interfacial water within ~ 1 nm around nitroxide radical-based spin labels located at the molecular surface [37–39], and revealed that it is slower than those in bulk. The dynamics of the interfacial water can be also detected experimentally by neutron scattering and NMR [28, 29]. Because the time scale of the experiment is 10^{-9} – 10^{-11} s, only interfacial water molecules strongly interacting with lipids are observed: the time scale of rotational relaxation is 10^{-10} s order and diffusion constant is 10^{-9} m²/s order [29].

To interpret the molecular mechanism of experimentally observed phenomena and investigate more microscopic dynamics of molecules, molecular dynamics (MD)

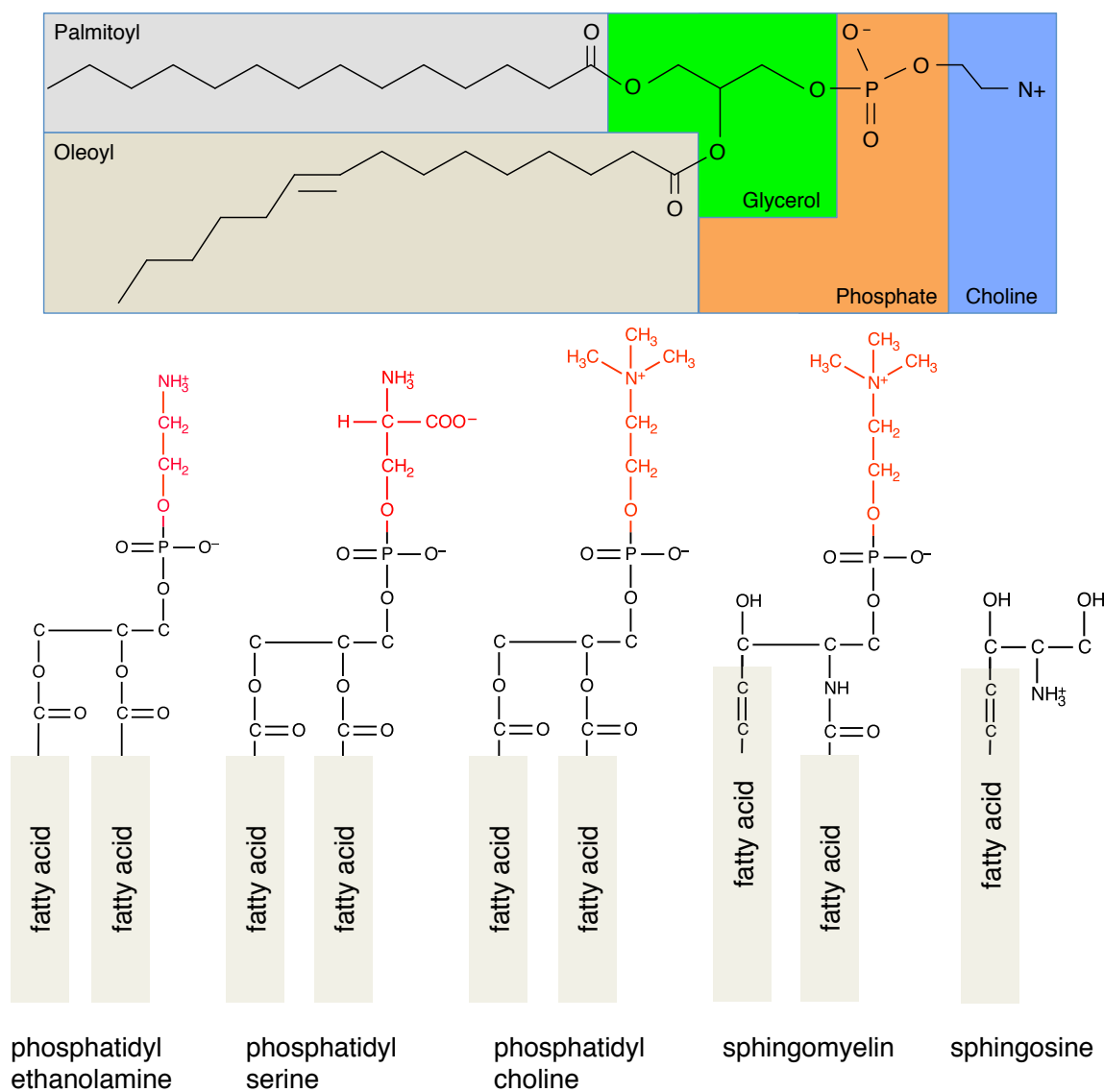


Fig. 1.2 Structure of phospholipids.

simulation can be a powerful computational tool [45, 46]. In particular, this *in silico* approach on water molecules around membranes is in qualitative agreement with the experimentally observed band spectrum [47–50]. Solvent structure around lipid head group regions is different from that in bulk [51–53]. The formation of a clathrate-like shell is observed for the hydrophobic PC head group but not for hydrophilic PE head group. In self-assembled lipid structures such as vesicles, liposomes, and plasma membranes, water molecules form a bridge that connects lipid molecules [54, 55]. Approximately 70 % of lipid molecules are linked by the water bridge, where approximately 70 % of the intermolecular water bridges are

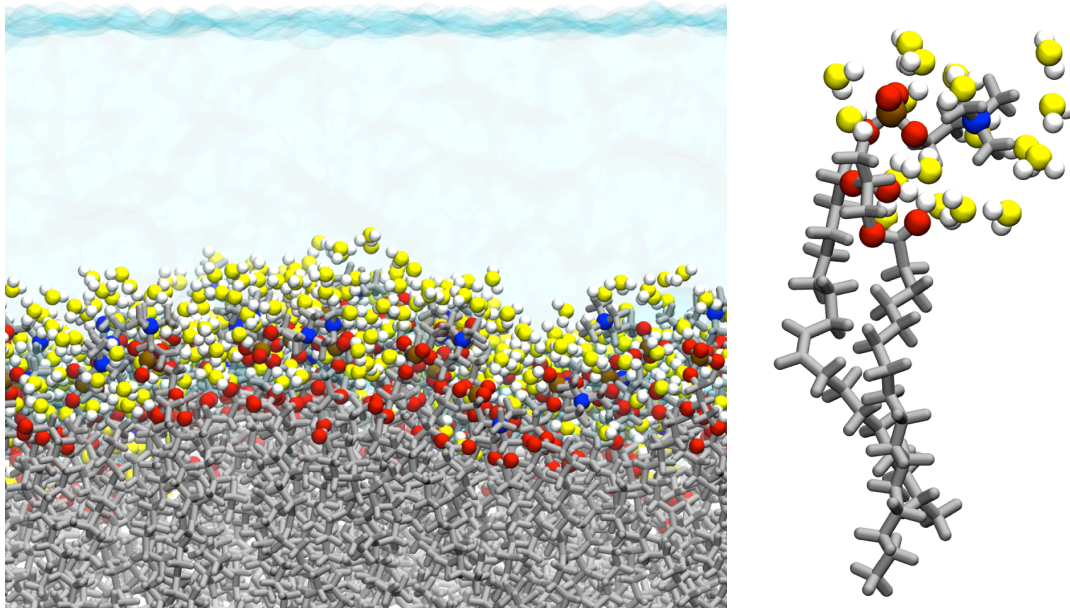


Fig. 1.3 Snapshot of interfacial water on the POPC lipid membrane by MD simulation. Oxygen, phosphorus, nitrogen, and carbon atoms of lipids are colored red, brown, blue, and gray, respectively. Water molecules correspond to the upper transparent coating. The interfacial water molecules on the lipid bilayer is colored yellow (oxygen) and white (hydrogen).

formed between non-ester phosphate oxygen, and the rest are formed between non-ester phosphate and carbonyl oxygen [54]. About half of those form multiple bridges. Mean residence time of such interfacial water molecules on the membrane surface is 7-71 ps depending on the binding sites and definitions of hydrated molecules [54, 56, 57].

The dynamics and structure of the interfacial water are largely influenced by the thermal motion of the polar head groups and lipid fluidity [45]. Translational and rotational motions of water molecules near membranes are slower than those in bulk [56, 58–60]. The degree of slowness of the dynamics depends on the location of water molecules near the lipid head group and lipid types. Neutral ethanolamine group of PE, negatively charged glycerol group of phosphatidylglycerol (PG), and negatively charged serine group of PS make the hydrated water molecules much slower than the neutral choline group of PC [56, 59]. To compare the effect of lipid membrane phase on properties of water-membrane interfaces, distearoyl-PC membrane (a gel phase) and dilinoleoyl-PC membrane (a liquid-crystalline phase) were studied at the same temperature 310 K [61]. The PC bilayer in the gel phase is

partially dehydrated at the carbonyl group, and rotational motion of surface water molecules is slower than that on the liquid-crystalline phase.

Containing of cholesterol also decreases lipid-lipid links and increases hydration in the polar region of the lipid membranes [55]. Increase of cholesterol concentration accelerates the surface water diffusivity [39]. Ions also affect the water environment on membrane surfaces. Cations induce dehydration of lipids [62] and perturb interfacial water organization [44]. Near the membrane surface (~ 0.1 nm), specific ions alter the activation energy of the surface water diffusivity, and the order of the activation energy follows the Hofmeister series [38].

1.3 Aquaporin

Aquaporins (AQPs), transmembrane proteins found in the cell membranes of all living entities, are natural transporter of water molecules. After the first discovery of AQP1 [63], 13 isoforms of human AQPs (AQP0-12) have been identified [64], each with a different tissue distribution and each playing specific physiological roles [65]. The basic function of AQPs in regulating the osmotic pressure of the cells has therapeutic potential in oedema, cancer, obesity, brain injury, glaucoma, and several other conditions [66]. In fact, congenital cataracts (AQP0), diabetes insipidus (AQP2), and the autoimmune demyelinating disease neuromyelitis optica are linked to the AQPs.

All AQPs are tetrameric proteins composed of four identical monomers, and some form large arrays with varying structural properties [67, 68] [see Fig. 1.4A]. The aquaporin family can be divided into three major groups based on the amino acid sequences: classical aquaporins, aquaglyceroporins, and unorthodox aquaporins [69]. The aquaporin group, which includes AQP0, AQP1, AQP2, AQP4, and AQP5, exclusively permits water molecules, rejecting charged molecules, ions and even protons [70–73]. The aquaglyceroporin group, which includes AQP3, AQP7, AQP9, and AQP10, can permeate other small solutes such as glycerol and urea other than water. The unorthodox aquaporin group includes AQP6, AQP8, AQP11, and AQP12. The AQP6 permeates anions [74] and AQP8 permeates urea [75]. The AQP11 and AQP12 are not expressed in plasma membrane but inside the cell, and have not been fully elucidated [76]. By understanding the mechanism of water permeation within AQPs, researchers can begin to design biomimetic nanopores for desalination processes [77–79].

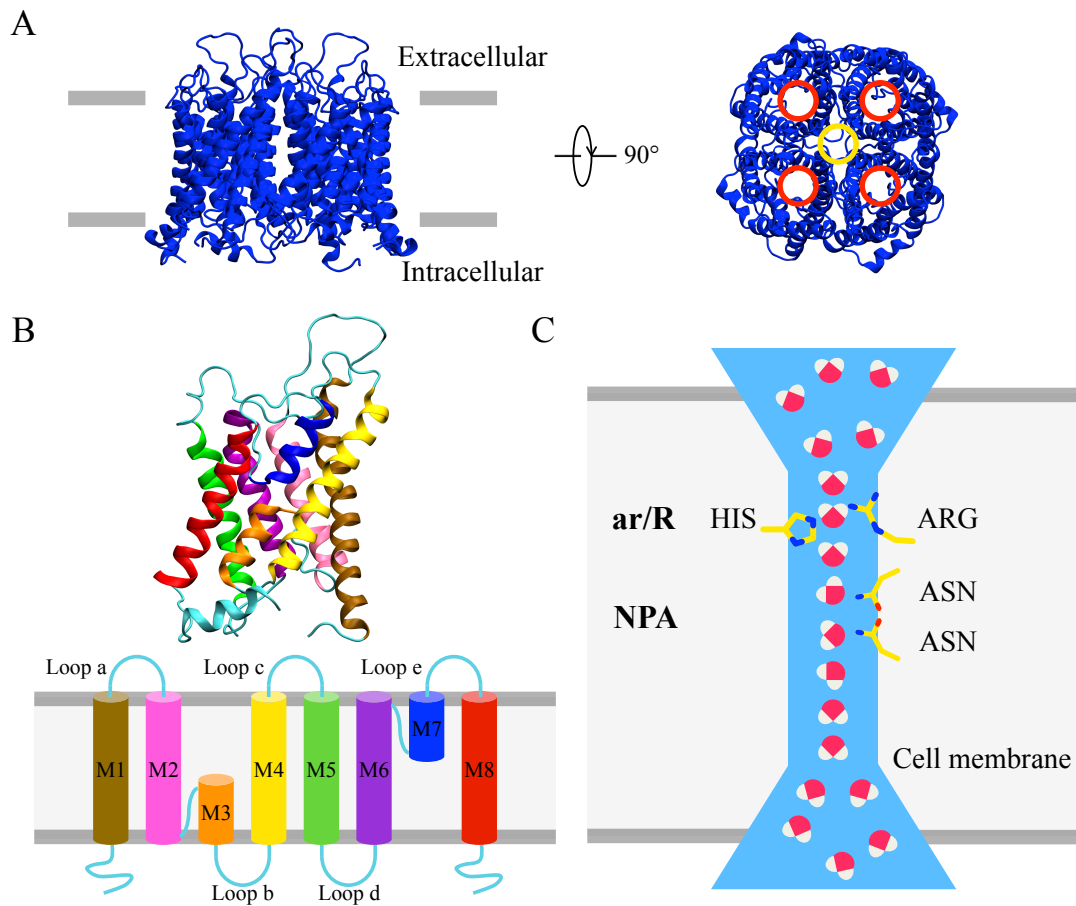


Fig. 1.4 Structure of aquaporins. (A) Structure of AQP1 tetramer, parallel to the membrane (left) and from the extracellular side (right). Water channels (red circle) in each tetramer and a central pore (yellow circle) in the center of the tetramer. (B) Overall structure of an AQP1 monomer. Eight transmembrane helices (M1-M8) and connecting loops are colored respectively. (C) Schematic representation of the aquaporin channel with ar/R region and NPA motif.

High-resolution overall structures have been established for some aquaporins: AQP0 [80,81], AQP1 [82,83], AQP2 [84], AQP4 [85], AQP5 [86], *E. coli* AqpZ [87], *E. coli* aquaglyceroporin GlpF [88,89], and malarial *Plasmodium falciparum* AQP [90]. These enable us to understand the mechanism of water permeation and other solute exclusion. Further insights into water configuration and the energetic of water permeation within AQPs have been provided by MD simulations [89,91–98].

AQPs consist of six transmembrane α -helices (M1, M2, M4-M7, and M8), two short helices (M3 and M7), and five connecting loops (loops a-e) [see Fig. 1.4B]. The tetrameric structure creates an additional hydrophobic narrow pore through its center, which permeates ions [99,100] and gas molecules [101]. The six transmem-

brane helices compose a hourglass shape narrow pore, where water molecules align in a single file and permeate with high permeability of approximately one water molecule per one nanosecond. Using a finite-element calculation the characteristic hourglass shape of AQPs was suggested to optimize the water permeation through the AQPs [102]. The cone-shaped vestibules of AQPs with suitable opening angle may make an increase of water permeability.

Channel steric conformation and solute binding sites within AQP pore facilitate the rapid and highly selective permeation of water molecules. There are two characteristic parts, the asparagine-proline-alanine (NPA) motif and the aromatic/arginine selectivity filter (ar/R region) [see Fig. 1.4C]. The NPA motif is located at the two short helices, cytoplasmic M3 and extracellular M7, in the center of the membrane. This motif is a part of hydrophilic surface and allows the water molecule to form hydrogen bonds with two asparagines, thereby reversing the orientation of the water molecule in opposite direction. Although asparagine is conserved, proline and alanine are variable, e.g. asparagine-proline-cysteine in AQP11 and asparagine-proline-threonine in AQP12 [64]. It has been suggested that the NPA motif play a key role for expression of AQPs in the plasma membrane [103].

The other domain is the ar/R region constituting the narrowest part of the pore, the diameter about 0.3 nm [83]. The ar/R region of aquaglyceroporins is wider and less polar [88, 89]. The ar/R region is composed of a conserved arginine and three amino acids, where histidine is conserved across most of water-specific AQPs. The different combination of amino acids in the ar/R region contributes to site diverse in size and hydrophobicity, and works as a filter blocking molecules that are too large to pass through the narrowest region [72]. Point mutations in the ar/R region in AQP1 allow passage of urea, glycerol, ammonia, and protons [104].

These two highly conserved parts has been treated as a controversial topic for proton exclusion filters. MD simulations suggest that the free energy barrier located at the NPA motif is dominant for the proton exclusion [89, 93, 95, 105–108]. But, this could not mention the fact that mutations in the ar/R-region increase the proton conductance [104, 109]. Recently, a high resolution X-ray structure of yeast aquaporin (0.88 Å) proposed that ar/R region breaks the continuous hydrogen bond network and is a feasible part to prevent proton permeation [110].

1.4 Thesis objective and outline

In this thesis, we investigate the dynamics of water molecules around lipid membranes. In chapter 2, the computational methodology of MD simulations are introduced. In chapter 3, temperature dependence of water dynamics near the membrane surface is revealed. In chapter 4 and 5, anomalous dynamics, such as anomalous diffusion and $1/f$ noise, of water molecules on the membrane surfaces are discussed. Moreover, we reveal the origin of these anomalous dynamics. In chapter 6, relationship between conformational fluctuation of AQP and water permeation is discussed.

Chapter 2

Computational methods: Molecular dynamics simulation

The MD simulation is one of the computational techniques, where the motion of particles is solved by Newton's equation of motion. The equation of motion for particle i is described as

$$m_i \ddot{\mathbf{r}}_i = \mathbf{F}_i. \quad (2.1)$$

This equation is numerically solved by integrating coordinates and velocities of particles. Such a simulation technique can be a “computational microscope” in variety of research fields, such as physics, biology, chemistry, and engineering, for observing various phenomena at molecular levels and temporal time scales that are difficult to access experimentally.

2.1 Numerical integration

The equations of motion in the MD simulation cannot be solved analytically because these are simultaneous differential equations of all degree of freedom. Thus, numerical integration of difference equation is performed at every time steps Δt . Although various numerical integration methods have been developed, Verlet algorithm [111] as well as velocity-Verlet algorithm [112] is often used for MD simulations.

2.1.1 Verlet algorithm

Taylor expansion of coordinates $\mathbf{r}_i(t + \Delta t)$ and $\mathbf{r}_i(t - \Delta t)$ is given by

$$\mathbf{r}_i(t + \Delta t) = \mathbf{r}_i(t) + \Delta t \dot{\mathbf{r}}_i(t) + \frac{\Delta t^2}{2!} \ddot{\mathbf{r}}_i(t) + \frac{\Delta t^3}{3!} \dddot{\mathbf{r}}_i(t) + O(\Delta t^4), \quad (2.2)$$

$$\mathbf{r}_i(t - \Delta t) = \mathbf{r}_i(t) - \Delta t \dot{\mathbf{r}}_i(t) + \frac{\Delta t^2}{2!} \ddot{\mathbf{r}}_i(t) - \frac{\Delta t^3}{3!} \dddot{\mathbf{r}}_i(t) + O(\Delta t^4). \quad (2.3)$$

The sum of Eq. (2.2) and Eq. (2.3) is

$$\mathbf{r}_i(t + \Delta t) + \mathbf{r}_i(t - \Delta t) = 2\mathbf{r}_i(t) + \Delta t^2 \ddot{\mathbf{r}}_i(t) + O(\Delta t^4). \quad (2.4)$$

Using Eq. (2.1) and Eq. (2.4), we have

$$\mathbf{r}_i(t + \Delta t) = 2\mathbf{r}_i(t) - \mathbf{r}_i(t - \Delta t) + \frac{\Delta t^2}{m_i} \mathbf{F}_i(t) + O(\Delta t^4), \quad (2.5)$$

and from Eq. (2.2) and Eq. (2.3) we obtain

$$\dot{\mathbf{r}}_i(t) = \frac{\mathbf{r}_i(t + \Delta t) - \mathbf{r}_i(t - \Delta t)}{2\Delta t} + O(\Delta t^2). \quad (2.6)$$

The Eq. (2.5) and Eq. (2.6) are called Verlet algorithm [111].

2.1.2 Velocity-Verlet algorithm

Taylor expansion of coordinate $\mathbf{r}_i(t + \Delta t)$, velocity $\mathbf{v}_i(t + \Delta t)$, and force $\mathbf{F}_i(t + \Delta t)$ is given by

$$\mathbf{r}_i(t + \Delta t) = \mathbf{r}_i(t) + \Delta t \dot{\mathbf{r}}_i(t) + \frac{\Delta t^2}{2!} \ddot{\mathbf{r}}_i(t) + O(\Delta t^3), \quad (2.7)$$

$$\mathbf{v}_i(t + \Delta t) = \mathbf{v}_i(t) + \Delta t \dot{\mathbf{v}}_i(t) + \frac{\Delta t^2}{2!} \ddot{\mathbf{v}}_i(t) + O(\Delta t^3), \quad (2.8)$$

$$\mathbf{F}_i(t + \Delta t) = \mathbf{F}_i(t) + \Delta t \dot{\mathbf{F}}_i(t) + \frac{\Delta t^2}{2!} \ddot{\mathbf{F}}_i(t) + O(\Delta t^3). \quad (2.9)$$

Inserting $\dot{\mathbf{r}}_i(t) = \mathbf{v}_i(t)$ and $\ddot{\mathbf{r}}_i(t) = \mathbf{F}_i(t)/m_i$ into Eq. (2.7), we have

$$\mathbf{r}_i(t + \Delta t) = \mathbf{r}_i(t) + \Delta t \mathbf{v}_i(t) + \frac{\Delta t^2}{2!} \frac{\mathbf{F}_i(t)}{m_i} + O(\Delta t^3), \quad (2.10)$$

and using $\dot{\mathbf{v}}_i(t) = \mathbf{F}_i(t)/m_i$ with Eq. (2.8) - $\frac{\Delta t}{2}$ × Eq. (2.9) results in

$$\mathbf{v}_i(t + \Delta t) = \mathbf{v}_i(t) + \frac{\Delta t}{2m_i} (\mathbf{F}_i(t) + \mathbf{F}_i(t + \Delta t)) + O(\Delta t^3). \quad (2.11)$$

The Eq. (2.10) and Eq. (2.11) are called velocity-Verlet algorithm [112].

2.2 Constrained molecular dynamics simulation

The general force fields for MD simulations are designed to be applied constraints on all or partial of molecules. The constrained MD simulation is the method to treat molecules as rigid body

$$m_i \ddot{\mathbf{r}}_i = \mathbf{F}_i + \mathbf{R}_i, \quad (2.12)$$

$$\mathbf{R}_i = - \sum_k \lambda_k \nabla_i g_k, \quad (2.13)$$

$$g_k = (\mathbf{r}_i - \mathbf{r}_j)^2 - d_{ij}^2 = 0, \quad (2.14)$$

where \mathbf{R}_i is the force on particle i due to the constraints, λ_k is time-dependent Lagrange multipliers determined from Eq. (2.14), and d_{ij} is the fixed bond distance between particles i and j . The temporal differentiation of Eq. (2.14)

$$\dot{g}_k = 2 (\dot{\mathbf{r}}_i - \dot{\mathbf{r}}_j) (\mathbf{r}_i - \mathbf{r}_j) = 0, \quad (2.15)$$

means that relative velocity of particles i and j is normal to relative coordinate.

2.2.1 SHAKE algorithm

In the case of the constrained MD simulations with Eq. (2.12), the Verlet algorithm of Eq. (2.4) can be written as

$$\mathbf{r}_i(t + \Delta t) = 2\mathbf{r}_i(t) - \mathbf{r}_i(t - \Delta t) + \frac{\Delta t^2}{m_i} \mathbf{F}_i(t) + \frac{\Delta t^2}{m_i} \mathbf{R}_i(t). \quad (2.16)$$

The Eq. (2.16) can be divided into two terms: moved coordinate term, $\mathbf{q}_i(t + \Delta t)$, without constraints and correction term with constraints

$$\mathbf{r}_i(t + \Delta t) = \mathbf{q}_i(t + \Delta t) + \frac{\Delta t^2}{m_i} \mathbf{R}_i(t). \quad (2.17)$$

Inserting Eq. (2.17) into Eq. (2.14), constraint condition at time $t + \Delta t$ is given by

$$g_k(t + \Delta t) = \left\{ (\mathbf{q}_i(t + \Delta t) - \mathbf{q}_j(t + \Delta t)) + \Delta t^2 \left(\frac{\mathbf{R}_i(t)}{m_i} - \frac{\mathbf{R}_j(t)}{m_j} \right) \right\}^2 - d_{ij}^2 = 0. \quad (2.18)$$

Using Eq. (2.13), Eq. (2.14), and Eq. (2.18), we have

$$\begin{aligned} & 2\Delta t^2 (\mathbf{q}_i(t + \Delta t) - \mathbf{q}_j(t + \Delta t)) \left\{ - \sum_k 2\lambda_k \frac{1}{\mu_{ij}} (\mathbf{r}_i(t) - \mathbf{r}_j(t)) \right\} \\ & + 4\Delta t^4 \sum_k \sum_{k'} \lambda_k \lambda_{k'} \frac{1}{\mu_{ij} \mu_{i'j'}} (\mathbf{r}_i(t) - \mathbf{r}_j(t)) (\mathbf{r}_{i'}(t) - \mathbf{r}_{j'}(t)) \\ & = d_{ij}^2 - (\mathbf{q}_i(t + \Delta t) - \mathbf{q}_j(t + \Delta t))^2, \end{aligned} \quad (2.19)$$

where μ_{ij} is the reduced mass of particles in the constraint bond and given by

$$\frac{1}{\mu_{ij}} = \frac{1}{m_i} + \frac{1}{m_j}. \quad (2.20)$$

To obtain the λ_k by solving Eq. (2.19) is called SHAKE algorithm [113].

2.2.2 RATTLE algorithm

As using velocity-Verlet algorithm, we have to consider the constraint coordination and velocity. Dividing the difference formula of velocity-Verlet into moved coordinate term $q_i(t + \Delta t)$ without constraints and correction term with constraints, we have following expression

$$\mathbf{r}_i(t + \Delta t) = \mathbf{r}_i(t) + \Delta t \mathbf{r}_i(t) + \frac{\Delta t^2}{2m_i} \mathbf{F}_i(t) + \frac{\Delta t^2}{2m_i} \mathbf{R}_{Ri}(t), \quad (2.21)$$

$$\mathbf{r}_i(t + \Delta t) = \mathbf{q}_i(t + \Delta t) + \frac{\Delta t^2}{2m_i} \mathbf{R}_{Ri}(t), \quad (2.22)$$

$$\dot{\mathbf{r}}_i(t + \Delta t) = \dot{\mathbf{r}}_i(t) + \frac{\Delta t}{2m_i} (\mathbf{F}_i(t) + \mathbf{F}_i(t + \Delta t)) + \frac{\Delta t}{2m_i} (\mathbf{R}_{Ri}(t) + \mathbf{R}_{Vi}(t + \Delta t)), \quad (2.23)$$

$$\dot{\mathbf{r}}_i(t + \Delta t) = \dot{\mathbf{q}}_i(t + \Delta t) + \frac{\Delta t}{2m_i} \mathbf{R}_{Vi}(t + \Delta t), \quad (2.24)$$

where \mathbf{R}_{Ri} and \mathbf{R}_{Vi} are constraint forces for coordinate and velocity, respectively. Firstly, we consider \mathbf{R}_{Rij} . The constraint force of ij pair can be written as

$$\mathbf{R}_{Rij} = -\lambda_{Rij} \frac{\mathbf{r}_{ij}}{r_{ij}}. \quad (2.25)$$

Here, putting the following equation

$$g_{ij} = \frac{\lambda_{Rij} \Delta t^2}{2r_{ij}}, \quad (2.26)$$

into Eq. (2.22), the coordinates of particles i and j can be written as

$$\mathbf{r}_i(t + \Delta t) = \mathbf{q}_i(t + \Delta t) - \frac{g_{ij}}{m_i} \mathbf{r}_{ij}(t), \quad (2.27)$$

$$\mathbf{r}_j(t + \Delta t) = \mathbf{q}_j(t + \Delta t) + \frac{g_{ij}}{m_j} \mathbf{r}_{ij}(t). \quad (2.28)$$

Inserting Eq. (2.27) and Eq. (2.28) into Eq. (2.14) gives

$$d_{ij}^2 = |\mathbf{r}_{ij}(t + \Delta t)|^2 = |\mathbf{q}_{ij}(t + \Delta t) - g_{ij} \mu_{ij} \mathbf{r}_{ij}(t)|^2. \quad (2.29)$$

As ignoring the g_{ij}^2 term, g_{ij} is given by

$$g_{ij} \approx \frac{|\mathbf{q}_{ij}(t + \Delta t)|^2 - d_{ij}^2}{2\mu_{ij}(\mathbf{q}_{ij}(t + \Delta t) \cdot \mathbf{r}_{ij}(t))}. \quad (2.30)$$

The coordinates $\mathbf{r}_i(t+\Delta t)$ and $\mathbf{r}_j(t+\Delta t)$ are obtained putting g_{ij} into Eq. (2.27) and Eq. (2.28). Because Eq. (2.30) is an approximation formula, until the constraint condition Eq. (2.14) is achieved for all pair ij , the insertion of Eq. (2.30) into Eq. (2.27) and Eq. (2.28) is continued by replacing $\mathbf{q}_i(t + \Delta t)$ and $\mathbf{q}_j(t + \Delta t)$ with the obtained $\mathbf{r}_i(t + \Delta t)$ and $\mathbf{r}_j(t + \Delta t)$. The $\mathbf{F}_i(t + \Delta t)$ is obtained from $\mathbf{r}_i(t + \Delta t)$.

Secondly, we consider the constraint force \mathbf{R}_{Vij} . Because \mathbf{R}_{Vij} between particles i and j is proportional to \mathbf{r}_{ij} , \mathbf{R}_{Vij} can be written as

$$\mathbf{R}_{Vij} = -\lambda_{Vij} \frac{\mathbf{r}_{ij}}{r_{ij}}. \quad (2.31)$$

Putting the following k_{ij}

$$k_{ij} = \frac{\lambda_{Vij} \Delta t}{2d_{ij}}, \quad (2.32)$$

into Eq. (2.24), the velocities of particles i and j can be written as

$$\dot{\mathbf{r}}_i(t + \Delta t) = \dot{\mathbf{q}}_i(t + \Delta t) + \frac{k_{ij}}{m_i} \mathbf{r}_{ij}(t + \Delta t), \quad (2.33)$$

$$\dot{\mathbf{r}}_j(t + \Delta t) = \dot{\mathbf{q}}_j(t + \Delta t) + \frac{k_{ij}}{m_j} \mathbf{r}_{ij}(t + \Delta t). \quad (2.34)$$

Inserting Eq. (2.33) and Eq. (2.34) into constraint condition Eq. (2.15), k_{ij} is given by

$$k_{ij} = \frac{\mathbf{r}_{ij}(t + \Delta t) \cdot \mathbf{q}_{ij}(t + \Delta t)}{\mu_{ij} d_{ij}^2}. \quad (2.35)$$

Until the constraint condition Eq. (2.15) is achieved for all pair ij within a adequate error, the insertion of Eq. (2.35) into Eq. (2.33) and Eq. (2.34) is continued by replacing $\mathbf{q}_i(t + \Delta t)$ and $\mathbf{q}_j(t + \Delta t)$ with the obtained $\mathbf{v}_i(t + \Delta t)$ and $\mathbf{v}_j(t + \Delta t)$. This is called RATTLE algorithm [114].

2.3 Control of pressure and temperature

If all particles in a system are along trajectories in accordance with the Newton's equation of motion, the total energy E of the system is preserved. When the number of particles N and the volume V are constant in an isolated molecular system, the MD simulation achieves the microcanonical ensemble (NVE ensemble). Because many experiments are performed in a condition of constant temperature T and pressure P (isobaric-isothermal ensemble, NPT ensemble), MD simulations are

required ingenuity in the equation of motion to be equal to that of experiments. The temperature of the monatomic molecule is calculated by principle of equipartition

$$\frac{3}{2}Nk_{\text{B}}T = \sum_{i=1}^N \frac{1}{2}m_i\mathbf{v}_i^2. \quad (2.36)$$

The system pressure is calculated with the virial theorem

$$\mathbf{P} = \frac{1}{3V} \left[\sum_{i=1}^N m_i\mathbf{v}_i^2 + \sum_{i=1}^N (\mathbf{r}_i\mathbf{F}_i) \right]. \quad (2.37)$$

2.3.1 Berendsen's algorithm

Some methods have been developed to achieve constant temperature and pressure in MD simulations. The Berendsen's algorithm [115] is often used for the calculation of complex and large-scale system because of its simple treatment. Berendsen's algorithm for temperature control is accomplished by scaling the velocities of the particles at each time step as follows

$$\lambda = \sqrt{1 + \frac{\Delta t}{\tau_T} \left(\frac{T_0}{T} - 1 \right)}, \quad (2.38)$$

$$\mathbf{v}'_i = \lambda\mathbf{v}_i, \quad (2.39)$$

where τ_T , T_0 , and T are coupling time with an external heat bath, given temperature of the heat bath, and system temperature, respectively. The strength of the coupling with the heat bath can be controlled with τ_T .

Berendsen's algorithm for pressure control is accomplished by rescaling the coordinates of the particles and the cell size at every time step as follows

$$\boldsymbol{\mu} = \left[\mathbf{1} - \frac{\Delta t}{\tau_P} (\mathbf{P}_0 - \mathbf{P}) \right]^{1/3}, \quad (2.40)$$

$$\mathbf{r}'_i = \boldsymbol{\mu}\mathbf{r}_i, \quad (2.41)$$

$$\mathbf{V}' = (\det\boldsymbol{\mu})\mathbf{V}, \quad (2.42)$$

where τ_P , \mathbf{P}_0 , and \mathbf{P} are coupling time with a barostat, given reference pressure, and pressure of the system, respectively. The strength of the coupling with the barostat can be controlled with τ_P .

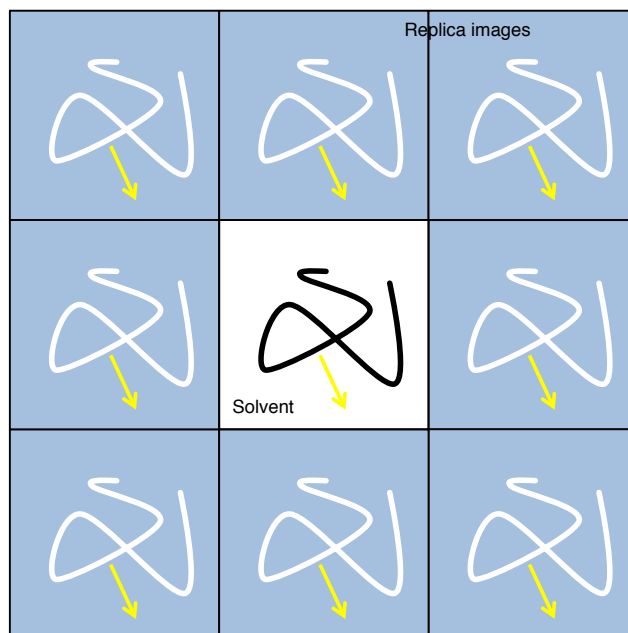


Fig. 2.1 Boundary condition.

2.4 Boundary condition

To approximate the results of MD simulations to reality, it is ideal to increase the number of particles in the system of MD simulations close to the real system, ideally handling the order of Avogadro number ($\simeq 10^{23}$). However, the limitation of the number of particles is 10^4 - 10^7 degrees with current high-performance computers. Thus, periodic boundary conditions are usually applied in MD simulations. The cubical simulation box Ω is replicated throughout space to form an infinite lattice Φ [see Fig. 2.1]. If a particle is in a system with cubic size L , the concept of the periodic boundary condition is written as

$$\Phi \approx \Omega(\mathbf{r}) + \Omega(\mathbf{r} + L\mathbf{n}), \quad (2.43)$$

where \mathbf{n} is an integer vector except for zero vector.

2.5 Force and potential

Some of the popular force fields such as AMBER, CHARMM, OPLS, and GROMOS use a simple functional form defined by bonded and non-bonded interactions. Total

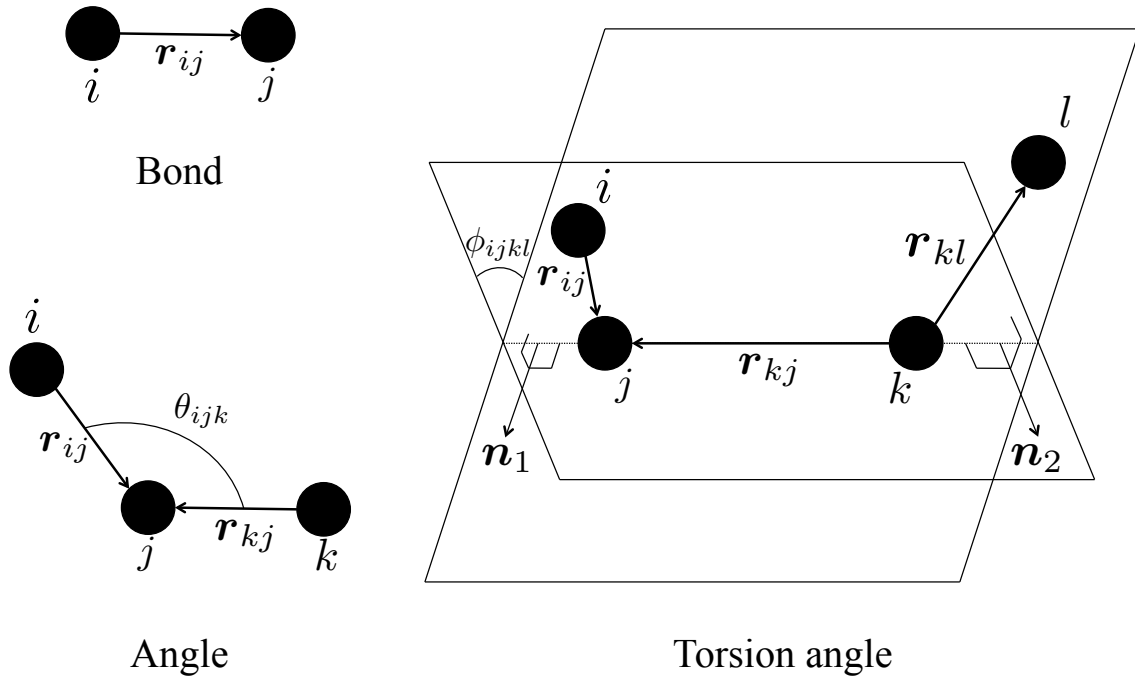


Fig. 2.2 Schematic diagram of bonded interactions.

potential energy U is represented by the following formula

$$\begin{aligned}
 U = & \sum_{\text{bonds}} K_b (r - r_0)^2 + \\
 & \sum_{\text{angles}} K_a (\theta - \theta_0)^2 + \\
 & \sum_{\text{torsions}} \frac{V_n}{2} (1 + \cos(n\phi - \gamma)) + \\
 & \sum_{\text{nonbond } ij} \varepsilon_{ij} \left[\left(\frac{R_{ij}}{r_{ij}} \right)^{12} - 2 \left(\frac{R_{ij}}{r_{ij}} \right)^6 \right] + \\
 & \sum_{\text{nonbond } ij} \frac{Q_i Q_j}{4\pi\epsilon r_{ij}}.
 \end{aligned} \tag{2.44}$$

In the following we will explain the individual potential.

2.5.1 Bonded interaction

Bond

For covalently bonded two atoms, the potential and force are calculated with an approximation of a spring [see Fig. 2.2]

$$U_{\text{bond } ij} = K_b (r_{ij} - r_0)^2, \tag{2.45}$$

$$\mathbf{F}_i = -\mathbf{F}_j = -2K_b(r_{ij} - r_0) \frac{\mathbf{r}_{ij}}{r_{ij}}, \quad (2.46)$$

where r_{ij} , r_0 , and K_b are distance between atoms, equilibrium distance, and spring constant of stretching vibration, respectively.

Angle

For three atoms, the potential and force are calculated with following equation [see Fig. 2.2]

$$U_{\text{angle } ijk} = K_a(\theta_{ijk} - \theta_0)^2, \quad (2.47)$$

$$\mathbf{F}_i = -2K_a(\theta_{ijk} - \theta_0) \frac{1}{r_{ij} \sin \theta_{ijk}} \left(\frac{\mathbf{r}_{kj}}{r_{kj}} - \cos \theta_{ijk} \frac{\mathbf{r}_{ij}}{r_{ij}} \right), \quad (2.48)$$

$$\mathbf{F}_i = -2K_a(\theta_{ijk} - \theta_0) \frac{1}{r_{kj} \sin \theta_{ijk}} \left(\frac{\mathbf{r}_{ij}}{r_{ij}} - \cos \theta_{ijk} \frac{\mathbf{r}_{kj}}{r_{kj}} \right), \quad (2.49)$$

$$\mathbf{F}_j = -\mathbf{F}_i - \mathbf{F}_k, \quad (2.50)$$

$$\cos \theta_{ijk} = \frac{\mathbf{r}_{ij} \cdot \mathbf{r}_{kj}}{r_{ij} r_{kj}}, \quad (2.51)$$

where θ_{ijk} , θ_0 , and K_a are angle between three bonded atoms ijk , equilibrium angle, and spring constant of deformation vibration, respectively.

Torsion

The potential and force of the torsion angle (dihedral angle) for i , j , k , and l atoms are calculated as following [see Fig. 2.2]. If we define the normal vector as $\mathbf{n}_1 = \mathbf{r}_{ij} \times \mathbf{r}_{kj}$, $\mathbf{n}_2 = \mathbf{r}_{kj} \times \mathbf{r}_{kl}$, the torsion angle ϕ ($-\pi < \phi \leq \pi$) is given by

$$\cos \phi = \frac{\mathbf{n}_1 \cdot \mathbf{n}_2}{n_1 n_2}, \quad (2.52)$$

$$\phi = -\text{sign}(\arccos(\cos \phi), \mathbf{r}_{kj} \cdot (\mathbf{n}_1 \times \mathbf{n}_2)). \quad (2.53)$$

The potential for the torsion angle is described as

$$U_{\text{torsion}} = \frac{V}{2}(1 + \cos(n\phi - \gamma)), \quad (2.54)$$

where V , n , and γ are spring constant of the dihedral angle, cycle, and equilibrated dihedral angle, respectively. The forces for i , j , k , and l are given by

$$\begin{aligned} \mathbf{F}_i &= f_a(\mathbf{f}_b \times \mathbf{r}_{kj}), \\ \mathbf{F}_j &= f_a(-\mathbf{f}_c \times \mathbf{r}_{kl} + \mathbf{f}_b \times \mathbf{r}_{ik}), \\ \mathbf{F}_k &= f_a(-\mathbf{f}_b \times \mathbf{r}_{ij} + \mathbf{f}_c \times \mathbf{r}_{jl}), \\ \mathbf{F}_l &= f_a(\mathbf{f}_c \times \mathbf{r}_{kj}), \end{aligned} \quad (2.55)$$

where f_a , f_b , and f_c are

$$\begin{aligned} f_a &= -\frac{nV}{2} \frac{\sin(n\phi - \gamma)}{\sin \phi}, \\ f_b &= \left(\frac{\mathbf{n}_2}{n_2} - \cos \phi \frac{\mathbf{n}_1}{n_1} \right) \frac{1}{n_1}, \\ f_c &= \left(\frac{\mathbf{n}_1}{n_1} - \cos \phi \frac{\mathbf{n}_2}{n_2} \right) \frac{1}{n_2}. \end{aligned} \quad (2.56)$$

2.5.2 Non-bonded interaction

Van der Waals force

The van der Waals force includes repulsion and attraction for non-bonded atom pairs at close and long ranges, respectively. The Lennard-Jones potential [116] is often used as an approximate model for the van der Waals force

$$U_{ij} = \varepsilon_{ij} \left[\left(\frac{R_{ij}}{r_{ij}} \right)^{12} - 2 \left(\frac{R_{ij}}{r_{ij}} \right)^6 \right]. \quad (2.57)$$

The exponent in the first term, which is the repulsive term, is not necessary to be 12 and can be changed from 9 to 15. The exponent 6 in the second term, which is the attractive term, is based on quantum chemical calculation. The force is written as

$$\mathbf{F}_i = -\mathbf{F}_j = -\frac{12\varepsilon_{ij}}{R_{ij}} \left[\left(\frac{R_{ij}}{r_{ij}} \right)^{13} - \left(\frac{R_{ij}}{r_{ij}} \right)^7 \right] \frac{\mathbf{r}_i - \mathbf{r}_j}{r_{ij}}, \quad (2.58)$$

where ε_i , ε_j , R_i , and R_j are decided from Fig. 2.3. The ε_{ij} and R_{ij} are defined as $\varepsilon_{ij} = \sqrt{\varepsilon_i \varepsilon_j}$ and $R_{ij} = R_i + R_j$.

Coulomb force

The electrostatic interaction between electrically charged particles is described by Coulomb's law:

$$U_{ij} = \frac{Q_i Q_j}{4\pi\epsilon r_{ij}}, \quad (2.59)$$

where Q is the charge of the particle. Because the decay of this potential is very slow, the cutoff method cannot be used in this case. Therefore, in MD simulations, the Ewald method [117] is usually used for the calculation of the coulombic interaction.

In the Ewald method, the interaction is separated into the real space and reciprocal space functions. The potential energy of the Coulombic interaction in the Ewald

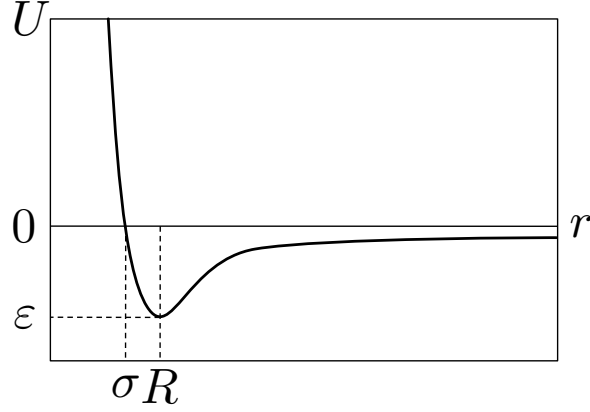


Fig. 2.3 Van der Waals potential.

method is given by

$$U_{\text{Ewald}} = U_1 + U_2 + U_3, \quad (2.60)$$

$$U_1 = \frac{1}{2} \sum_n \sum_i \sum_{j(j \neq i)} \frac{Q_i Q_j}{4\pi\epsilon_0} \frac{\text{erfc}(\alpha |\mathbf{r}_i - \mathbf{r}_j + L\mathbf{n}|)}{|\mathbf{r}_i - \mathbf{r}_j + L\mathbf{n}|}, \quad (2.61)$$

$$U_2 = \frac{2\pi}{L^3} \sum_{\mathbf{G}} \frac{\exp(-|\mathbf{G}|^2/4\alpha^2)}{|\mathbf{G}|^2} \sum_i \sum_j \frac{Q_i Q_j}{4\pi\epsilon_0} \cos[\mathbf{G} \cdot (\mathbf{r}_i - \mathbf{r}_j)], \quad (2.62)$$

$$U_3 = - \sum_i \frac{Q_i^2}{4\pi\epsilon_0} \frac{\alpha}{\sqrt{\pi}}, \quad (2.63)$$

where $\mathbf{G} = \frac{2\pi}{L} \mathbf{h}$ is the reciprocal lattice vector, and \mathbf{h} is an integer vector.

Chapter 3

Temperature dependence of water dynamics near membrane surfaces

3.1 Introduction

Cryopreservation is a process to preserve tissues at low temperature. In the cooling process, water crystallization causes mechanical damage to cell membranes. Thus, it is important to investigate the behavior of water molecules near cell membranes at low temperature.

Temperature dependence of water molecules near membrane surfaces has been investigated by experimental and computational approaches [32, 35, 37, 118, 119]. Polarized infrared spectroscopy technique revealed that hydration water molecules near palmitoyl-oleoyl-phosphatidylcholine (POPC) membrane can be divided into two groups: well-structured low density “network” water and less-structured dense “multimer” water [32]. According to an increase in temperature, the network water decreases whereas the multimer water increases. Using ODNP technique, the temperature dependence of the diffusion coefficient of water molecules within 1 nm of the spin-labeled site on the dihexadecanoyl-phosphatidylcholine (DPPC) membrane surface was found to follow the Arrhenius law between 295 K and 330 K [37]. MD simulation study [119] of single tail cationic surfactant membrane, behenyl trimethyl ammonium chloride, between 283 K and 350 K also confirmed the Arrhenius nature of water molecules near the membrane surface below the phase transition temperature of the membrane. The interfacial water molecules were defined as whose oxygen z coordinates remain continuously within ± 0.3 nm from the lipid head group peak positions for 40 ps. The entropy and potential energy of the interfacial water have a strong correlation with the phase transition of the membrane.

Such a correlation is also observed for hydration water reorientation dynamics on the dimyristoyl-phosphatidylcholine (DMPC) membrane with THz-TDS [35]. Using broadband dielectric spectroscopy and modulated differential scanning calorimetry techniques below 250 K [118], it was investigated that the Arrhenius temperature dependence of dynamics of the DMPC lipid head group at high hydrated state, which changes to a super-Arrhenius nature at low hydration level, has a correlation with relaxation of interfacial water molecules near the lipid head group.

Translational and rotational motions of water molecules near membranes are slower than those in bulk [58, 59]. However, little is known regarding how and why water molecules near membranes become slow. It is considered that power-law distribution of residence times, which is observed in water molecules on proteins [120–122] and DNA [123], is related to the water retardation on lipid membrane surfaces.

Power-law trapping-time distributions are widespread phenomena ranging from Hamiltonian systems [124] and material science [125–127] to biological phenomena [13, 128–130]. Two mechanisms generating a power-law trapping-time distribution are well-known. One is a random energy landscape [131]. Following the Arrhenius law, the average trapping time $\langle \tau_E \rangle$ in a potential valley is proportional to $\tau_0 \exp(E/k_B T)$, where τ_0 , E , T , and k_B denote the characteristic escape time, energy barrier height, temperature, and Boltzmann's constant, respectively. A power-law trapping time distribution can be observed when the barrier heights follow the exponential distribution $P(E) = E_0^{-1} \exp(-E/E_0)$, where E_0 is the mean barrier height. For simplicity, we assume $\tau_E = \langle \tau_E \rangle = \tau_0 \exp(E/k_B T)$. Using the relation $P(\tau_E)d\tau_E = P(E)dE$, we can calculate the distribution $P(\tau)$ of the trapping times for which particles are confined within exponentially distributed random potential valleys [132]:

$$\begin{aligned} P(\tau) &= \frac{1}{E_0} \exp\left(-\frac{E}{E_0}\right) \frac{k_B T}{\tau_0} \exp\left(-\frac{E}{k_B T}\right) \\ &= \frac{k_B T}{E_0} \left(\frac{\tau}{\tau_0}\right)^{-\mu-1} \frac{1}{\tau_0}, \end{aligned} \quad (3.1)$$

for $\tau \geq \tau_0$, where $\mu = k_B T/E_0$ and E_0 is the mean barrier height. Here, it is assumed that there is no correlation in the barrier heights. The other one is a comb-like structure [133]. If particles diffuse in a comb-like structure, they cannot move to the direction perpendicular to the comb while in the comb. The distribution

of escape times from the comb follows a power law with exponent $3/2$ ($\mu = 1/2$), which is that of recurrence times to the origin in one-dimensional random walk. The former is attributed to an energy trap, while the latter is attributed to an entropy trap [134]. There exists another origin for a power law in the trapping-time distribution. For example, the distribution of trapping times for which particles governed by the fractional Langevin equation are confined within a potential follows a power-law distribution (escape from a potential driven by a fractional noise) [135].

Here, we perform MD simulations on system of water molecules plus a palmitoyl-oleoyl-phosphatidylethanolamine (POPE) membrane at temperature 250-350 K to investigate diffusivities of water molecules near the membrane surface. We report that long time trappings of water molecules induced by a power-law trapping-time distribution enhance the viscosity of water molecules around membrane surfaces. The temperature dependence of the water molecular motions on the membrane surface is different from that in bulk. Decreasing temperature enhances the water retardation on the membrane surface. Moreover, we show that water molecules on the membrane surface exhibit a subdiffusion, i.e. sublinear growth of the mean square displacement.

3.2 Methods

To elucidate the temperature dependence of water dynamics around the lipid membrane surface, MD simulations of a POPE bilayer were performed at temperature ranging from 250 K to 350 K. The lipid bilayer system of pure POPE lipids was consisted of 128 lipids (64 for each leaflet) and 10,004 TIP3P water molecules [see Fig. 3.1]. We minimized the energy of all molecules by steepest descent method followed by the conjugate gradient method. A 200 ns simulation of the membrane system provided with constant number of atoms at pressure of 0.1 MPa and temperature of 310 K was performed, and the final structure of the simulation was defined to be a standard structure. We performed additional 60-90 ns simulations at several temperatures (250, 270, 280, 290, 330, and 350 K) using the standard structure. The stability and equilibration of each system were monitored by average area per lipid. All MD simulations were carried out under constant atom number, pressure, and temperature, using the Berendsen's algorithm [115] with a coupling time of 0.2 ps. The time step was set at 1 fs. The lengths of bonds involving the hydrogen atoms were constrained to equilibrium lengths using the SHAKE method.

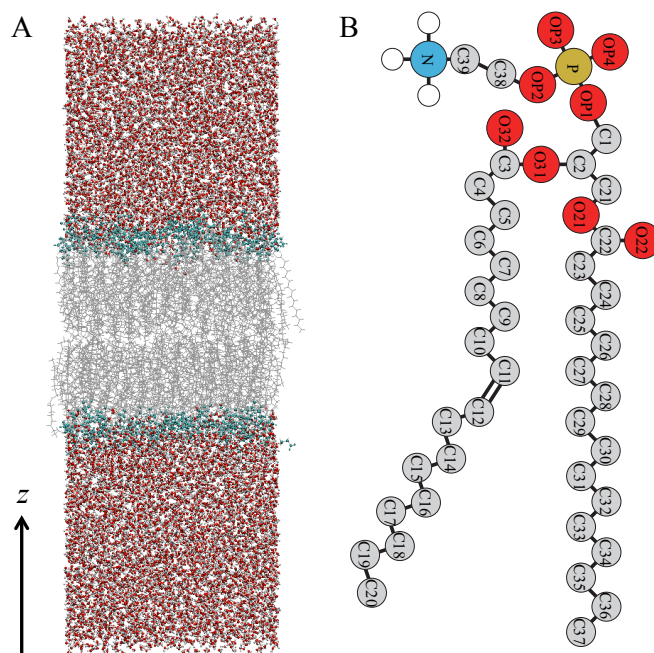


Fig. 3.1 Schematic view of the simulation system. (a) Snapshot of the simulation system. Lipid bilayer and water molecules show silver and red, respectively. The surface of the lipid bilayer is colored with cyan. (b) Structural formula of the POPE lipid molecule. (Red, brown, light blue, and gray circles indicate oxygen, phosphorus, nitrogen, and carbon atoms, respectively.)

The GAFF force field was used for the POPE lipid. This parameter of POPE has been used in previous studies about the membrane or a membrane protein [5,13,96], and the transition temperature was estimated about 280 K [5]. We note that the area per lipid at 310 K is smaller than experimental data [136] and almost the same as other MD simulations [137–139], indicating that POPE bilayer is a little stiff in our simulations. The particle mesh Ewald method was used with a specified direct space cutoff distance of 1.0 nm. A three-dimensional periodic boundary condition was imposed on all systems. The properties of each system were analyzed from the trajectories of the final 20 ns of each system. MD simulations were performed using AMBER10 software [140].

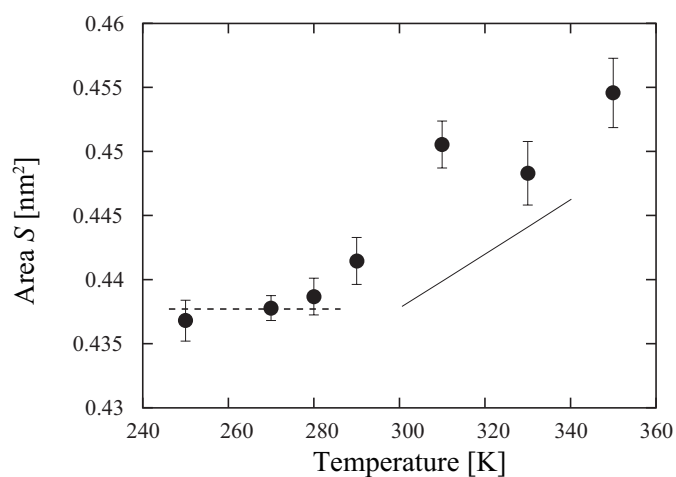


Fig. 3.2 Area per lipid at different temperature. Circles with error bars are the result of MD simulations. Areas from 250 to 280 K are almost constant, and areas above 280 K notably increase. This suggests that transition temperature is around 280 K. The dashed line is the average area from 250 to 280 K, and the solid line is the increasing rate of areas from 280 to 350 K calculated by the least-squares method.

3.3 Results and Discussion

3.3.1 Residence of water molecules on the POPE membrane surface

To investigate dynamics of water molecules near the membrane surface, we define the layer of water molecules in an explicit manner. Although a location of water molecules near the surfaces of membranes can be defined by their perpendicular distance from the surfaces of the head group regions of membranes, this distance cannot be determined exactly because the membrane surface is fluctuating and undulate. Therefore, we classify the layer of water molecules according to their hydrogen bond connectivity if water molecules remain over 5 ps in the layer. If the residence time is less than 5 ps, we removed the water molecules from the ensemble in layers. More precisely, water molecules in the first layer form hydrogen bonds with surface lipid molecules, those in the second layer hydrogen-bond to the first layer water molecules, those in the third layer hydrogen-bond to the second layer water molecules, etc. Hydrogen bonds form when interatomic distances between N (lipid) - O (water), O (lipid) - O (water), and O (water) - O (water) are within 0.34, 0.33, and 0.32 nm, respectively. We note that water molecules in the sixth layer reside about 1.2 nm above the surface of membranes. Bulk water molecules are defined as molecules more than 4.0 nm distant from the membrane surfaces.

Figure 3.3A shows a trajectory of a water molecule projected onto the lateral plane (xy plane). Water molecules in the first layer can diffuse slowly on the xy plane while they are trapped on the membrane surface. As shown in Fig. 3.3B, the probability density function (PDF) of residence time $P(t)$, which is defined by the times during which water molecules remain in the first layer, at temperature ranging 250-350 K follows power-law, $P(t) \propto t^{-2.3}$ to $t^{-2.7}$. Moreover, as shown in Fig. 3.3C, the power-law exponent increases linearly as a function of temperature. The observed linear relationship between power-law exponent and temperature is consistent with Eq. 3.1. Therefore, it is physically reasonable to consider that the power-law residence time of water molecules on membrane surfaces is attributed to a random energy landscape constructed by interactions between the water molecules and lipid molecules near the membrane. This random energy landscape could be provided by complex surfaces composed with the hydrophilic head groups of lipid molecules, which typically comprise phosphate, choline, and glycerol. The linear

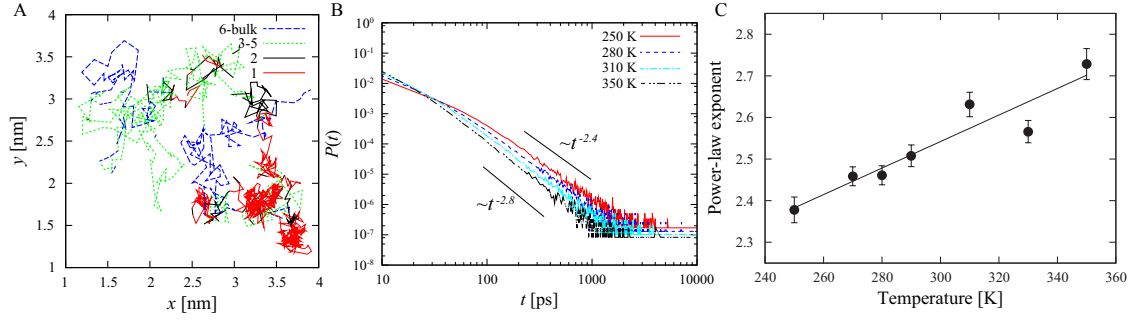


Fig. 3.3 Residence of water molecules on the POPE membrane surface. (A) Lateral trajectory of a water molecule tracked for 1 ns at 310 K. Red, black, green, and blue lines with different line types represent the trajectories in the first layer, second layer, third to fifth layer, and sixth layer to bulk, respectively. Water molecules in the first layer can diffuse locally, whereas water molecules far from the lipid bilayer surface diffuse widely. (B) PDFs of residence times of water molecules in the first layer at temperature 250, 280, 310, and 350 K. $P(t)$ follow power laws $t^{-\alpha}$ for all temperature. (C) Power-law exponents of $P(t)$. The power-law exponents are calculated by the least-square method within the region $3 \leq \ln(t) \leq 6.5$ for all temperature. Symbols are the results of simulations; the solid line represents a linear fitting. Power-law exponents are linearly dependent on temperature.

temperature dependence of power-law exponents holds around the transition temperature of the POPE membrane (about 280 K for this force field) [see Fig. 3.2]. This result suggests that phase transition of the membrane does not influence the power-law behavior.

3.3.2 Diffusivities of water molecules near the POPE membrane surface

In normal diffusion, the mean square displacement (MSD) grows linearly with time:

$$\langle |\mathbf{r}(t) - \mathbf{r}(0)|^2 \rangle \sim 2dDt \quad (t \rightarrow \infty), \quad (3.2)$$

where $\mathbf{r}(t)$ is a particle position at time t , D is the diffusion coefficient, d is the dimension, and $\langle \dots \rangle$ denote an ensemble average. In this form, the diffusion coefficient can be expressed as

$$D = \lim_{t \rightarrow \infty} \frac{\langle |\mathbf{r}(t) - \mathbf{r}(0)|^2 \rangle}{2dt}. \quad (3.3)$$

However, the diffusion coefficient cannot properly characterize the diffusivity of water molecules near the membrane surfaces because water molecules do not always remain in such a local space for a long time. To characterize a translational motion of water molecules near the membrane surfaces, we introduce the mean exit time (MET) [141]. The MET for lateral direction (METL) and z direction (METZ)

are defined by the mean of the exit times: $\text{METL} = \langle t_L \rangle$, $\text{METZ} = \langle t_Z \rangle$, where t_L and t_Z are the exist times for lateral and z directions, respectively. These are defined by $t_L = \min\{t|\{x(t+t_0) - x(t_0)\}^2 + \{y(t+t_0) - y(t_0)\}^2 > 2L^2\}$, $t_Z = \min\{t|\{z(t+t_0) - z(t_0)\}^2 > L^2\}$, where t_0 defines the entry time of a water molecule into each layer and L is a distance to the exit. We note that the layer of a water molecule at t_L may not be the same as that at t_0 . In other words, we include water molecules in the ensemble of the METs even when they escape from the layer at t_0 . The diffusion coefficient is approximately equal to $L^2/2\text{MET}$. In bulk, the METL and METZ are identical. Figure 3.4 shows the METs when L^2 is set at 0.5 nm^2 , almost twice the interatomic hydrogen bond distance between two water molecules. We confirmed that the result is qualitatively the same as $L^2 = 0.1 \text{ nm}^2$, almost the interatomic hydrogen bond distance between two water molecules [see Fig. 3.6]. Figures 3.4A and 3.4B show the METs for each temperature. For the lateral direction, we use trajectories of water molecules that are subtracted the position of the center of mass of the membrane because the membrane itself can diffuse laterally due to a finite size effect.. The METL and METZ near the surface of the membrane become large due to interactions between water molecules and head groups of lipid molecules. Temperature dependence of the METL and METZ differs in each layer. The differences of the METL and METZ between the first layer and bulk become large as temperature decreases. At low temperature, water molecules near the surface of the membrane become more viscous than bulk molecules, but this effect decreases at higher temperature. Figures 3.4C and 3.4D show the PDFs of the METL and METZ for different layers at 310 K. The shapes of the distributions depend on the layers. Diffusivities in the z direction and the lateral direction on the membrane surface are about 2.7 (350 K) - 3.7 (250 K) and 2.5 (350 K) - 3.5 (250 K) times slower than the bulk diffusivity, respectively [see Fig. 3.5A]. As the METZ ratio between the first layer and bulk becomes large, the METL ratio becomes large, which means that decrease in lateral diffusivity is positively associated with that in the z direction. Therefore, enhanced power-trappings make the translational motions of water molecules near the membrane surface much slower than those in bulk especially at low temperature. As a result, temperature dependence near the membrane surface is more sensitive than that in bulk.

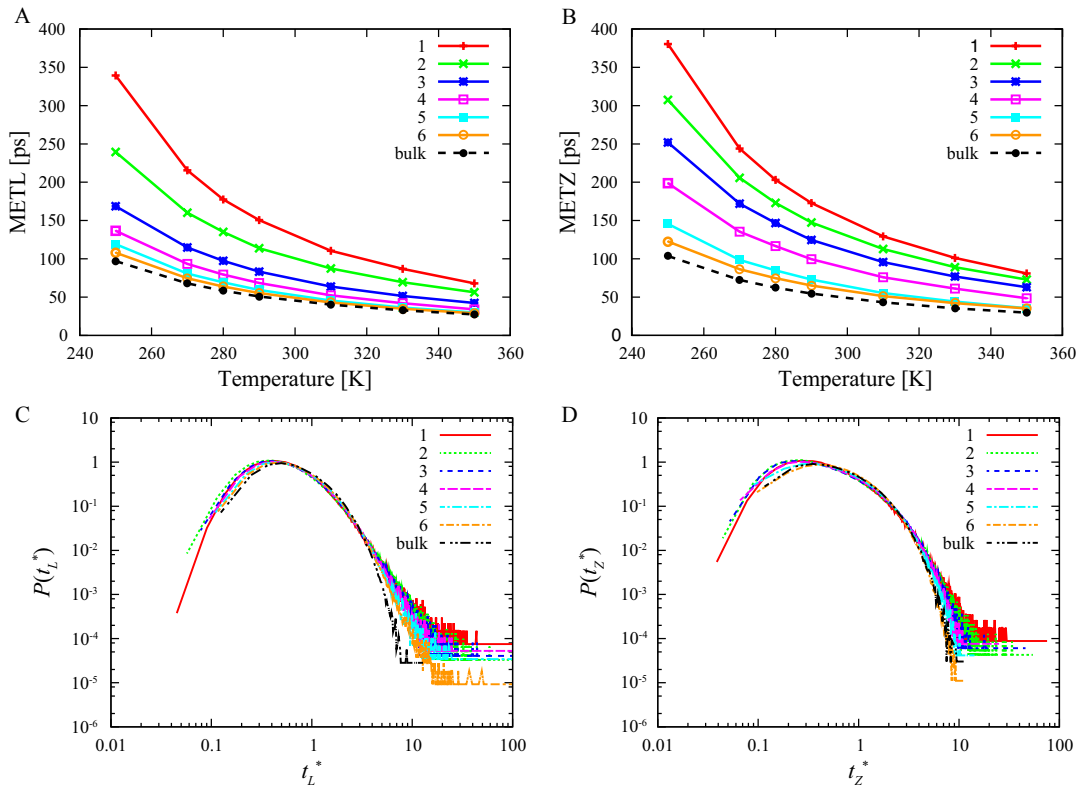


Fig. 3.4 Translational motion of water molecules near the POPE membrane surface (mean exit times in the case $L^2 = 0.5 \text{ nm}^2$). (A)(B) METL and METZ of water molecules at different temperature and layers (symbols with lines). (C)(D) Probability density function (PDF) of exit times for lateral and z direction at 310 K. PDFs $P(t^*)$ are normalized by their mean, $t^* = t / \langle t_i \rangle$, where $\langle t_i \rangle$ means the average of MET in i th layer. The METLs for $i = 1$ to 6 and bulk are 111, 87, 63, 52, 46, 43, and 40 ps, respectively. The METZs for $i = 1$ to 6 and bulk are 129, 113, 96, 76, 55, 51, and 43 ps, respectively.

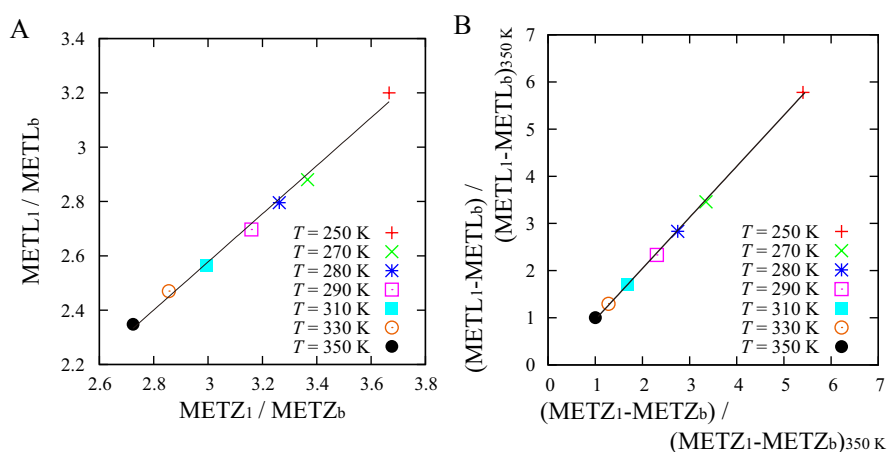


Fig. 3.5 Differences of translational motion of water molecules between the first layer and bulk. (A) The METL ratio between the first layer and bulk ($METL_1 / METL_b$) vs. the METZ ratio ($METZ_1 / METZ_b$). (B) The METL differences between the first layer and bulk ($METL_1 - METL_b$) vs. the METZ ratio ($METZ_1 - METZ_b$). Solid line is a linear fitting of all data.

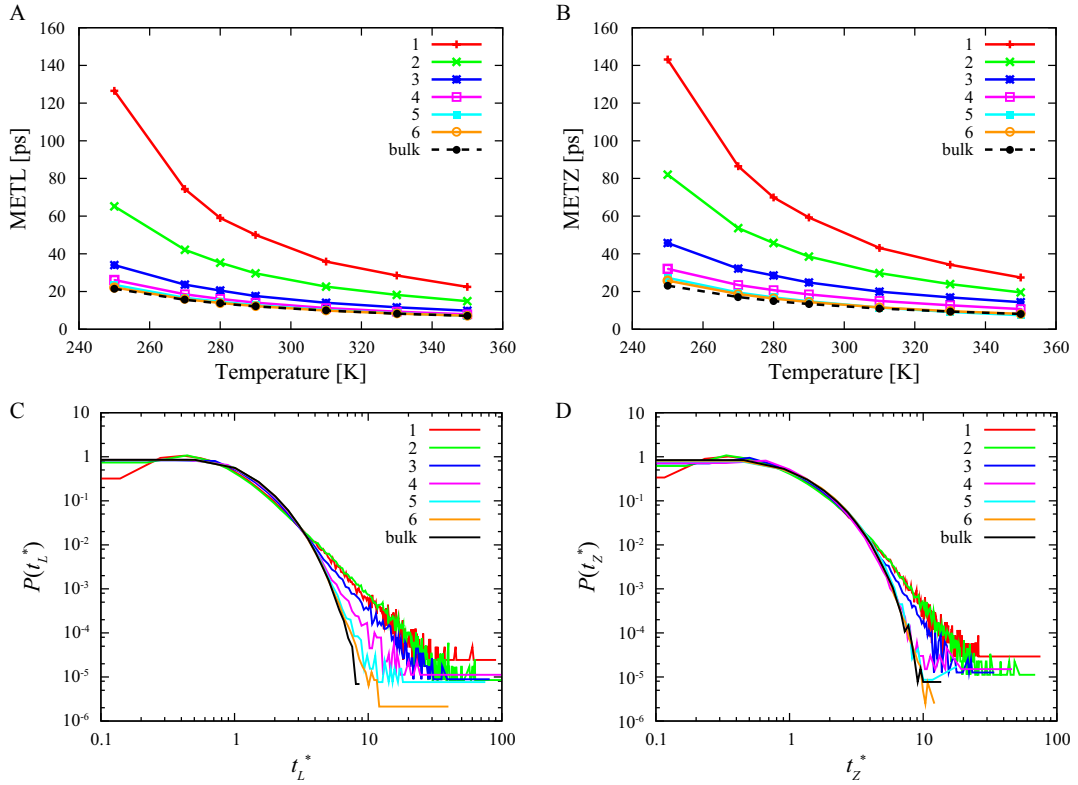


Fig. 3.6 Mean exit times in the case $L^2 = 0.1 \text{ nm}^2$. (A)(B) METL and METZ of water molecules at different temperature and layers (symbols with lines). (C)(D) Probability density function (PDF) of exit times for lateral and z direction at 310 K. PDFs $P(t^*)$ are normalized by their mean, $t^* = t / \langle t_i \rangle$, where $\langle t_i \rangle$ means the average of MET in i th layer. The METLs for $i = 1$ to 6 and bulk are 36, 23, 14, 11, 10, and 10 ps, respectively. The METZs for $i = 1$ to 6 and bulk are 43, 30, 20, 15, 11, 11, and 11 ps, respectively.

3.3.3 Rotational motion of water molecules near the POPE membrane surface

To investigate rotational motions of water molecules near the membrane surfaces, we consider an orientational correlation function of water molecules, defined by

$$C_i(t) = \langle \vec{\mu}_i(t + t_0) \cdot \vec{\mu}_i(t_0) \rangle, \quad (3.4)$$

where t_0 is the entry time of a water molecule into the i -th layer, and $\vec{\mu}_i(t + t_0)$ is a dipole vector of a water molecule at time $t + t_0$. As shown in Fig. 3.7A, $C_i(t)$ is fitted by a superposition of exponential functions: $C_i(t) = (1 - A_i) \exp(-t/\tau'_i) + A_i \exp(-t/\tau_i)$ with $\tau_i > \tau'_i$ [142], where $i = 1, \dots, 6$ and b . Relaxation times τ'_i , τ_i and weight A_i of the first layer and bulk are summarized in Table 3.1. The weight A_i is larger than $1 - A_i$ for all temperature, and increase as temperature decreases. Figure 3.7B shows the relaxation time τ_i . It follows that rotational motions of water molecules near the surface of the membrane are slower than those in bulk for all temperature. Although the relaxation times τ_i for over fourth layer are almost the same as those in bulk, the relaxation times τ_i of the first and second layer are about 2-5 times larger than those in bulk. Differences of the relaxation time between the first layer and bulk increases according to a decrease in temperature [see Fig. 3.8B]. As opposed to the temperature dependence of the normalized METL and METZ, the ratio between the first layer and bulk τ_1/τ_b decreased according to a decrease in temperature [see Fig. 3.8A]. The results indicate that long time trappings on the membrane surface do not affect the relaxation time very much and that temperature dependence of the relaxation time due to interaction between water and lipid molecules is less sensitive than that due to interaction between water and water molecules.

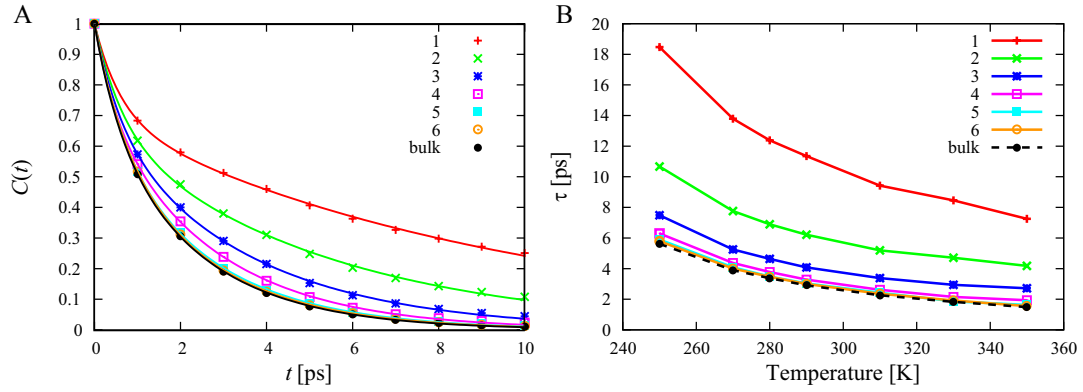


Fig. 3.7 Rotational motion of water molecules on the POPE membrane surface. (A) Orientational correlation functions of water molecules with fitting curves $C_i(t) = (1 - A_i) \exp(-t/\tau'_i) + A_i \exp(-t/\tau_i)$. Orientational correlation functions in different layers are distinguished by different symbols and colors. Solid curves are the fitting curves. (B) Relaxation time of the orientational correlation function of water molecules at different temperature and layers (symbols with lines). Relaxation times for different layers are distinguished by symbols.

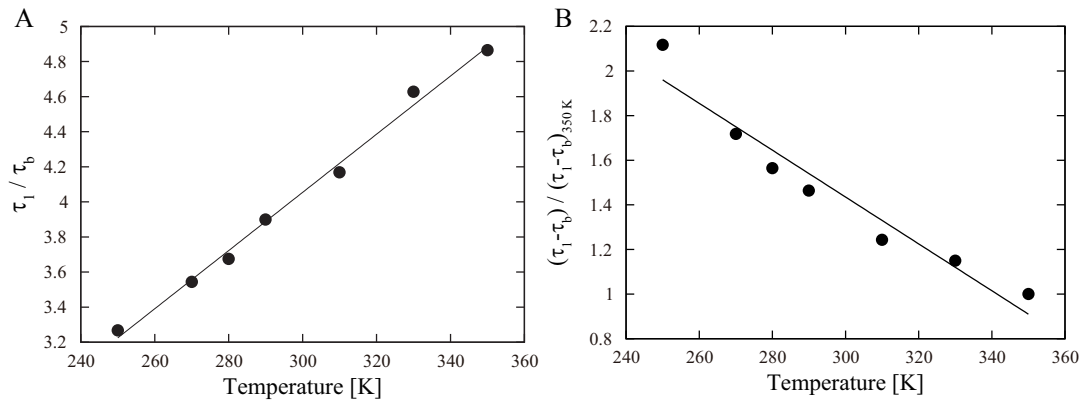


Fig. 3.8 Differences of rotational motion of water molecules between the first layer and bulk. (A) Ratio between the first layer and bulk τ_1/τ_b vs. temperature. (B) Difference between the first layer and bulk $\tau_1 - \tau_b$ vs. temperature. Solid line is a linear fitting of all data.

Table 3.1 The factor of the orientational correlation function fitting curves of water molecules: (τ'_i, τ_i, A_i)

	τ'_1 [ps]	τ_1 [ps]	A_1	τ'_b [ps]	τ_b [ps]	A_b
250 K	0.52	18.5	0.82	0.62	5.61	0.82
270 K	0.58	13.8	0.78	0.58	3.90	0.79
280 K	0.59	12.4	0.76	0.65	3.37	0.76
290 K	0.60	11.4	0.74	0.61	2.91	0.75
310 K	0.60	9.42	0.70	0.57	2.26	0.72
330 K	0.61	8.46	0.65	0.56	1.83	0.67
350 K	0.60	7.26	0.61	0.51	1.49	0.64

3.3.4 Anomalous diffusion of water molecules on the POPE membrane surface

To investigate the dynamics of water molecules, we consider the ensemble-averaged translational mean-squared displacement (tMSD) given by

$$\langle l^2(t) \rangle = \frac{1}{2} \langle \{x(t+t_0) - x(t_0)\}^2 + \{y(t+t_0) - y(t_0)\}^2 \rangle, \quad (3.5)$$

where t_0 is the time when water molecules enter the first layer. In considering rotational diffusion, we define $\delta\theta(t) \equiv \cos^{-1}(\vec{\mu}(t) \cdot \vec{\mu}(t+\delta t))$ and direction $\vec{p}(t) \equiv \vec{\mu}(t) \times \vec{\mu}(t+\delta t)$, where $\vec{\mu}(t)$ is the dipole vector of a water molecule at time t . The vector $\vec{\varphi}(t) \equiv \int_{t_0}^{t_0+t} \delta\theta(t') \vec{p}(t') dt'$ gives us the trajectory representing the rotational motion. Then, the ensemble-averaged rotational mean-squared displacement (rMSD) [143] is given by

$$\langle \varphi^2(t) \rangle = \langle |\vec{\varphi}(t) - \vec{\varphi}(0)|^2 \rangle. \quad (3.6)$$

We note that the ensemble of the MSD at time t does not include water molecules that have ever exited from the first layer. Therefore, the ensemble is not exactly the same as that of the METs. We use trajectories of water molecules that are subtracted the position of the center of mass of the membrane. As shown in Fig. 3.3.4, translational and rotational diffusion of water molecules near the surface of the membrane is not normal but subdiffusion, i.e. the sublinear growth of the MSD. In the next Chapter 4, we investigate the origin of the subdiffusion.

In summary, we have found that the PDF of residence times of water molecules on the POPE membrane surface follows a power-law. Because there are correlation between lateral and vertical motions of water molecules near the membrane surface, long time tappings induced by a power-law residence time distribution enhance the viscosity of water molecules near the membrane surfaces. Translational and rotational motions near the surface of the membrane surface become much slower than those in bulk as temperature decreases. We have also found that translational and rotational motions of water molecules on the membrane surface exhibit subdiffusion.

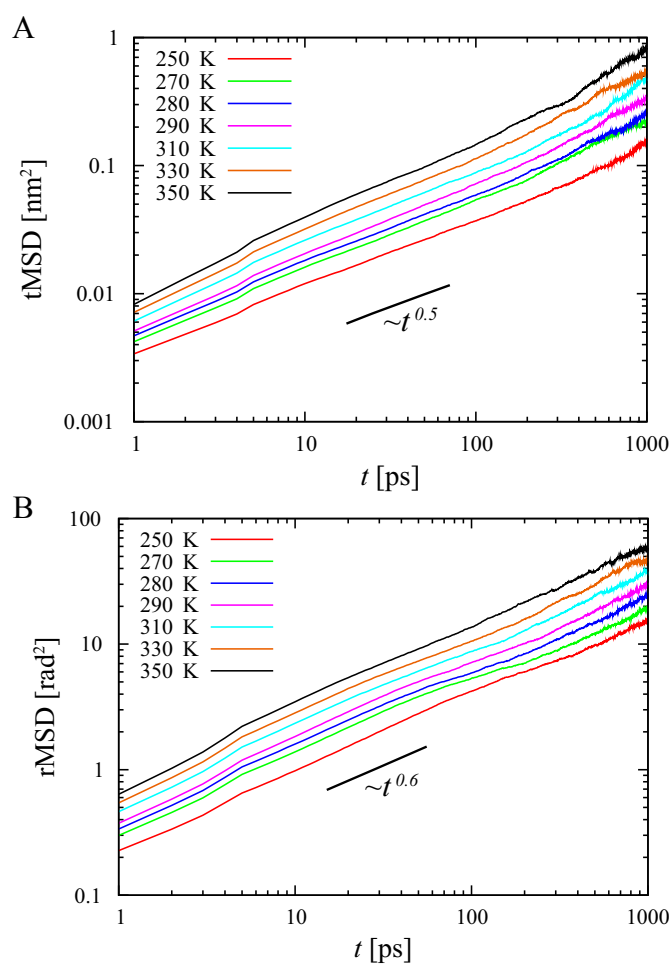


Fig. 3.9 Ensemble-averaged MSD of water molecules in the first layer, (A) translational and (B) rotational motions. The lines indicate a sublinear growth.

Chapter 4

Anomalous diffusion of water molecules on membrane surfaces

4.1 Introduction

In usual case, diffusion can be characterized by the ensemble-averaged MSD, i.e. $\langle \mathbf{r}^2(t) \rangle = 2dDt$, where D is the diffusion constant and d is a dimension. However, for example single-particle tracking experiments have shown subdiffusion to occur in living cells [130, 144–147]

$$\langle \mathbf{r}^2(t) \rangle \simeq 2dD_\alpha t^\alpha \quad \text{with} \quad 0 < \alpha < 1, \quad (4.1)$$

where α is the subdiffusive exponent and D_α is the generalized diffusion constant. Indeed, such “anomalous” dynamic behavior as subdiffusion is perhaps not anomalous but is rather widely observed in biological systems [148]. There are three well-known stochastic models of subdiffusion with different mechanisms [148]: continuous time random walk (CTRW) [149], fractional Brownian motion (FBM) [150, 151], and diffusion on a fractal lattice [152]. Because these models have different physical nature, revealing the origin is significant to understand physical properties [12, 148]. In particular, the physical origin of subdiffusion in living cells has been extensively studied [130, 145–147].

Here, we briefly introduce the CTRW and FBM mainly related to the topic of this chapter.

Subdiffusive continuous time random walk

In the CTRW model, the random walker has to be wait for a random waiting time τ drawn from the waiting time PDF $\psi(\tau)$. If the PDF is drawn with power-law

$$\psi(\tau) \simeq \frac{\tau_0^\alpha}{\tau^{1+\alpha}}, \quad (4.2)$$

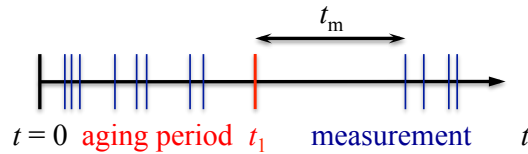


Fig. 4.1 Schematic view of observing the aging process. The process is renewed governed by the random waiting times with power-law distribution (blue lines). We start the measurement of the process at a time t_1 (aging period, red line) after start time of the process at $t = 0$. The waiting time for the first renewal after the time t_1 is t_m .

for $0 < \alpha < 1$, the mean of the waiting time diverges, and the diffusive motion shows subdiffusion. In what follows, we discuss the subdiffusive case of CTRW.

Ergodicity is a statistical term that the time average of all quantities for sufficiently long time is the same as the ensemble average. There is a discrepancy between the MSD and the time-averaged mean square displacement (TAMSD), i.e. weak ergodicity breaking [131, 153–155]. The mean of the TAMSD is given by

$$\langle \overline{\delta^2(\Delta; t)} \rangle \sim \frac{2D_\alpha}{\Gamma(1 + \alpha)} \frac{\Delta}{t^{1-\alpha}}, \quad (4.3)$$

in the limit $\Delta \ll t$. The TAMSD increases linearly, while MSD increases sublinearly, indicating ergodicity breaking. The TAMSD decreases when measurement time t increases. The longer the process goes on, the more the walker occasionally encounters longer time trappings, which affects the subdiffusive motion. Such long time trapping events typically increase according to an increase of the observation time t . Such aging phenomena of TAMSD, $\overline{\delta^2} \simeq 1/t^{1-\alpha}$, are observed for the diffusion of a potassium channel in the plasma membrane [130] and insulin granules in the cytoplasm [147].

We consider the aging process when we start to observe the random walker at a time t_1 after the walker starts to move at time $t = 0$ [see Fig. 4.1]. The PDF of the waiting time t_m for the first jump after the start time of the measurement at t_1 [156, 157] is given by

$$h(t_m; t_1) = \frac{\sin \pi \alpha}{\pi} \frac{t_1^\alpha}{t_m^\alpha (t_m + t_1)}. \quad (4.4)$$

When the aging period is enough longer $t_1 \gg t_m$, the scaling of the PDF $h(t_m; t_1) \simeq t_m^{-\alpha}$ is broader than that of the original one $\psi(\tau) \simeq \tau^{-1-\alpha}$.

The MSD in this aging process can be written as

$$\langle x^2(t; t_1) \rangle \sim D_\alpha [(t + t_1)^\alpha - t_1^\alpha]. \quad (4.5)$$

For times $t_1 \ll t$ we observe sublinear increase of the MSD, $\langle x^2(t; t_1) \rangle \sim D_\alpha t^\alpha$, while for times $t_1 \gg t$ the MSD shows apparent linear scaling with time t , $\langle x^2(t; t_1) \rangle \sim D_\alpha t_1^{\alpha-1} t$. Thus, as start time of the measurement t_1 increases, the MSD decreases.

From the TAMSD for the aging process

$$\overline{\delta^2(\Delta; t, t_1)} = \frac{1}{t - \Delta} \int_{t_1}^{t_1 + t - \Delta} \{x(t' + \Delta) - x(t')\}^2 dt', \quad (4.6)$$

the mean of the TAMSD results in

$$\langle \overline{\delta^2(\Delta; t, t_1)} \rangle \sim \frac{\Lambda_\alpha(t_1/t)}{\Gamma(1 + \alpha)} 2D_\alpha \frac{\Delta}{t^{1-\alpha}} = \Lambda_\alpha(t_1/t) \langle \overline{\delta^2(\Delta; t)} \rangle, \quad (4.7)$$

for $\Delta \ll t$, where $\Lambda_\alpha(z) = (1 + z)^\alpha - z^\alpha$. In the limit of strong aging $t_1 \gg t \gg \Delta$, we observe an equivalence of the MSD and the TAMSD

$$\langle \overline{\delta^2(\Delta; t, t_1)} \rangle \sim \frac{2D_\alpha}{\Gamma(1 + \alpha)} t_1^{\alpha-1} \Delta \sim \langle x^2(\Delta; t_1) \rangle. \quad (4.8)$$

Another feature of the CTRW is a large scatter of the TAMSDs, i.e. the amplitudes between different TAMSDs exhibit large variation. To characterize the scatter of the TAMSDs, relative standard deviation (RSD) is defined by

$$R(t; \Delta) \equiv \frac{\sqrt{\langle \overline{\delta^2(\Delta; t)}^2 \rangle - \langle \overline{\delta^2(\Delta; t)} \rangle^2}}{\langle \overline{\delta^2(\Delta; t)} \rangle}. \quad (4.9)$$

If the process is ergodic, the RSD of the TAMSDs converge to zero when the measurement time is long. In the case of the CTRW, non-ergodic case, the RSD of TAMSDs converge to a non-zero constant depending on the power-law exponent α of the waiting time distribution [153, 158]:

$$R(t; \Delta) \rightarrow \sqrt{\frac{2\Gamma^2(\alpha + 1)}{\Gamma(2\alpha + 1)} - 1}, \quad (t \rightarrow \infty), \quad (4.10)$$

for all $\Delta \ll t$. This means that the TAMSDs remain random variables even when the measurement time goes to infinity, which is totally different from the Brownian motion, FBM, or random walk on fractal lattice. Such a large scattering of TAMSDs is observed in the motion of mRNA molecules inside live *E. coli* cells [145], chromosomal loci in live bacterial cells [159], and lipid granules in living fission yeast cells [146].

Fractional Brownian motion

The stochastic integral term of the FBM was introduced by Mandelbrot and van Ness [151] to take into account correlations in a random walk

$$x(t) = \frac{1}{\Gamma([1 + \alpha]/2)} \left[\int_0^t (t - t')^{(\alpha-1)/2} dB(t') + \int_{-\infty}^0 \left\{ (t - t')^{(\alpha-1)/2} - (-t')^{(\alpha-1)/2} \right\} dB(t') \right], \quad (4.11)$$

where $dB(t)$ is the white Gaussian noise. In this model, the current state is influenced by the past state.

To be more intuitive, we consider the Langevin equation with the fractional Gaussian noise $\xi_{\text{fGn}}(t)$

$$x(t) = \int_0^t \xi_{\text{fGn}}(t') dt', \quad (4.12)$$

where the mean of the fractional Gaussian noise $\langle \xi_{\text{fGn}}(t) \rangle = 0$ and the covariance function is given by a power law

$$\langle \xi_{\text{fGn}}(t_1) \xi_{\text{fGn}}(t_2) \rangle = \alpha(\alpha - 1) K_\alpha^* |t_1 - t_2|^{\alpha-2}, \quad (4.13)$$

for $t_1, t_2 > 0$ and $t_1 \neq t_2$. The autocorrelation function of positions in the FBM is

$$\langle x(t_1)x(t_2) \rangle = K_\alpha^* (t_1^\alpha + t_2^\alpha - |t_1 - t_2|^\alpha). \quad (4.14)$$

At $t = t_1 = t_2$, we can observe the consistent of the MSD with mean of the TAMSD, i.e. the FBM is ergodic [160]:

$$\langle \overline{\delta^2(\Delta)} \rangle = 2K_\alpha^* \Delta^\alpha = \langle x^2(\Delta) \rangle. \quad (4.15)$$

The fractional Gaussian noise of Eq. (4.13) can describe both superdiffusion for positively correlated noise ($1 < \alpha < 2$) and subdiffusion for negatively correlated noise ($0 < \alpha < 1$). And the cases of $\alpha = 1$ and $\alpha = 2$ correspond to Brownian and ballistic diffusion, respectively.

In general, it is difficult to reveal the underlying mechanism of subdiffusion. Identification of ergodic and aging properties is one of the clues in clarifying the physical origin. It is known that the FBM motion is ergodic, whereas under confinement of an harmonic external potential $U(x) = kx^2/2$, we observe an exponential relaxation of the MSD for a model related to the FBM [161–163]

$$\langle x^2(t) \rangle \sim \langle x^2 \rangle_{\text{st}} - \frac{2}{k^2} \alpha(\alpha - 1) K_\alpha^* t^{\alpha-2} e^{-kt}, \quad (4.16)$$

and a power-law relaxation of the TAMSD

$$\overline{\delta^2(\Delta)} \sim 2\langle x^2 \rangle_{\text{st}} - \frac{K_\alpha^* \Gamma(1 + \alpha)}{k^\alpha} e^{-k\Delta} - \frac{2\alpha(\alpha - 1)K_\alpha^*}{k^2 \Delta^{2-\alpha}}, \quad (4.17)$$

where $\langle x^2 \rangle_{\text{st}} = K_\alpha^* \Gamma(1 + \alpha)/k^\alpha$, and in particular, $\overline{\delta^2(\Delta)} = 2\langle x^2 \rangle_{\text{st}}$ at $\Delta \rightarrow \infty$. Moreover, the FBM under the external confinement exhibits transient aging, where time and ensemble averages behave differently, i.e. transiently nonergodic [164]. Since the ordinary ergodicity, where the time average are equal to the ensemble average, holds for the FBM and diffusion on a fractal lattice [160,165], the dominant feature of CTRW with a divergent mean waiting time is aging and weak ergodicity breaking [131,153–155]. Such phenomena are also observed in a range of stochastic models different from the CTRW such as random walk with static disorder [166], random walks with correlated waiting times [167,168], spatially correlated random walks [169], aging walks [170], and stored-energy-driven Lévy flight [171].

Water molecules “near” the surface of lipid membranes were found to show transient subdiffusion [172,173]. They define the surface water molecules that are in a layer $(z, z + \Delta z)$ perpendicular to the membrane surface. They assume that the surface of the membrane is smooth despite the complex lipid membrane surface is undulating and fluctuating. The definition contains water molecules that are not associated with the lipid surface atoms. And to obtain enough ensembles, water molecules are harmonically constrained in the z direction [173].

Here, we focus on the water molecules which continuously interact with lipid molecules on the surface without any artificial forces. We investigate the subdiffusion of water molecules “on” membrane surfaces and the origin of the subdiffusive motion.

4.2 Methods

MD simulations of pure POPC or POPE bilayers were performed. Each lipid bilayer system consisted of 128 lipids (64 for each leaflet) and 7,680 TIP3P water molecules [see Fig. 4.2(A)]. The CHARMM36 [174] force field was used for the lipids. The TIP3P water model modified for the CHARMM force field [175] was used because the CHARMM36 force field was developed based on the TIP3P water models. Although the diffusion constant of TIP3P water model is higher than the experimental values, it reproduces the first-shell hydration and the energetics of liquid water [176]. The bond lengths involving the hydrogen atoms were constrained to

equilibrium lengths using the SHAKE method. The direct sum and Lennard-Jones interactions were smoothly truncated at a cutoff distance of 1.2 nm, using a switching function that becomes effective at 1.0 nm. The particle-mesh Ewald method was used for calculations of electrostatic interactions. Before MD simulations, energy minimization was performed using a conjugate gradient algorithm to remove the bad contacts of the initial configuration. Simulations were performed under constant NPT (number of particles, pressure, and temperature) with temperature 310 K and pressure 0.1 MPa. For temperature and pressure control, a Langevin thermostat and piston were used with a damping coefficient of 1 ps^{-1} and a collision period of 0.2 ps, respectively. The three orthogonal dimensions of the periodic cell were allowed to change independently in the x - y and z dimensions (semi-isotropic pressure coupling). Each simulation ran for 240 ns under 2.0 fs time-step increments; coordinates were recoded every 1.0 ps. The final system sizes of MD simulations of POPC and POPE bilayers are $0.66 \times 0.66 \times 0.88 \text{ nm}^3$ and $0.61 \times 0.61 \times 1.02 \text{ nm}^3$, respectively. The properties of each system were analyzed over the trajectories of the final 130 ns of each system. All MD simulations were performed using NAMD2.9 software [177].

4.3 Results and Discussion

4.3.1 Diffusion of water molecules on membrane surfaces

Water molecules forming the bridges connecting lipid molecules on the membrane surface do not diffuse. This bridge is formed by hydrogen bonds between the water molecules and head groups of the lipid molecules. These hydrogen bond interactions create a complicated and random potential surface over the membrane. To investigate the diffusivity of water molecules on the membrane surface, we define surface water molecules as water molecules for which the oxygens remain continuously within interatomic distances of 0.35 nm from atoms (oxygen, phosphorus, nitrogen, and carbon atoms) in the lipid molecules. In what follows, we use trajectories of the water and lipid molecules where the position of the center of mass of the membrane is subtracted.

First, we consider the survival probability of residence time of water molecules on the membrane surface, where the residence time is defined as the duration for which a water molecule remains on the membrane surface [see Fig. 4.2B]. The sur-

vival probability is defined by $F(t) = \int_t^\infty P(t')dt'$, where $P(t')$ is a PDF. The PDFs of the residence times follow power-law distributions with exponential cutoffs in their tails [see Fig. 4.3]. Mean residence times on POPC and POPE bilayers are 7.0 ± 36 ps and 9.3 ± 42 ps, respectively. Although almost all of the water molecules pass on the membrane surface without binding to the lipid molecules, we are interested in the water molecules diffusing on lipid membrane surfaces. This is because water molecules residing on the surface for long time can contribute to membrane stability by making water bridges and may have important role in many physiological processes.

Figure 4.2C shows a lateral trajectory of a water molecule residing on the POPE bilayer surface for 9 ns. Surprisingly, water molecules do diffuse widely on the membrane surface while residing on it. In other words, a water bridge connecting lipid molecules in a membrane is not fixed but dynamical. Indeed, diffusion distances on the membrane surface lengthen with increasing residence times. Figure 4.2D shows the probability that the maximal excursion distance for water molecules is greater than l_c , $P(r_{\max}^2(t) > 2l_c^2)$, where the maximal excursion distance is defined by $r_{\max}(t) = \max\{r(t') : 0 \leq t' \leq t\}$ with $r(t) = \sqrt{x(t)^2 + y(t)^2}$. About 40 % of water molecules that reside on the membrane surface over 600 ps can diffuse above 0.5 nm^2 . This implies that water molecules can diffuse beyond a lipid molecule in the membranes, because the area per lipid is about $0.5\text{-}0.7 \text{ nm}^2$. Some water molecules diffuse by interchanging the water bridge while remaining on the membrane surface. We found a water-bridge interchange dynamics for the first time.

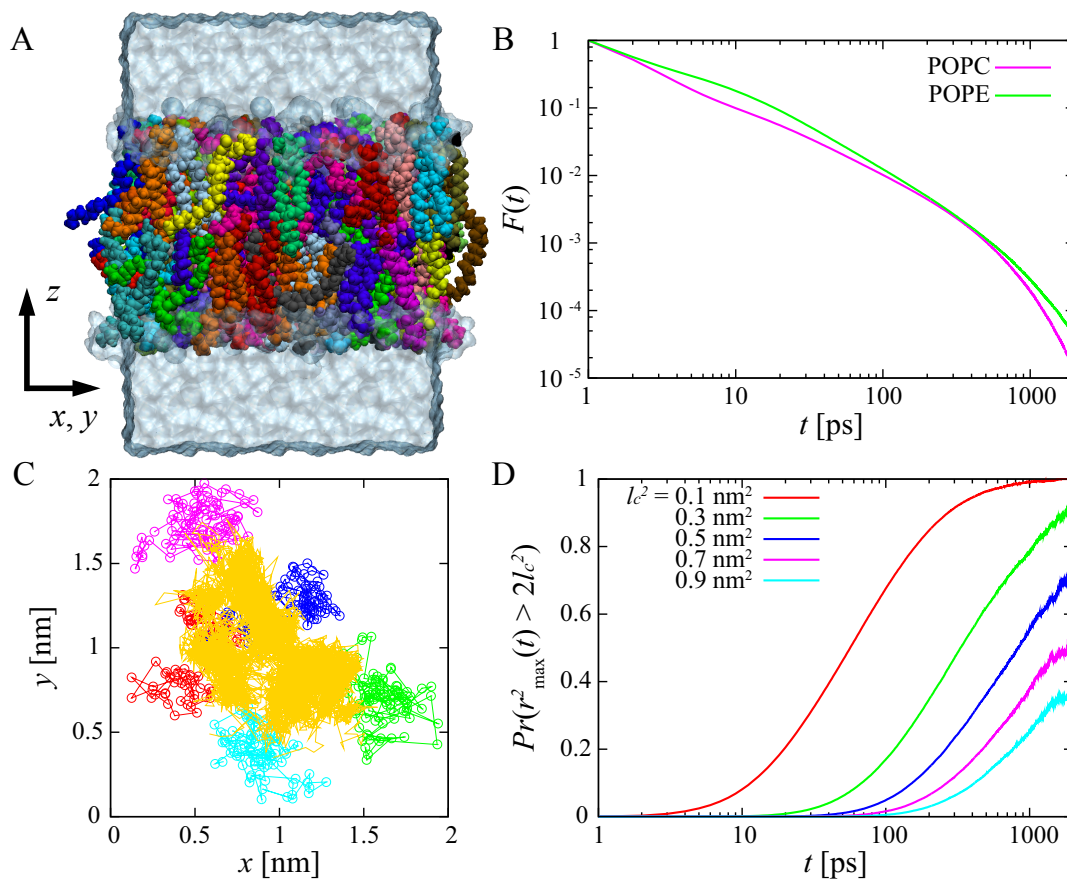


Fig. 4.2 Diffusion of water molecules on lipid membrane surfaces. (A) Configuration of POPC bilayer. Each color represents a different phospholipid. Explicit water molecules correspond to the upper and lower transparent coatings. (B) Survival probability of residence time of water molecules on the membrane surfaces. (C) Lateral trajectory of a water molecule (yellow) tracked for 9 ns on a POPE membrane surface. Circles with lines represent trajectories of different lipid molecules. (D) Fraction of water molecules traversing a certain distance l_c . Each color represents different l_c values.

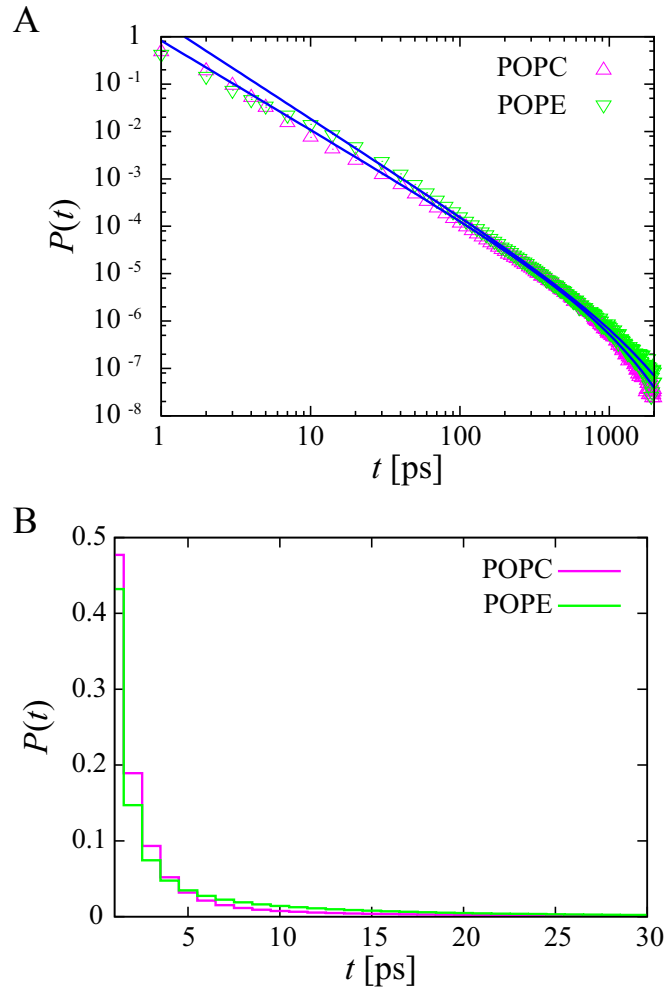


Fig. 4.3 Residence of water molecules on membrane surfaces. (A) PDFs $P(t)$ of residence time of water molecules on membrane surfaces. Solid lines are fitting curves by power-law distributions with exponential cutoffs: $P(t) = At^{-\beta} \exp(-t/\tau)$ (POPC: $\beta = 1.9$, $\tau = 780$, POPE: $\beta = 2.0$, $\tau = 1200$). The parameter A is a fitting parameter, not a normalization constant. (B) $P(t)$ in Cartesian coordinate.

4.3.2 Translational and rotational subdiffusion of water molecules on membrane surfaces

To investigate the diffusion of water molecules on the membrane surfaces, we consider translational as well as rotational diffusion of the water molecules. The ensemble-averaged lateral translational MSD (tMSD) is defined as

$$\langle l^2(t) \rangle = \frac{1}{2} \langle \{x(t+t_0) - x(t_0)\}^2 + \{y(t+t_0) - y(t_0)\}^2 \rangle, \quad (4.18)$$

where t_0 is the time when water molecules enter the membrane surfaces and $\langle \dots \rangle$ is the average with respect to captured and reflected water molecules impinging on the membrane surface. If exiting from the membrane surfaces, water molecules are excluded from the ensemble. In considering rotational diffusion, we define $\delta\theta(t) \equiv \cos^{-1}(\vec{\mu}(t) \cdot \vec{\mu}(t+\delta t))$ and direction $\vec{p}(t) \equiv \vec{\mu}(t) \times \vec{\mu}(t+\delta t)$, where $\vec{\mu}(t)$ is the dipole vector of a water molecule at time t . The vector $\vec{\varphi}(t) \equiv \int_{t_0}^{t_0+t} \delta\theta(t') \vec{p}(t') dt'$ gives us the trajectory representing the rotational motion. Then, the ensemble-averaged rotational MSD (rMSD) [143] is given by

$$\langle \varphi^2(t) \rangle = \langle |\vec{\varphi}(t) - \vec{\varphi}(0)|^2 \rangle. \quad (4.19)$$

In CTRW, the MSD is suppressed with increase of the starting time t_1 of a measurement [156]. This behavior is called *aging*. To investigate aging, we consider the dependence of the MSDs on the starting time of a measurement. Here, we consider $\text{tMSD}(t; t_1) = \langle \{x(t+t_0+t_1) - x(t_0+t_1)\}^2 + \{y(t+t_0+t_1) - y(t_0+t_1)\}^2 \rangle / 2$ and $\text{rMSD}(t; t_1) = \langle |\vec{\varphi}(t+t_0+t_1) - \vec{\varphi}(t_0+t_1)|^2 \rangle$, where t_1 corresponds to times after entering the membrane surface at t_0 . Figure 4.4 shows the MSDs measured after time t_1 from 0 to 200 ps. Translational motions of water molecules exhibit subdiffusion as in diffusion of lipid molecules [13, 14, 144, 178, 179] and peripheral membrane proteins [180]. Whereas the subdiffusive exponents in the tMSDs decrease as time t increases, the rMSDs show subdiffusion with a constant subdiffusive exponent. For tMSD and rMSD, water molecules on POPC bilayers are faster than those on POPE bilayers. This is because hydrogen bonds between choline groups and water molecules in POPC bilayers are weaker than those in POPE bilayers because methyl groups are present in the choline group of POPC. Moreover, as seen in Fig. 4.4, both tMSD and rMSD depend on the starting time of a measurement t_1 . Both MSDs become smaller the later t_1 becomes. For $t_1 > 50$ ps, unlike CTRW,

MSDs do not strongly depend on t_1 . Therefore, this aging will be affected by a non-equilibrium initial condition when water molecules attach to the membrane surfaces. We note that MSDs calculated after equilibration on membrane surfaces also decrease according to t_1 [see Fig. 4.5].

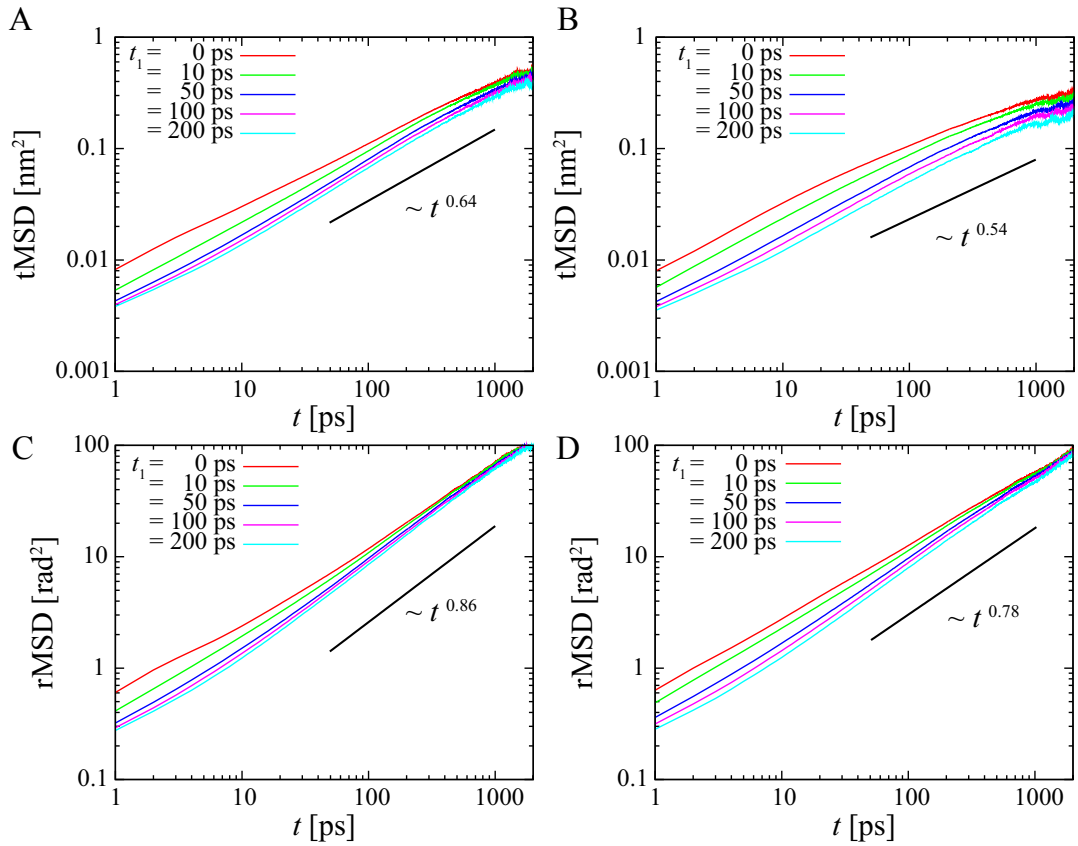


Fig. 4.4 Subdiffusion and aging of water molecules on membrane surfaces. (A) Ensemble-averaged tMSD and (C) rMSD of water molecules on a POPC membrane surface. (B) and (D) are the tMSD and rMSD on a POPE membrane surface. The slope of the solid lines are fitted in the time interval from 50 to 1000 ps for $t_1 = 200$ ps. The different colored lines correspond to different measurement starting times t_1 .

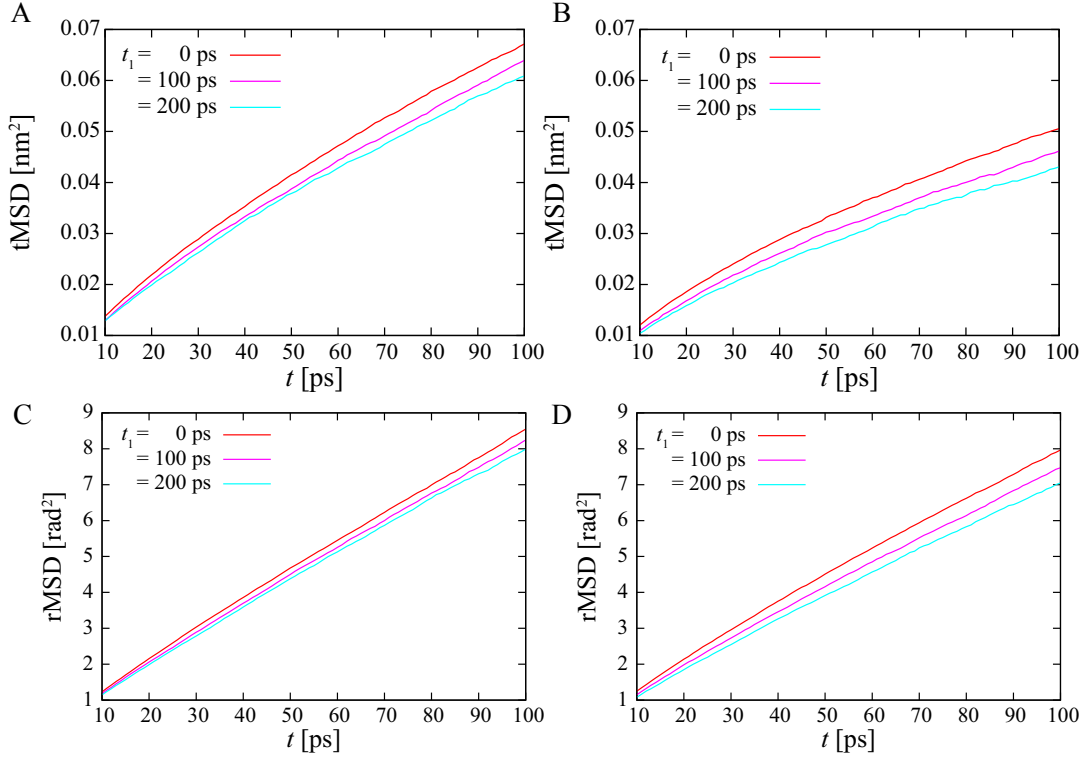


Fig. 4.5 Ensemble-averaged MSDs of water molecules with different measurement starting times. (A) Ensemble-averaged tMSD and (C) rMSD of water molecules on a POPC membrane surface. (B) and (D) are the tMSD and rMSD on a POPE membrane surface. We consider $\text{tMSD}(t; t_1) = \langle \{x(t + t_0 + t_1 + t_2) - x(t_0 + t_1 + t_2)\}^2 + \{y(t + t_0 + t_1 + t_2) - y(t_0 + t_1 + t_2)\}^2 \rangle / 2$ and $\text{rMSD}(t; t_1) = \langle |\vec{\varphi}(t + t_0 + t_1 + t_2) - \vec{\varphi}(t_0 + t_1 + t_2)|^2 \rangle$, where t_2 is a skipping time of non-equilibrium initial condition when water molecules attach to the membrane surfaces at t_0 , and t_1 corresponds to times after $t_0 + t_2$. Here, t_2 is 200 ps. The different colored lines correspond to different measurement starting times t_1 . After the non-equilibrium initial condition, MSDs decrease depending on t_1 .

4.3.3 Origin of subdiffusive motion of water molecules on membrane surfaces

To clarify the origin of subdiffusive motions of water molecules on membrane surfaces, we perform a mean maximal excursion (MME) analysis [181], i.e. measure the maximal distance covered by the particle up to time t after its initial release from the origin. The MME analysis provides us an information on the physical nature of the underlying subdiffusive processes by using trajectories only. In Figs. 4.6A and 4.7A, the translational and rotational MSDs, $\langle l^2(t) \rangle$ and $\langle \varphi^2(t) \rangle$, and the MME second moments, $\langle l^2(t)_{\max} \rangle$ and $\langle \varphi^2(t)_{\max} \rangle$, grow sublinearly with time, where $\langle l^2(t)_{\max} \rangle$ and $\langle \varphi^2(t)_{\max} \rangle$ are the ensemble averages of $l_{\max}(t) = \max\{l(t') : 0 \leq t' \leq t\}$ and $\varphi_{\max}(t) = \max\{\varphi(t') : 0 \leq t' \leq t\}$, respectively. For about $t > 30$ ps, the subdiffusive exponents of MSDs are almost the same as those of the MME second moment. This result suggests that a fractal or CTRW feature appears over relatively large-time intervals. Moreover, Figs. 4.6B and 4.7B show that the regular moment ratios $\langle l^4(t) \rangle / \langle l^2(t) \rangle^2$ and $\langle \varphi^4(t) \rangle / \langle \varphi^2(t) \rangle^2$ fluctuate above 2 except for $\langle \varphi^4(t) \rangle / \langle \varphi^2(t) \rangle^2$ around 1000 ps and that the MME moment ratios $\langle l^4(t)_{\max} \rangle / \langle l^2(t)_{\max} \rangle^2$ and $\langle \varphi^4(t)_{\max} \rangle / \langle \varphi^2(t)_{\max} \rangle^2$ fluctuate above 1.49. This result suggests CTRW scenario and excludes FBM and fractal scenarios. Figures 4.6C and 4.7C show that the probability for water molecules to be in a sphere of growing radius $r_0 t^{\alpha/2}$ is almost constant over t , while for rotational diffusion, the probability below 20 ps increases because of a change in the subdiffusive exponent. This result suggests CTRW or FBM scenarios and excludes fractal scenario. The above results are summarized in Table 4.1. These results strongly support the CTRW scenario for large-time intervals.

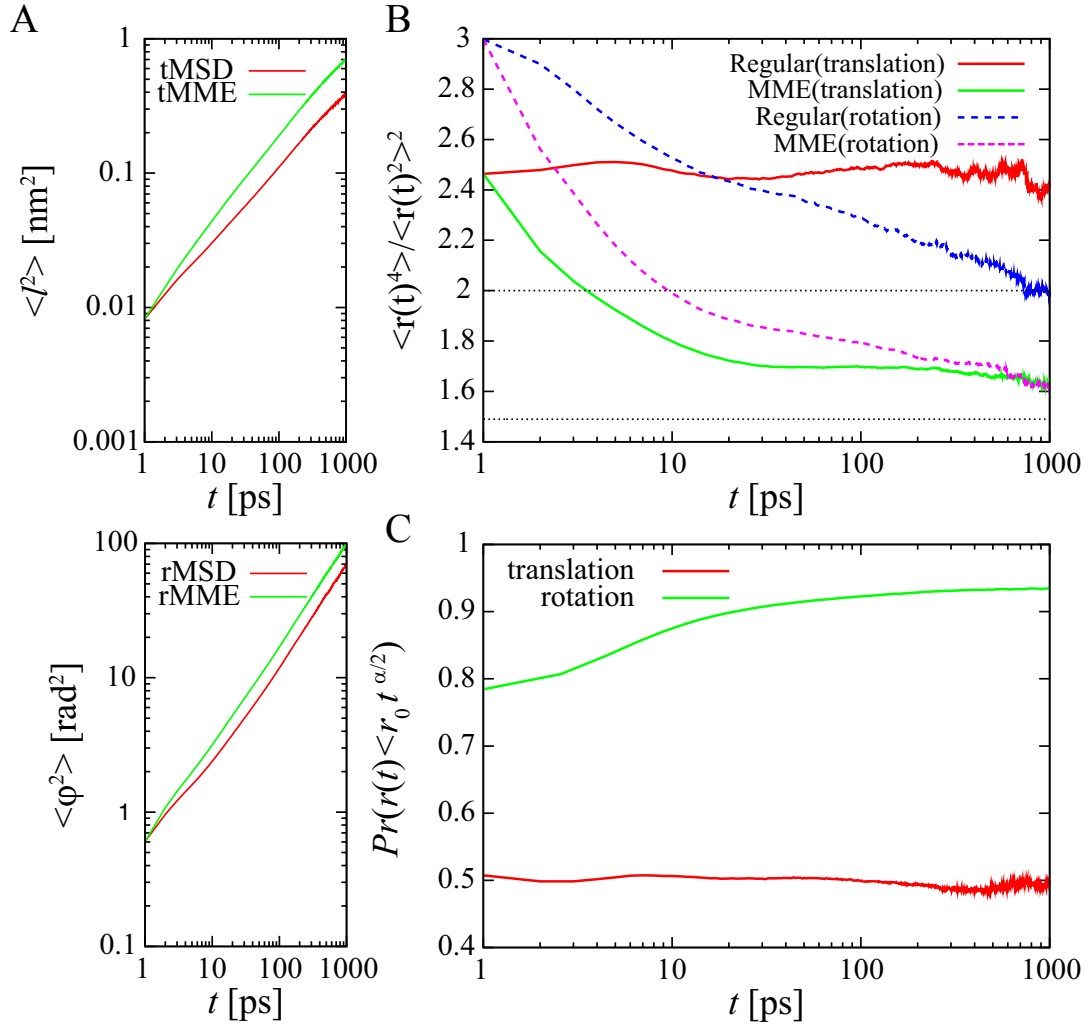


Fig. 4.6 Quantitative analysis of trajectories of water molecules on the POPC membrane surface. (A) MSD and second MME moment as functions of time t for translational and rotational diffusion. (B) Regular and MME moment ratios for translational and rotational motions. Horizontal lines are ratios 2 and 1.49. (C) Probability of water molecules to be in a sphere of growing radius $r_0 t^{\alpha/2}$. The value of α is based on fitted values 0.56 and 0.76 for translational and rotational motions in the time interval from 10 to 1000 ps for $t_1 = 0$ ps, respectively.

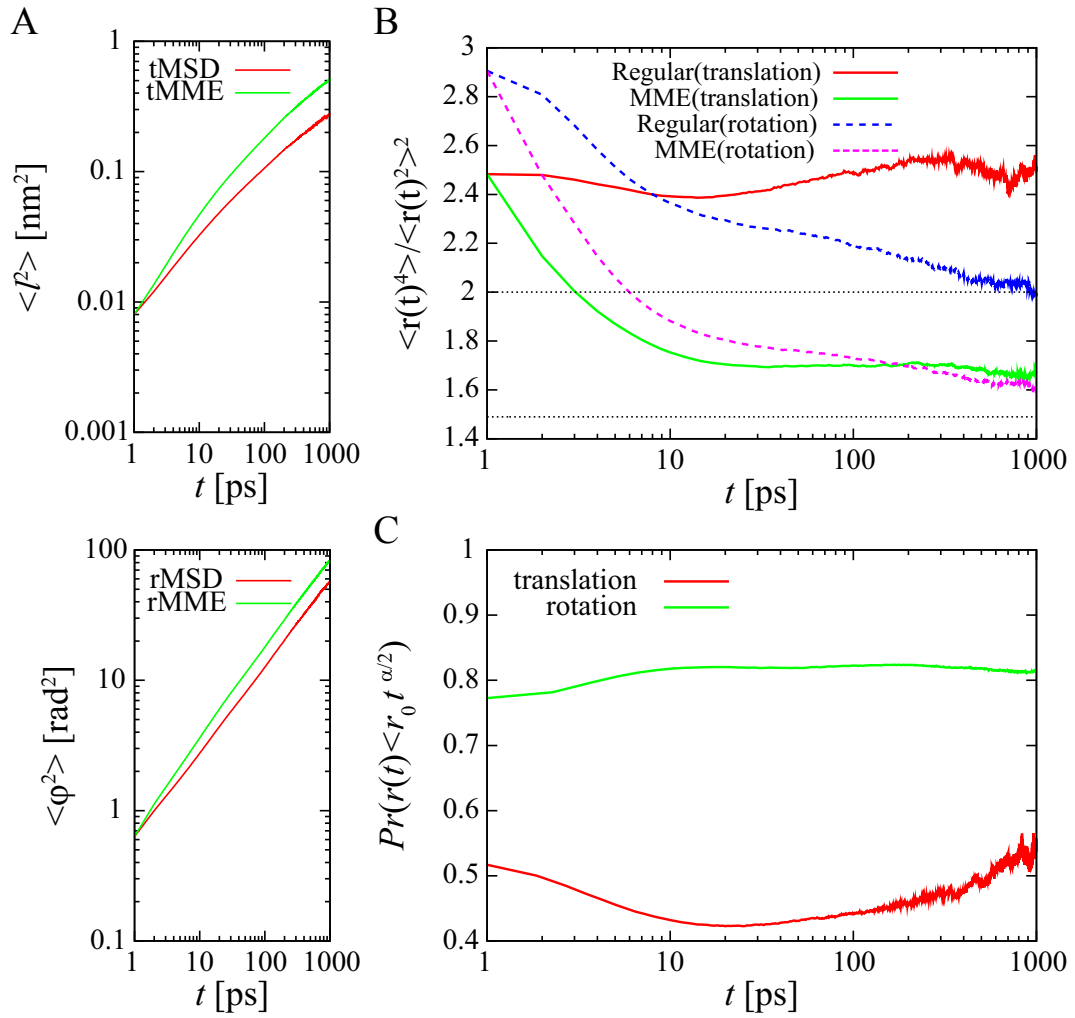


Fig. 4.7 Quantitative analysis on trajectories of water molecules on the POPE membrane surface. (A) MSD and second MME moment as function of time t for translational and rotational diffusion. (B) Regular and MME moment ratios about translational and rotational motions. (C) Probability to be in a growing sphere of radius $r_0 t^{\alpha/2}$. The α are based on the fitted values 0.5 and 0.66 for translational and rotational motions in the time interval from 10 to 1000 ps for $t_1 = 0$ ps, respectively.

To validate the CTRW scenario, we consider the TAMSDs defined by $\overline{\delta^2(\Delta; t)} = (\overline{\delta_x^2(\Delta; t)} + \overline{\delta_y^2(\Delta; t)}) / 2$ and $\overline{\delta_\varphi^2(\Delta; t)} = \frac{1}{t-\Delta} \int_0^{t-\Delta} |\vec{\varphi}(t' + \Delta) - \vec{\varphi}(t')|^2 dt'$ for translational and rotational motions, respectively, where t is the measurement time and $\overline{\delta_x^2(\Delta; t)} = \int_0^{t-\Delta} \{x(t' + \Delta) - x(t')\}^2 dt' / (t - \Delta)$. TAMSDs for trajectories of water molecules residing on the surface of the membrane longer than 2000 ps for both translational and rotational motions are shown in Figs. 4.8AB and 4.9AB. Unlike CTRW, where the TAMSD grows linearly with Δ , TAMSDs do not show a linear scaling over short-time durations. Because the TAMSD shows subdiffusion in FBM, i.e. sublinear scaling of Δ , translational and rotational motions have a FBM characteristic over short-time durations of Δ . However, rotational TAMSDs show normal diffusion (linear scaling of Δ) as expected by CTRW, whereas translational TAMSDs do not show normal diffusion. The mean rotational TAMSDs crossover from sublinear to linear [see Fig. 4.10]. The crossover points at around 10 ps are coincident with the relaxation time for the orientational correlation functions of water molecules on the membrane surfaces [see Fig. 3.7]. Because the sublinear growth of the TAMSDs suggests FBM, the dynamics of water molecules will be affected by viscoelasticity.

Figures 4.8CD and 4.9CD show the aging plots for translational and rotational TAMSDs on the POPC membrane surface, i.e. the ensemble average of the TAMSD as a function of the measurement time t , for different measurement starting times t_1 . Whereas the ensemble averages of translational and rotational TAMSDs show power-law decays: $\langle \overline{\delta^2(\Delta; t)} \rangle \propto t^{-\gamma_1}$ and $\langle \overline{\delta_\varphi^2(\Delta; t)} \rangle \propto t^{-\gamma_2}$ for $t_1 < 50$ ps, those show little decay for $t_1 > 50$ ps. In CTRW, the ensemble average of a TAMSD decays as $\langle \overline{\delta^2(\Delta; t)} \rangle \propto t^{-(1-\alpha)}$ [153], where α is the power-law exponent for the trapping-time PDF. However, recently, it is shown that CTRW with strong noisy fluctuations do not show the aging of TAMSD, whereas MSD still shows aging [182]. Thus, the power-law decays of ensemble average of TAMSDs for $t_1 < 50$ ps are attributed to non-equilibrium initial conditions of water molecules on the membrane surfaces, in other words, the initial condition is like a state of a collision with a wall. This is because mean velocity of bulk water molecules is higher than those on the membrane surfaces. Moreover, the longer water molecules reside on the membrane surfaces, the more water molecules have chance to be buried into phosphate and glycerol groups. We note that MSDs show aging in our simulations even when an initial non-equilibrium state is skipped (see Fig. 4.5).

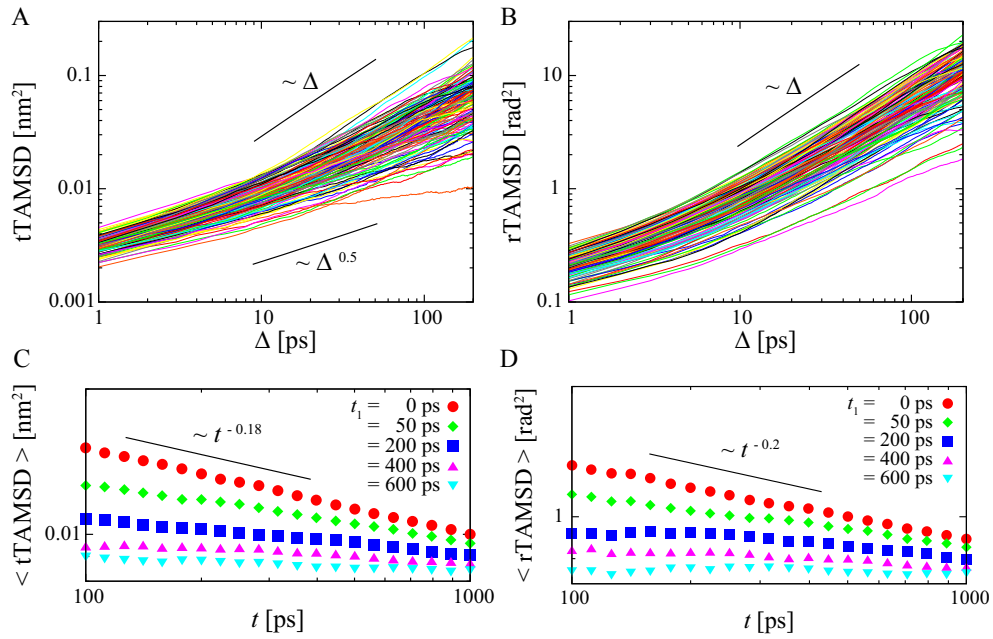


Fig. 4.8 (A) Translational and (B) rotational TAMSDs of water molecules on the POPC membrane surface. The different colored lines show 128 trajectories of water molecules. (C) Aging plot for translational and (D) rotational TAMSD for $\Delta = 10$ ps. The different colored symbols correspond to different measurement starting times t_1 . For reference, the power-law decays are represented by solid lines.

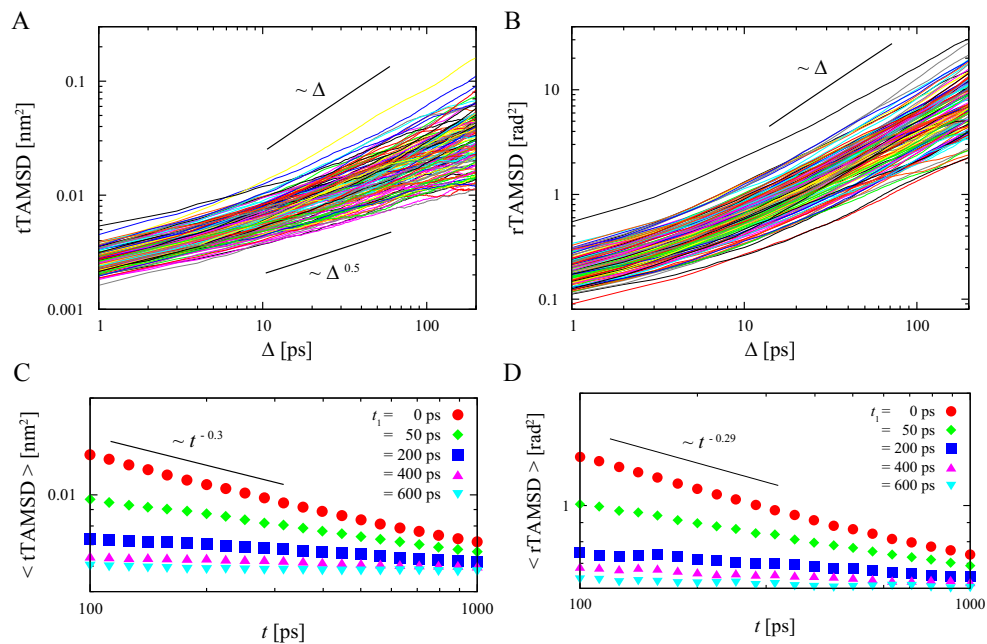


Fig. 4.9 (A) Translational and (B) rotational TAMSDs of water molecules on the POPE membrane surfaces. The different colored lines show 128 trajectories of water molecules. (C) Aging plot for translational and (D) rotational TAMSDs for $\Delta = 10$ ps. The different colored symbols correspond to different measurement starting times t_1 .

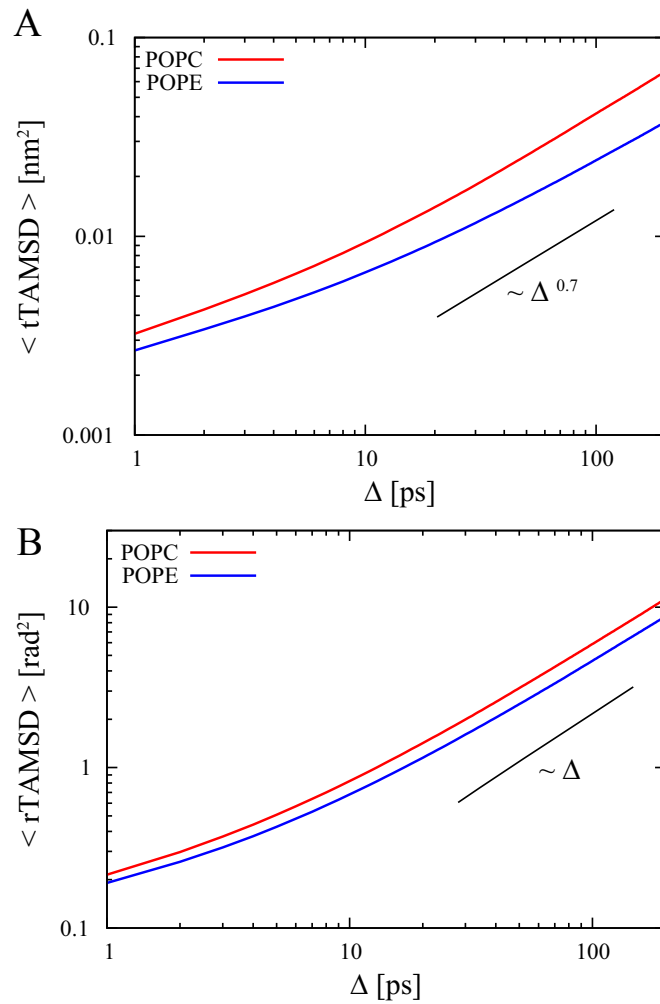


Fig. 4.10 (A) Mean TAMSD of translational and (B) rotational motion of water molecules on the lipid membrane surfaces. Translational mean TAMSDs are sublinear, which suggests FBM. Rotational mean TAMSDs are sublinear in short-time region, while they become normal for $\Delta > 20$ ps. This suggest that rotational motions obey FBM in short region and CTRW in large region $\Delta > 20$ ps.

Figure 4.11 shows the RSDs [Eq. (4.9)] for translational and rotational TAMSDs of water molecules residing on the membrane surfaces longer than 2000 ps. At the time scale of subdiffusion, the RSDs of TAMSDs do not converge to a non-zero constant but are decreasing monotonically, and are not consistent with Eq. (4.10). We think that this is because CTRWs with noisy fluctuations also show a similar behavior.

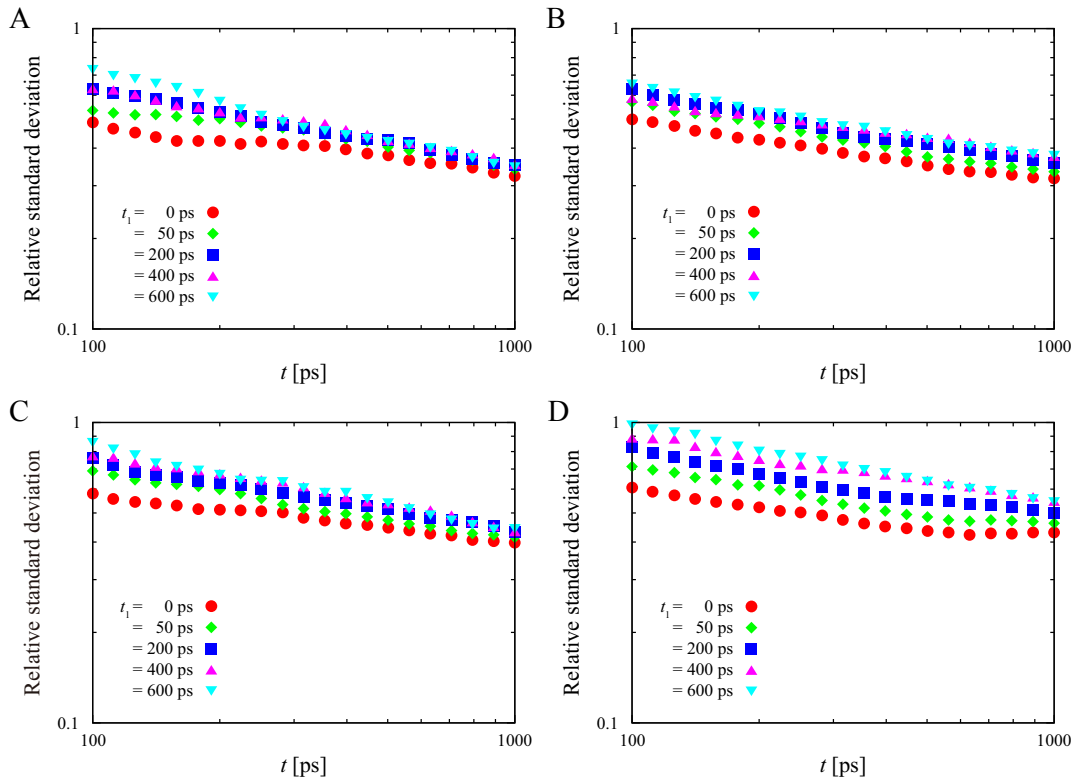


Fig. 4.11 Relative standard deviation of TAMSDs. RSDs of (A) translational and (C) rotational TAMSDs of water molecules on the POPC membrane surface. RSDs of (B) translational and (D) rotational TAMSDs of water molecules on the POPE membrane surface. All are done for $\Delta = 10$ ps. The different colored symbols correspond to different measurement starting times t_1 .

Table 4.1 Summary of confirming the origin of subdiffusive motions

Analysis	Translational
Second moment (regular, MME)	Fractals or CTRW [$\propto t^\alpha, \propto t^\alpha$]
Ratio (regular, MME)	CTRW [$> 2, > 1.49$]
Growing spheres	CTRW or FBM [$\Pr(r \leq r_0 t^{\alpha/2}, t) = A_0$]
TAMSD	FBM

Analysis	Rotational
Second moment (regular, MME)	Fractals or CTRW [$\propto t^\alpha, \propto t^\alpha$]
Ratio (regular, MME)	CTRW [$> 2, > 1.49$]
Growing spheres	CTRW or FBM [$\Pr(r \leq r_0 t^{\alpha/2}, t) = A_0$]
TAMSD	CTRW and FBM

Together with the MME analysis, it is physically reasonable to consider that the origin of the observed subdiffusion is a combination of CTRW and FBM. Although we do not provide a distinct evidence of constant aging effect, results in noisy CTRW [182] assist a suggestion that aging due to CTRW is inherent in water dynamics on the membrane surfaces. Readers may confront the question whether the observed CTRW feature could be due to the non-equilibration of the MD simulations. We note that non-equilibrium conditions of water molecules on the membrane surface are compatible with an equilibration of the total system. As shown in Fig. 4.12, total systems are equilibrated whereas TAMSDs show apparent aging [see aging plot in Fig. 4.8]. This apparent inconsistency can be resolved by dissociation of water molecules from the membrane surfaces. In fact, because water molecules can dissociate from the membrane surfaces and the mean residence time is finite, the system can be equilibrated.

The distribution of waiting times contributes to CTRW arising from random binding and unbinding of water molecules from the lipid surface. Moreover, translational motions of water molecules forming the water bridge are affected by lipid motions in lipid membranes which are governed by FBM motions [13, 14, 179]. Unlike CTRW, where a trapped state simply does not move, it is difficult to estimate exact trapping times in such situations. Figure 4.13 shows the PDFs of translational and rotational exit time of water molecules on the membrane surfaces with two types of thresholds. Although the PDF of exit times is known to be follow a power-law distribution with a divergent mean in CTRW, the PDFs $P(t)$ of exit

times on the membrane surfaces do not follow power-law distributions. The shapes of the PDFs strongly depend on the threshold value. It is difficult to determine the shape of the PDF for large l_c and θ in the situation such that particles can move during a trapped state. We think that a power-law distribution is invisible because water molecules on the membrane surface can move during a trapped state. We also confirmed that there are no significant differences in the water behavior on both POPC and POPE lipid membranes.

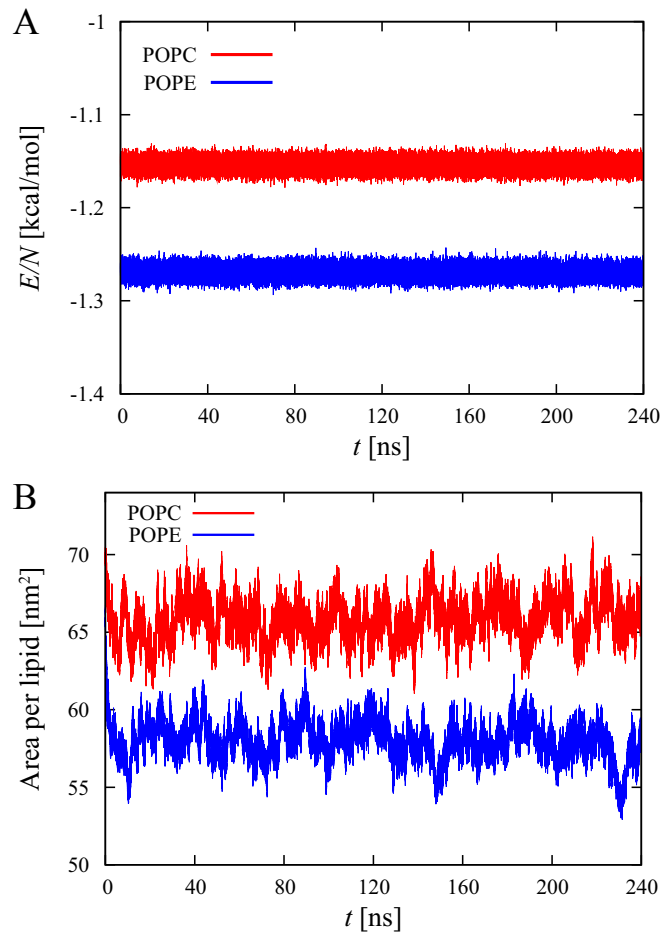


Fig. 4.12 Equilibration of the systems. (A) Surface area per lipid versus time for the two lipid systems. (B) Total energy per particle versus time for the two lipid systems. The areas per lipid and total energies per particle fluctuate around each constant value, which means that the systems are in an equilibrium.

In summary, we have shown that water molecules on membrane surfaces can diffuse laterally while connected as part of a bridging network to lipid molecules in membrane. This interchanging dynamics in the water bridge network can be

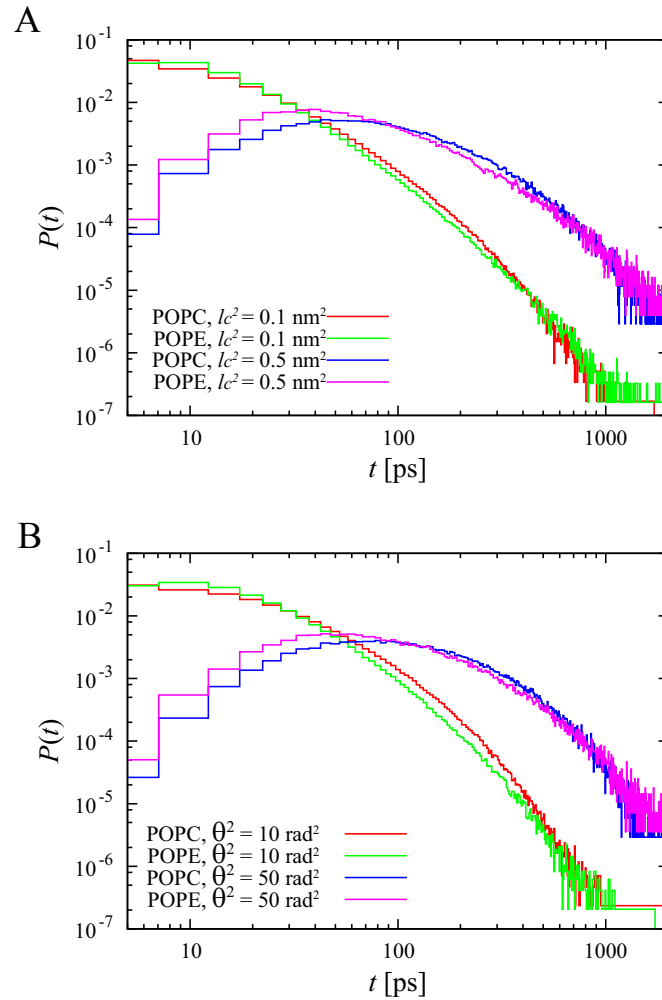


Fig. 4.13 Exit times of water molecules. PDFs of (A) translational and (B) rotational exit times of water molecules on the lipid membrane surfaces. Different color lines represent the differences of lipid membrane and thresholds.

described by CTRW. Furthermore, we have found translational and rotational subdiffusion of water molecules on the membrane surfaces. These subdiffusion originate from a combination of CTRW and FBM, which are attributed to long-time trapping by the membrane surface and viscoelasticity of lipid bilayers, respectively. Such a subdiffusive process has been observed in experiments of intracellular transport of insulin granules [147].

What is a biological significance of subdiffusion and aging phenomena of water molecules on cell membrane surfaces? Because subdiffusion and aging mean the diffusivity decreases as time passes, these phenomena cause water retardation and increase the chance of water binding on the membrane surfaces. As a result, water

molecules form bridges that connect lipid molecules and stabilize cell membranes. Moreover, the water retardation may contribute to higher efficiency of biological reactions on cell membranes. To recognize and bind to a target, biomolecules diffuse slowly around the target, and may be guided by the behavior of water molecules in the target vicinity [19]. For example, water retardation around a metalloenzyme active site assists enzyme-substrate interactions [183]. In a stochastic model, the probability of finding a nearby target is explicitly increased by subdiffusion [184]. Biological reactions such as ligand-receptor interactions and enzymatic reactions occur on cell membranes. Those depend upon encounters between biomolecules, and the structure and dynamics of water molecules in the hydration layer on the membranes. The water environment around the cell membranes produced by the anomalous diffusion of water molecules may have biological significance.

Chapter 5

$1/f$ noise in hydration dynamics on lipid membrane surfaces

5.1 Introduction

In numerous natural systems, the power spectra $S(f)$ exhibit enigmatic $1/f$ noise:

$$S(f) \propto \frac{1}{f^\beta} \quad (0 < \beta < 2). \quad (5.1)$$

at low frequencies. In biological systems, $1/f$ noise has been reported for protein conformational dynamics [185,186], fluctuations of an extended DNA molecule [187], DNA sequences [188], biorecognition [189], and ionic currents [190–193], implying that long-range correlated dynamics underlie biological processes.

There are many mathematical models that generate $1/f$ noise including stochastic models [151, 194–196] and intermittent dynamical systems [197–200]. The power-law residence time distribution is one of the most thoroughly studied origins for $1/f$ noise [195, 197–200]. In dichotomous processes, the power spectrum shows $1/f$ noise when the distribution of residence times of each state follows a power-law distribution with divergent second moment. For blinking quantum dots, which show a $1/f$ spectrum, residence times for “on” (bright) and “off” (dark) states have been experimentally shown to have a power-law distribution with a divergent mean [126, 201]. In stochastic models, this divergent mean residence time violates the law of large numbers which causes the breakdown of ergodicity, non-stationarity, and aging [153, 155, 166, 171, 202, 203]. On the other hand, the divergent mean residence time implies an infinite invariant measure in dynamical systems [204] and that the time-averaged observables are intrinsically random [204, 205].

Although little is known about the hydration dynamics, it is important to un-

derstand the dynamics of resident water molecules because these water molecules may play important roles in the overall dynamics of the membrane, and will affect membrane stability and biological reactions. In fact, such water molecules stabilize the assembled lipid structures [54]; this water retardation increases the efficiency of biological reactions [19, 183]. Water molecules enter and exit the hydration layer, and the number of water molecules near the lipid head group fluctuates.

Here, we perform MD simulations on water molecules plus pure lipid membrane at 310 K to investigate the hydration dynamics on the lipid surface. We find that fluctuations in the number of water molecules on the lipid surface show $1/f^\beta$ noise with $\beta > 1$ at high frequencies, and that the residence time distributions for “on” and “off” states follow power-law distributions with exponential cutoffs. Moreover, we construct a dichotomous process from the trajectory of the number of water molecules on a lipid molecule to clarify the origin of the $1/f$ noise. By analyzing the constructed dichotomous process, we find that there is a long-term correlation between residence times, which contributes to the $\beta > 1$ at high frequencies.

5.2 Methods

5.2.1 Molecular dynamics simulations

Additional MD simulation of complex POPC/palmitoyl-oleoyl-phosphatidylserine (POPS) bilayer was performed to clarify the universality of the hydration dynamics on the lipid membrane surfaces. The POPC/POPS (4:1) lipid system of 100 POPC lipids and 28 POPS lipids was solvated with 7,552 TIP3P water molecules, and NaCl ions at 150 mM concentration were added to neutralize the system. The simulation conditions were the same as that in Chapter 4.

Moreover, to confirm the universality of results, we changed water models, force fields, thermostat, and barostat. We performed a 1.14 μs MD simulation of the membrane system which has 128 POPC molecules and 7,823 SPC water molecules [206] using GROMACS-4.5.5 software [207]. The GROMOS96 53a6 force field [208], which is a united-atom model, was used for the POPC lipid. The pressure of 1 bar and a temperature of 310 K were controlled using the Parrinello-Rahman barostat [209] and velocity rescaling method [210] with a coupling time of 1 ps and 0.1 ps, respectively. The lengths of bonds involving the hydrogen atoms were constrained to equilibrium lengths using the LINCS

method [211]. The time step was set at 2 fs. The particle-mesh Ewald method was used for long-range electrostatic interactions. A cut-off distance of 1 nm was used for the van der Waals interactions.

5.2.2 Degree of non-Markovianity

The degree of non-Markovianity [192] is given by

$$G(\Delta, T) = \left[\frac{1}{T} \frac{1}{M^2} \sum_{i,j}^M \int_{\Delta}^{\Delta+T} D_{i,j}^2(t, \Delta) dt \right]^{1/2}, \quad (5.2)$$

where M is the total number of the states ($M = 2$ in our case), T is the range of the time Δ and t , and

$$D_{i,j}(t, \Delta) = P(i, t|j, 0) - \sum_{k=1}^M P(i, t|k, t - \Delta)P(k, t - \Delta|j, 0), \quad (5.3)$$

where $P(i, t|j, s)$ is the transition probability that the current state at the time t is in the state number i under the earlier state at the time s was in the state number j . The value of G strongly depends on the number of ensemble for calculating the transition probabilities. For calculating the transition probability, 128 dichotomous processes were divided into 100 segments. Thus, we used 12,800 data at each time step for calculating the conditional probabilities. The shuffled dichotomous processes were generated by shuffling the residence times for “on” and “off” states among themselves randomly. We generated the Markov dichotomous process where each state is generated independently with equal probability ($p = 1/2$). The $P(i, t|j, s)$ for the Markov dichotomous process was calculated by using the same number of ensemble 12,800. All $G(\Delta, T)$ were calculated for $T = 600$ ps.

5.3 Results and Discussion

5.3.1 Fluctuations of water molecules on the lipid head group

To investigate the hydration dynamics on the lipid membrane surfaces, we recorded the number of water molecules for which the oxygen was within interatomic distances of 0.35 nm [57, 212], which corresponds to the hydrogen bond distance, from all atoms in lipid head group [see Fig. 5.1A]. The number fluctuates around the average of about 14. Figure 5.1B shows the ensemble-averaged power spectra density

(PSD) of the water molecules calculated for the 128 lipid molecules in the POPC lipid bilayer. We have $S(f) \propto f^{-\beta}$ with $\beta = 1.35 \pm 0.05$ at high frequencies, while below a transition frequency ($f_t = 0.3$ GHz) PSD becomes a plateau at low frequencies. This crossover phenomenon is essential because $S(f) \propto f^{-\beta}$ with $\beta \geq 1$ implies non-integrability and non-stationarity. The observation of the plateau means that the measurement time is long enough. The time scale of the $1/f$ noise is longer than 100 ps ($f = 10^{10}$ Hz). Mean residence time of water molecules on the membrane surface is 7-71 ps depending on the binding sites and definitions of hydrated molecules [54, 56, 57], which is shorter than the time scale of the $1/f$ noise. Moreover, 80 % of water molecules which continuously reside on the membrane surface more than 1 ns move beyond 0.6 nm^2 [see Fig. 4.2]. The area per lipid is about $0.5\text{-}0.7 \text{ nm}^2$. Thus, most of the water molecules are displaced on the membrane surface by exchanging hydrogen bond interactions with lipid molecules in the time scale of the $1/f$ noise. We have confirmed that fluctuations of the number of water molecules within a box and a sphere near the membrane surfaces also exhibit $1/f$ noises but this is not the case for bulk [see Fig. 5.2].

A similar transition of the power-law exponent of the PSD has also been observed for the interchange dynamics of “on” and “off” states for quantum dot blinking [213]. This behavior was described theoretically using an alternating renewal process, where the residence time distributions of “on” and “off” states are given by a power-law with an exponential cutoff $\psi_{\text{on}}(\tau) \propto \tau^{-1-\alpha} e^{-\tau/\tau_{\text{on}}}$ and a power-law $\psi_{\text{off}}(\tau) \propto \tau^{-1-\alpha}$ with $\alpha < 1$, respectively [213]. The transition frequency f_t is related to the exponential cutoff in the quantum dot blinking experiment. In this case, the PSD exhibits aging, non-stationarity, and weak ergodicity breaking because the “off” time does not have a finite mean. To confirm whether the aging effect appears in the hydration dynamics on the lipid surface, we calculate the ensemble-averaged PSDs for different measurement times [Fig. 5.1C]. The magnitudes of the PSDs do not depend on the measurement time t , i.e. there is no aging. It follows that the power-law distribution with an exponential cutoff considered in [213] cannot explain hydration dynamics on the lipid membrane surfaces.

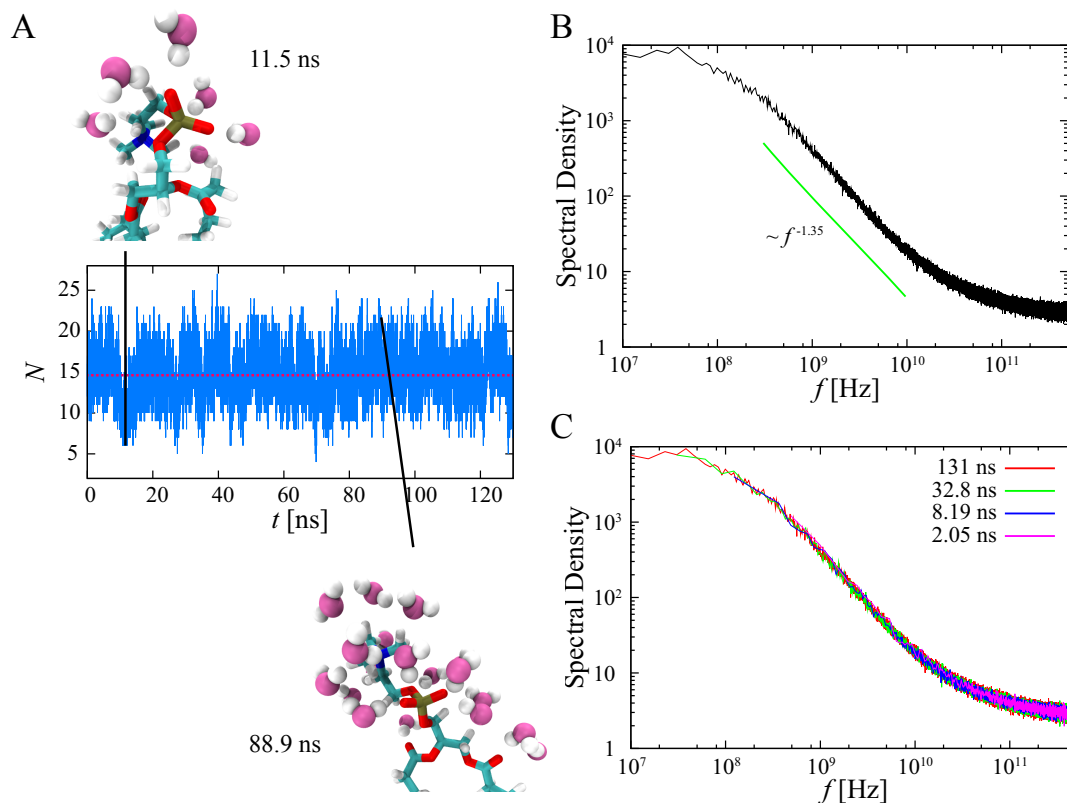


Fig. 5.1 Fluctuation of number of water molecules on the POPC membrane. (A) Time series of number of water molecules on a lipid head group. The red dashed line is the average number of water molecules on the lipid head group over this time period. The outer windows show snapshots of water molecules around the lipid head group. (B) Ensemble-averaged PSD of number of water molecules. We use 128 time series to obtain the ensemble-averaged PSD. The solid lines represent power-law behavior for reference. Total measurement time was 131 ns. (C) Ensemble-averaged PSD for four different measurement times: 2.05, 8.19, 32.8, and 131 ns. The power spectra coincide without fitting.

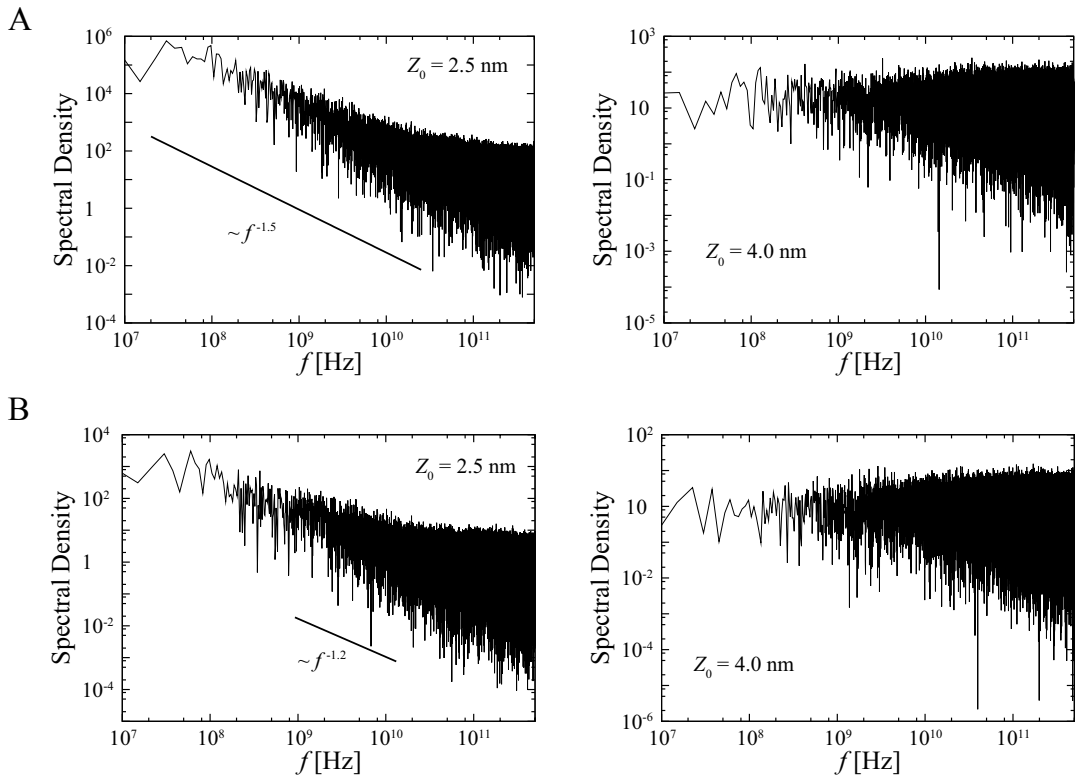


Fig. 5.2 Ensemble-averaged PSD of number of water molecules in regions near the POPC membrane surface. (A) Box (size is $l_x \times l_y \times l_z = 3 \times 3 \times 0.7$ nm³) and (B) sphere (radius is $r = 0.35$ nm³). The centers of the box and sphere are located at a perpendicular diastase Z_0 from the center of mass of the membrane. $Z_0 = 2.5$ nm is around the surface of the membrane. The fluctuations at $Z_0 = 4.0$ nm are white Gaussian noise.

5.3.2 Origin of the $1/f$ noise

One important question remains unclear: What is the origin of the $1/f$ noise? In other words, does power law intermittency or long-term memory contribute to the $1/f$ noise? To consider the origin of $1/f$ noise, we constructed a dichotomous (two states) process from the time series of the number of water molecules, where a state is called “on” ($N' = 1$) state when the number of water molecules on each lipid molecule is above the average number and “off” ($N' = -1$) state otherwise [Fig. 5.3A]. Figure 5.3B shows the ensemble-averaged PSD for the time series of constructed dichotomous processes. The obtained $1/f$ noise is the same as the ensemble-averaged PSD for the original time series [see Fig. 5.1B]. The PSD of the dichotomous processes also does not show aging [Fig. 5.3C].

To confirm a presence of a long-term memory, we calculate the ensemble-averaged PSD for shuffled dichotomous processes, where residence times for “on” and “off” states were shuffled among themselves randomly. Because shuffled dichotomous processes do not have a long-term correlation between residence times, we can clarify the existence of a long-term correlation. The ensemble-averaged PSD of the shuffled dichotomous processes exhibits $1/f$ noise and plateau at low frequencies [Fig. 5.4B]. However, the power-law exponent of $S(f) \propto f^{-\beta}$ at high frequencies changes from the original one (1.35) to 0.8. The frequency at which the PSD becomes a plateau is the same order of that of the original dichotomous process in Fig. 5.3B. This means that the long-term memory in residence times affects the power-law exponents of the original PSD.

Figure 5.4A shows PDFs of residence times for “on” and “off” states. Both PDFs follow power-law distributions with exponential cutoffs, $P(\tau) = A\tau^{-1-\alpha} \exp(-\tau/\tau_c)$, where the power-law exponent is $\alpha = 1.2$, and cutoffs for the PDFs of the “on” and “off” states are $\tau_c = 59$ ps and 1074 ps, respectively. The observed exponent, $\alpha > 1$, implies that mean residence time does not diverge and is consistent with the ergodic behavior (no aging). Following our observations, we performed a numerical simulation in which time series of “on” and “off” states were generated with random waiting times drawn from a power-law distribution with an exponential cutoff ($\alpha = 1.2$, on: $\tau_c = 60$ ps, off: $\tau_c = 1000$ ps). The PSD of the numerical simulation is well consistent with that of the shuffled dichotomous process [see Fig. 5.4B]. In alternating renewal process, the power-law exponent β

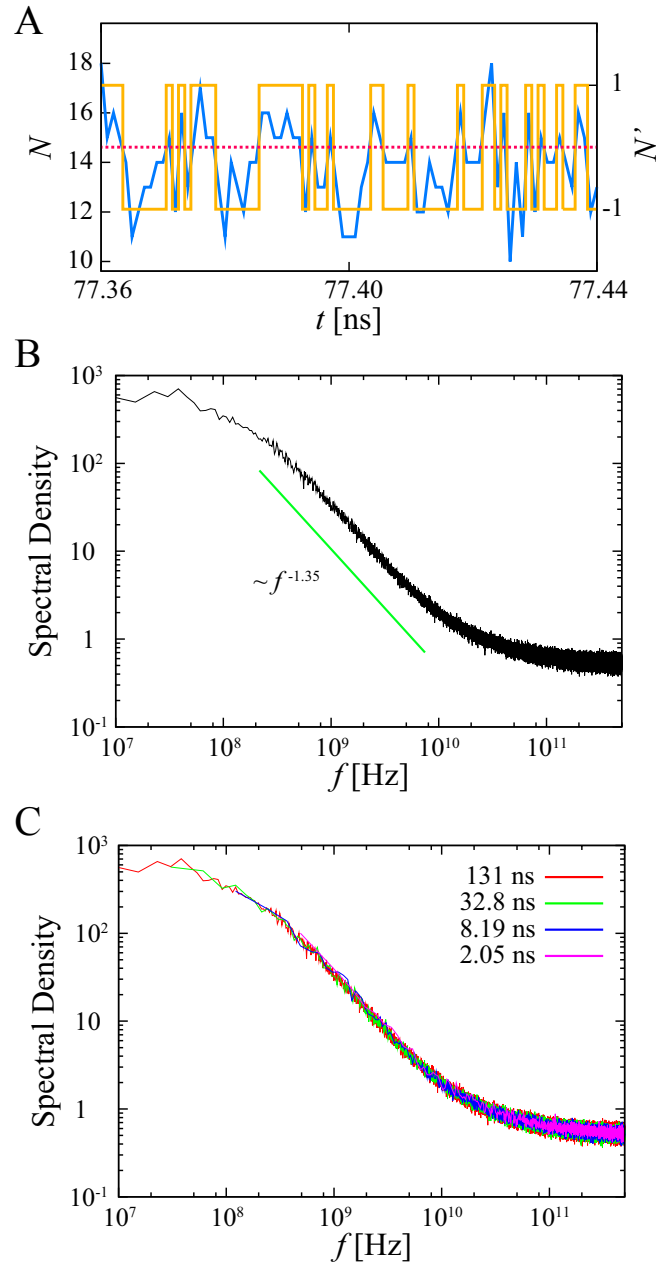


Fig. 5.3 $1/f$ noise in dichotomous process on the POPC membrane. (A) Part of a time series of the number of water molecules on a lipid molecule (blue line); conversion of this data into “on” or “off” states (yellow line), depending on whether the number of water molecules is above or below the average (red dashed line). (B) Ensemble-averaged PSD of the time series of the two states. The solid lines are shown as reference for higher and lower frequencies. (C) Ensemble-averaged PSD of the time series of the two states for four different measurement times: 2.05, 8.19, 32.8, and 131 ns. There is no aging.

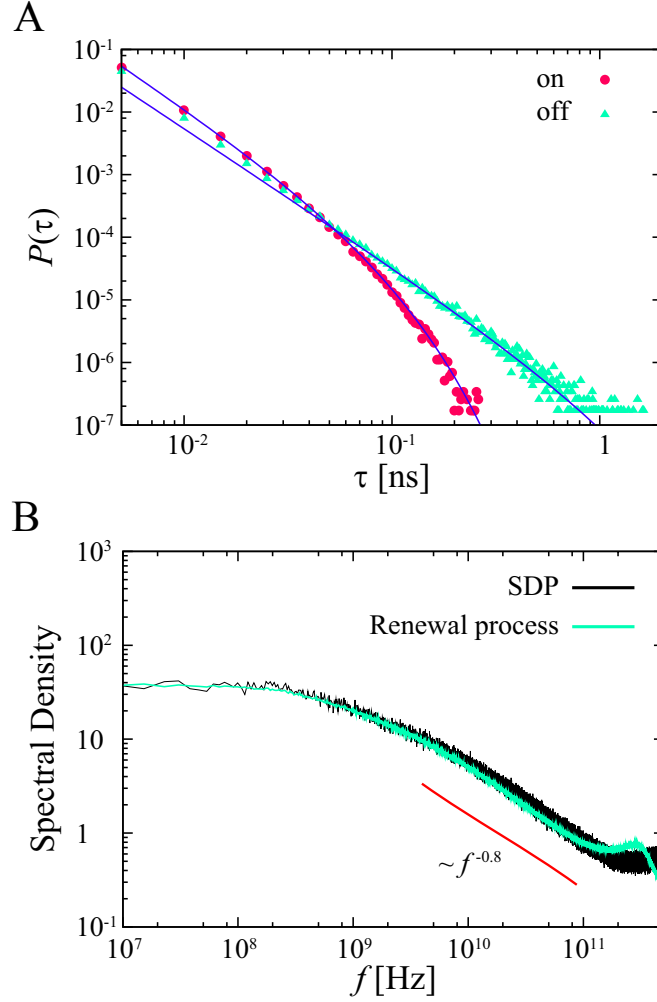


Fig. 5.4 Alternating renewal process. (A) PDFs of residence times of “on” and “off” states. Solid lines are fitted curves for power-law distributions with exponential cutoffs: $P(\tau) = A\tau^{-1-\alpha} \exp(-\tau/\tau_c)$ ($\alpha = 1.2$, on: $\tau_c = 59$ ps, off: $\tau_c = 1074$ ps). (B) Ensemble-averaged PSD of shuffled dichotomous processes (SDP) (black line) on the POPC membrane. Numerical simulation of alternating renewal process; residence times are given by power-law distribution with exponential cutoff, where $\alpha = 1.2$, on: $\tau_c = 60$ ps, off: $\tau_c = 1000$ ps (green line). The solid line is shown for reference.

in the PSD is given by the power-law exponent in the residence time distribution, i.e. $\beta = 2 - \alpha$ as $\alpha < 2$ [198]. The power-law exponent β observed here in the PSD is consistent with this relationship.

To clarify the correlation between residence times, we consider three types of time series of residence times: $\{\tau_1^{\text{on}}, \dots, \tau_n^{\text{on}}\}$, $\{\tau_1^{\text{off}}, \dots, \tau_n^{\text{off}}\}$, and $\{\tau_1^{\text{on}}, \tau_1^{\text{off}}, \dots, \tau_n^{\text{on}}, \tau_n^{\text{off}}\}$. Figure 5.5A shows the conditional averages of τ_{i+1} , denoted by $\langle \tau_{i+1} \rangle_{\tau_i}$, when the previous residence time is in $[\tilde{\tau}_{lk}, \tilde{\tau}_{l(k+1)})$ for some $k \in \{0\} \cup \mathbb{N}$, where we set $l = 10^3$

and $\tilde{\tau}_i$ is rearranged in ascending order ($\tilde{\tau}_0 < \tilde{\tau}_1 < \dots < \tilde{\tau}_i < \tilde{\tau}_{i+1} < \dots$) [214]. There are positive correlations of residence times between the previous “on” state and the current “on” state or the previous “off” state and the current “off” state, and negative correlations of residence times between an “on” state residence time and the next “off” state time or an “off” state residence time and the next “on” state time. This means that each state is stable, i.e. the hydration layer is stabilized. Furthermore, we show the degree of non-Markovianity, $G(\Delta, T)$, in Fig. 5.5B [192] (the details are shown in Methods). We used 12800 data at each time step to calculate the transition probabilities, and $G(\Delta, T)$ were calculated for $T = 600$ ps. Maximal values for dichotomous process (DP) and shuffled dichotomous process (SDP) are $G_{\text{DP}}(21, 600) = 0.067$ and $G_{\text{SDP}}(6, 600) = 0.015$, respectively. The value for computer-generated Markovian dichotomous processes is $G = 0.004$. The dichotomous process generated by the hydration dynamics shows strong non-Markovianity, while the shuffled dichotomous process also shows non-Markovianity before 400 ps. Moreover, the ensemble-averaged PSDs of the three types of time series of residence times exhibit $1/f$ noise [see Fig. 5.5C]. This result means that the residence times have a long-term correlation. These results imply that the high non-Markovianity of the dichotomous processes comes from not only a power-law residence time distribution but also a long-term memory in residence times. These results suggest that the origin of the $1/f$ noise is a combination of a power-law residence time distribution and a long-term correlation between residence times. These correlations between residence times are also observed in quantum dot blinking experiments [215, 216].

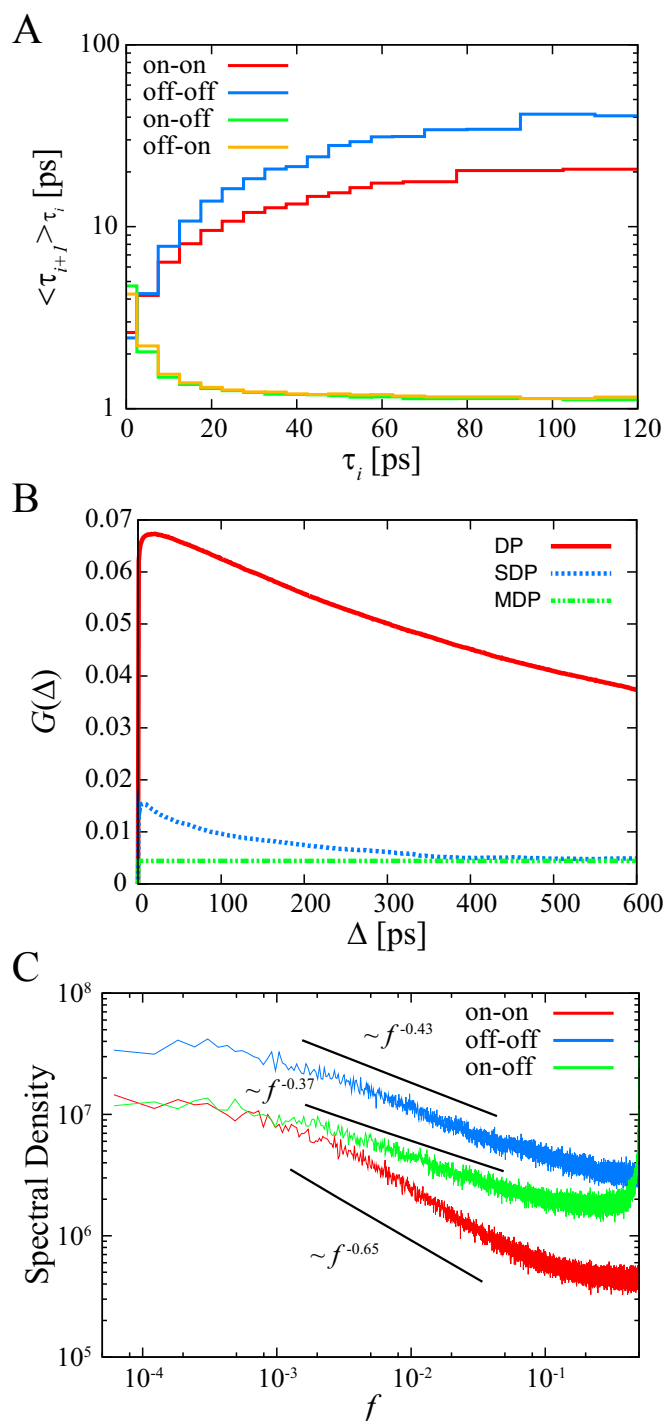


Fig. 5.5 Correlation between residence times on the POPC membrane. (A) Conditional averages of the residence times. Different color lines distinguish the pairs used for the analysis. (B) Degree of non-Markovianity for dichotomous processes (DP), shuffled dichotomous processes (SDP), and Markovian dichotomous processes (MDP). (C) Ensemble-averaged PSD of residence times. The solid lines are shown for reference.

Although we used conventional hydrogen bond distance 0.35 nm to define the surface water molecules, it was shown that there is no preferential mutual orientation between two water molecules if the distance is more than 0.3 nm [217, 218]. We confirmed $1/f$ noise with different definition of hydrogen bond distance 0.3 nm [see Fig. 5.6]. The value of the power law exponents of PSD become $\beta = -1.2$ at high frequencies. And transition frequency of the PSD shift to larger frequency because the cutoff of the distribution of the residence time in dichotomous process becomes short.

Moreover, surface water structures and diffusivities of lipid molecules are known to be affected by negatively charged lipids and ions [38, 219]. To clarify the universality of observed $1/f$ noise, we performed additional MD simulations of (i) pure POPE membrane [see Fig. 5.7-5.9], (ii) negatively charged membrane of POPC/POPS (4:1) lipids with 150 mM NaCl ions [see Fig. 5.10-5.11], and (iii) different force field, thermostat, and barostat [see Fig. 5.12]. Power-law exponent β of PSDs and cutoff time τ in the power-law residence time are slightly different. However, there are no significant qualitative differences, that is, the power law exponent β and the origin of the $1/f$ noise [see Fig. 5.6-5.12].

In summary, we have found that fluctuations of number of water molecules on the lipid molecules exhibit $1/f^\beta$ noise with $\beta > 1$ and that the power spectrum does not break ergodicity. Moreover, we have provided an evidence that the $1/f$ noise and ergodic behavior are caused by non-Markov power-law intermittency with exponential cutoff. What is a biological significance of $1/f$ noise in hydration dynamics on lipid membrane surfaces? The roles played by the water molecules near the membrane depend upon their structure and dynamics. There are positive correlations of residence times between the same states, and negative correlations of residence times between the different states. This means that each state is stable, i.e. the hydration layer is stabilized. The $1/f$ noise attributed to a correlated renewal process can contribute to the stability of the hydration layer, which is important for membrane stability and physiological processes. Moreover, these results are relevant to a broad range of systems displaying $1/f$ fluctuations.

Because dynamics of lipid molecules and membrane structures affect the hydration dynamics of water molecules, the complexity of lipid membrane surfaces, diffusivity, and fluctuations of lipid height will contribute to the $1/f$ noise. Here we confirmed that temporal fluctuations of the height of lipid molecules also show

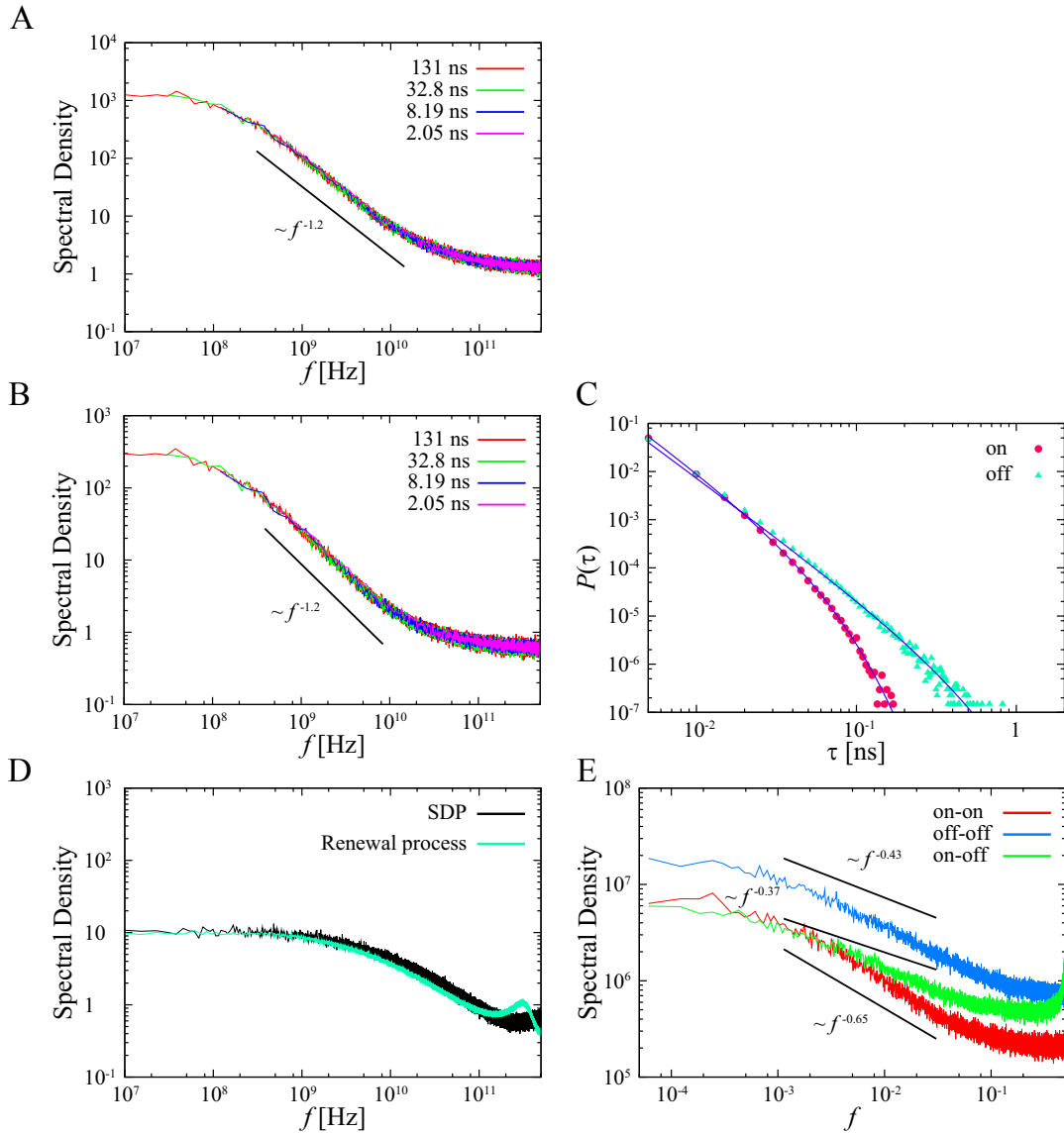


Fig. 5.6 $1/f$ noise in the hydration dynamics on the POPC membrane with using different hydrogen bond distance 0.3 nm. (A) Ensemble-averaged PSD of number of water molecules on POPC lipid head group. We use 128 time series to obtain the ensemble-averaged PSD. The different colored lines represent different measurement times. The solid line is shown as a reference. (B) Ensemble-averaged PSD of the time series of the two states. The dichotomous process was generated in the same way as the POPC membrane in the main text. (C) PDFs of residence times of “on” and “off” states on POPC. Solid lines are fitted curves for power-law distributions with exponential cutoffs: $P(\tau) = A\tau^{-1-\alpha} \exp(-\tau/\tau_c)$ ($\alpha = 1.4$, on: $\tau_c = 35$ ps, off: $\alpha = 1.45$, $\tau_c = 350$ ps). (D) Ensemble-averaged PSD of shuffled dichotomous processes (SDP) (black line). Numerical simulation of alternating renewal process; residence times are given by power-law distribution with exponential cutoff, where on: $\alpha = 1.4$, $\tau_c = 35$ ps, off: $\alpha = 1.45$, $\tau_c = 350$ ps (green line). (E) Ensemble-averaged PSD of residence times of two states.

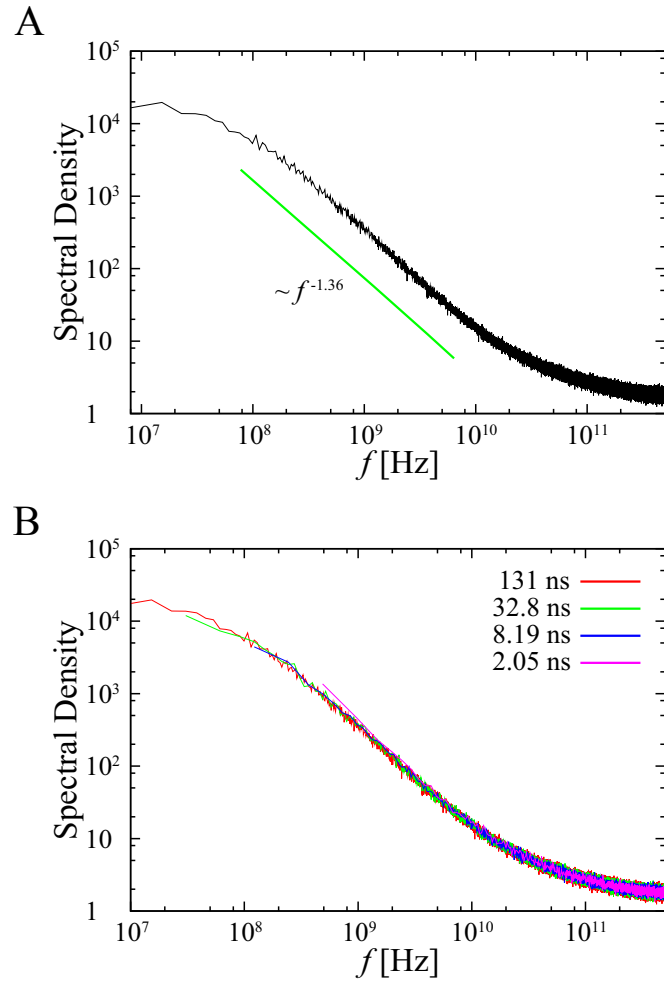


Fig. 5.7 $1/f$ noise in the hydration dynamics on the POPE membrane. (A) Ensemble-averaged PSD of number of water molecules on a lipid head group. We use 128 time series to obtain the ensemble-averaged PSD. The solid lines represent power-law behavior for reference. Total measurement time was 131 ns. (B) Ensemble-averaged PSD for four different measurement times: 2.05, 8.19, 32.8, and 131 ns. There is no aging.

$1/f$ noise [see Fig. 5.13]. The transition frequency in the PSD from $1/f$ noise to a plateau is almost the same as that of fluctuation of number of water molecules around the lipid molecule [see Fig. 5.1B and 5.13]. It has been shown that lipid bilayers exhibit transient subdiffusion originated from fractional Brownian motion (FBM) (viscoelasticity) [13, 14, 179] and shows dynamic heterogeneity [13]. Moreover, water molecules on the lipid membrane surfaces exhibit subdiffusion, which originates from a combination of long-term correlated noise (FBM) and divergent mean trapping time (CTRW) [see Chapter 4]. A power-law waiting time distribution, arising from random binding of water molecules with the lipid molecules or 1D

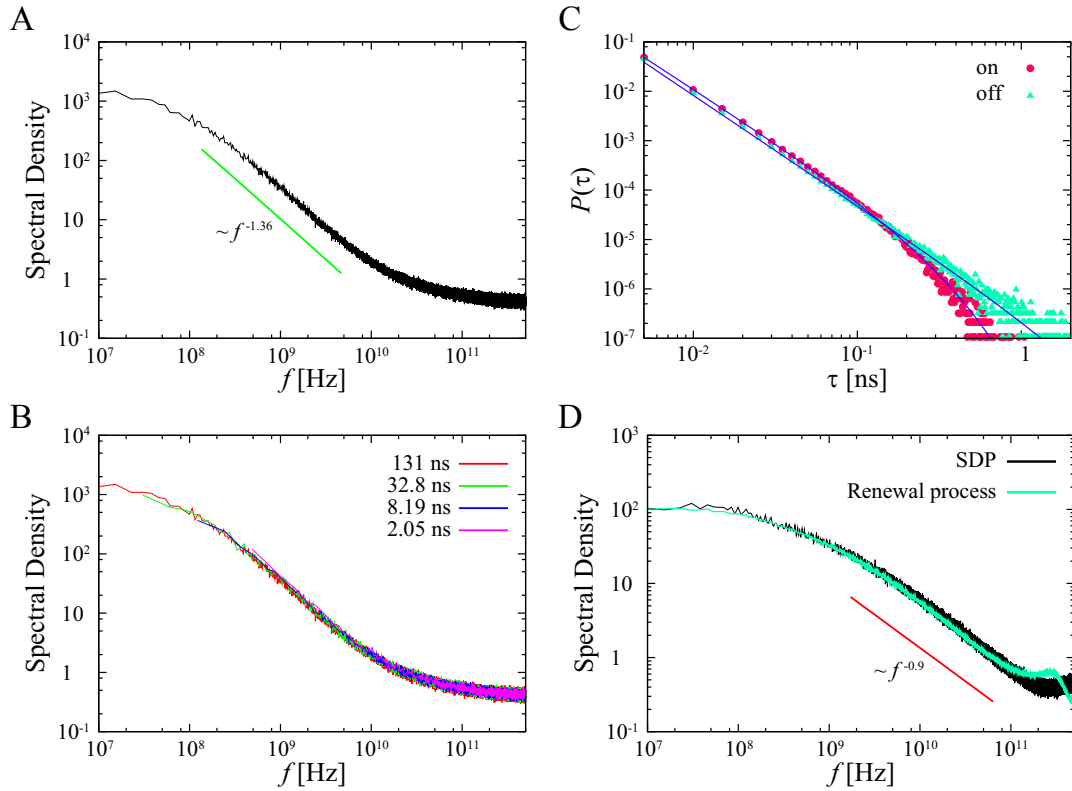


Fig. 5.8 $1/f$ noise in the dichotomous process on the POPE membrane. The dichotomous process was generated in the same way as the POPC membrane in the main text. (A) Ensemble-averaged PSD of the time series of the two states. We use 128 time series to obtain the ensemble-averaged PSD. The solid lines are shown as reference for higher and lower frequencies. (B) Ensemble-averaged PSD of the time series of the two states for four different measurement times: 2.05, 8.19, 32.8, and 131 ns. There is no aging. (C) PDFs of residence times of “on” and “off” states. Solid lines are fitted curves for power-law distributions with exponential cutoffs: $P(\tau) = A\tau^{-1-\alpha} \exp(-\tau/\tau_c)$ (on: $\alpha = 1.1$, $\tau_c = 240$ ps, off: $\alpha = 1.2$, $\tau_c = 3000$ ps). (D) Ensemble-averaged PSD of shuffled dichotomous processes (SDP) (black line). Numerical simulation of alternating renewal process; residence times are given by power-law distribution with exponential cutoff, where on: $\alpha = 1.1$, $\tau_c = 240$ ps, off: $\alpha = 1.2$, $\tau_c = 3000$ ps (green line). The solid line is shown for reference.

comb-like structure of lipid membrane surfaces, contributes to CTRW. Viscoelasticity of lipid bilayers contributes to the FBM of the water molecules. Furthermore, the hydrogen-bond exchange dynamics shows long range correlations between multiple water molecules [217, 218]. These effects will contribute to the origin of the observed $1/f$ noise.

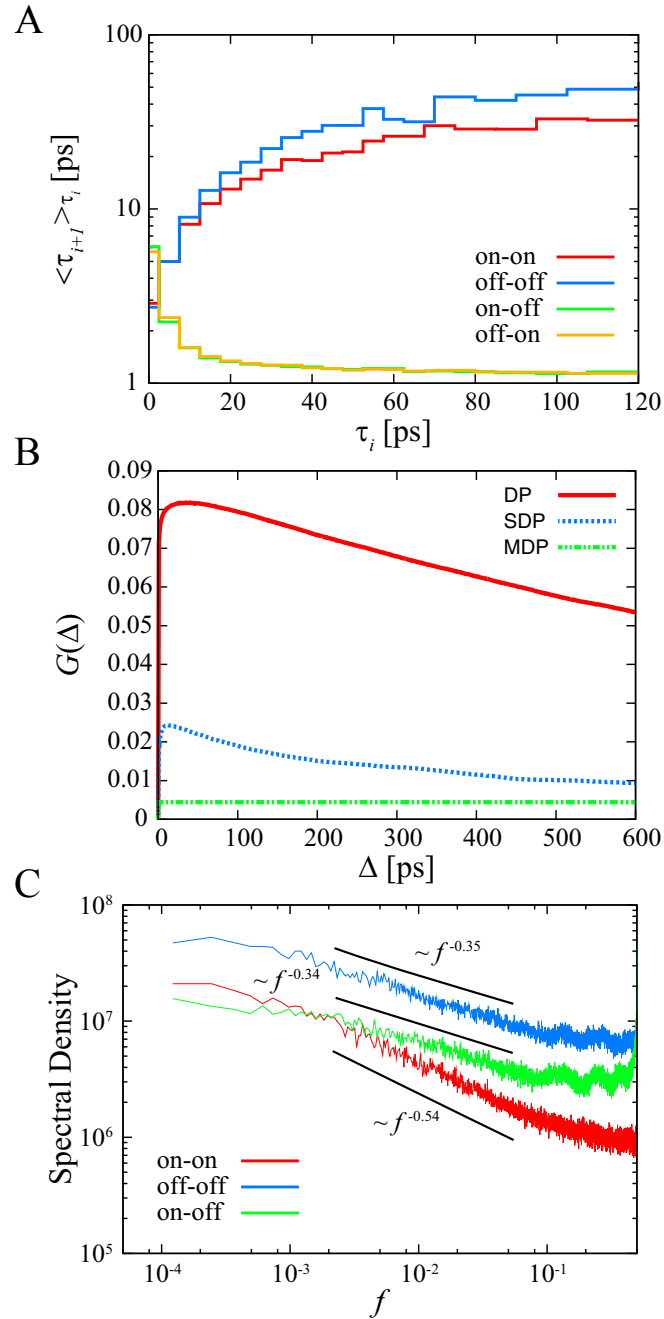


Fig. 5.9 Correlation of residence times on the POPE membrane. (A) Conditional averages of the residence times. Different color lines distinguish the pairs used for the analysis. (B) Degree of non-Markovianity for dichotomous processes (DP), shuffled dichotomous processes (SDP), and Markovian dichotomous processes (MDP). (C) Ensemble-averaged PSD of residence times. The solid lines are shown for reference.

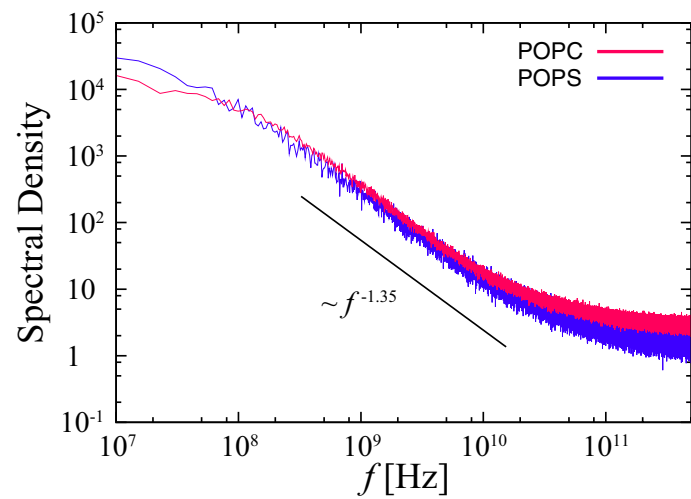


Fig. 5.10 $1/f$ noise in the hydration dynamics on the POPC/POPS membrane. Ensemble-averaged PSD of number of water molecules on a lipid head groups. We use 100 and 28 time series to obtain the ensemble-averaged PSDs on POPC (red) and POPS (blue) lipids, respectively. The solid lines represent power-law behavior for reference. Total measurement time was 131 ns. We confirmed that there is no aging.

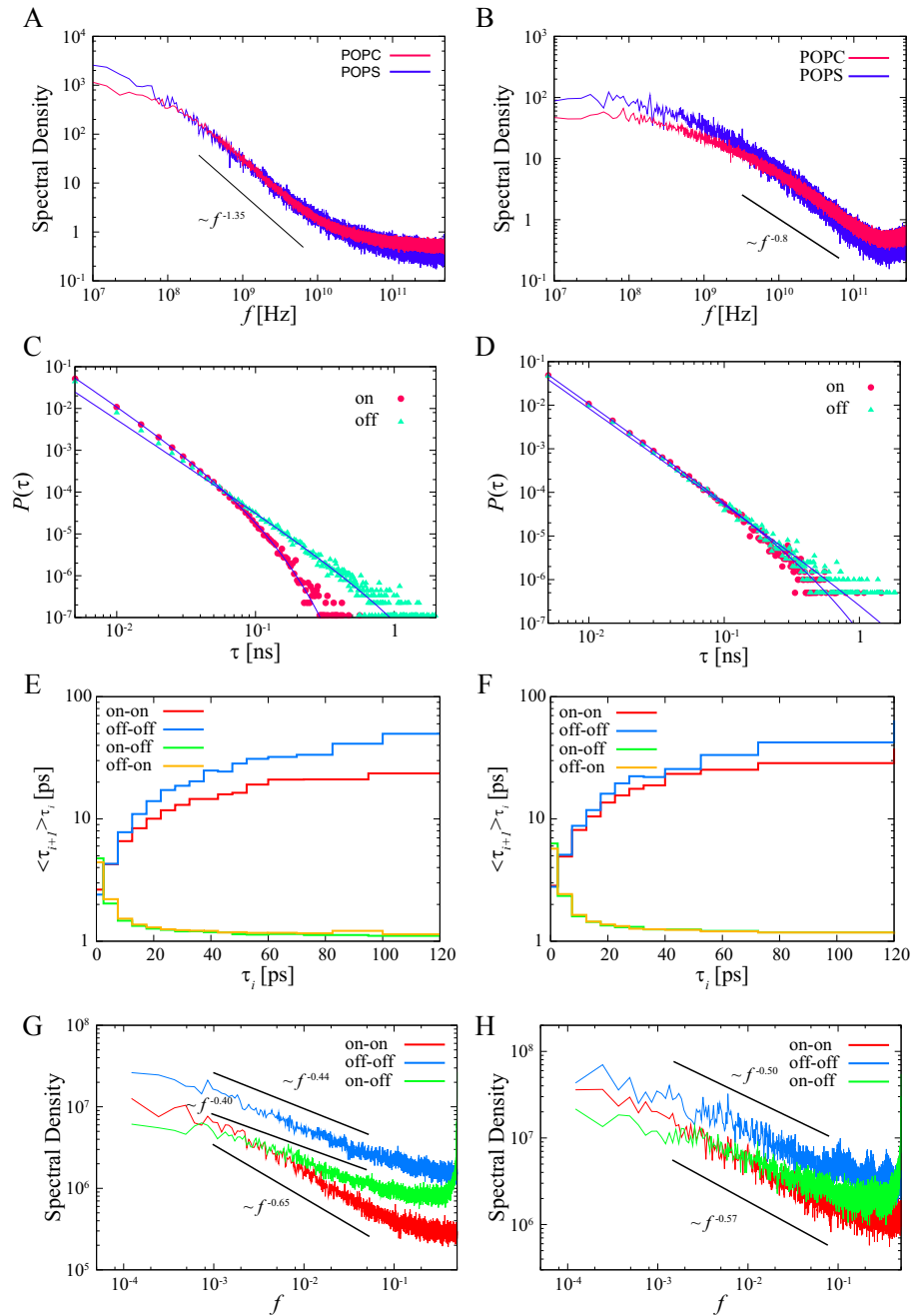


Fig. 5.11 $1/f$ noise in the dichotomous process on the POPC/POPS membrane. (A) Ensemble-averaged PSD of dichotomous processes. We use 100 and 28 time series to obtain the ensemble-averaged PSD on POPC and POPS lipids, respectively. The solid lines are shown as reference for higher and lower frequencies. We confirmed that there is no aging (results are not shown). (B) Ensemble-averaged PSD of shuffled dichotomous processes. (C) PDFs of residence times of “on” and “off” states on POPC. Solid lines are fitted curves for power-law distributions with exponential cutoffs: $P(\tau) = A\tau^{-1-\alpha} \exp(-\tau/\tau_c)$ ($\alpha = 1.2$, on: $\tau_c = 68$ ps, off: $\tau_c = 1000$ ps). (D) PDFs of residence times of “on” and “off” states on POPS. Solid lines are fitted curves for power-law distributions with exponential cutoffs: $P(\tau) = A\tau^{-1-\alpha} \exp(-\tau/\tau_c)$ ($\alpha = 1.2$, on: $\tau_c = 513$ ps, off: $\tau_c = 3420$ ps). (E) Conditional averages of the residence times on POPC and (F) POPS lipids. (G) Ensemble-averaged PSD of residence times on POPC and (H) POPS lipids. The solid lines are shown for reference.

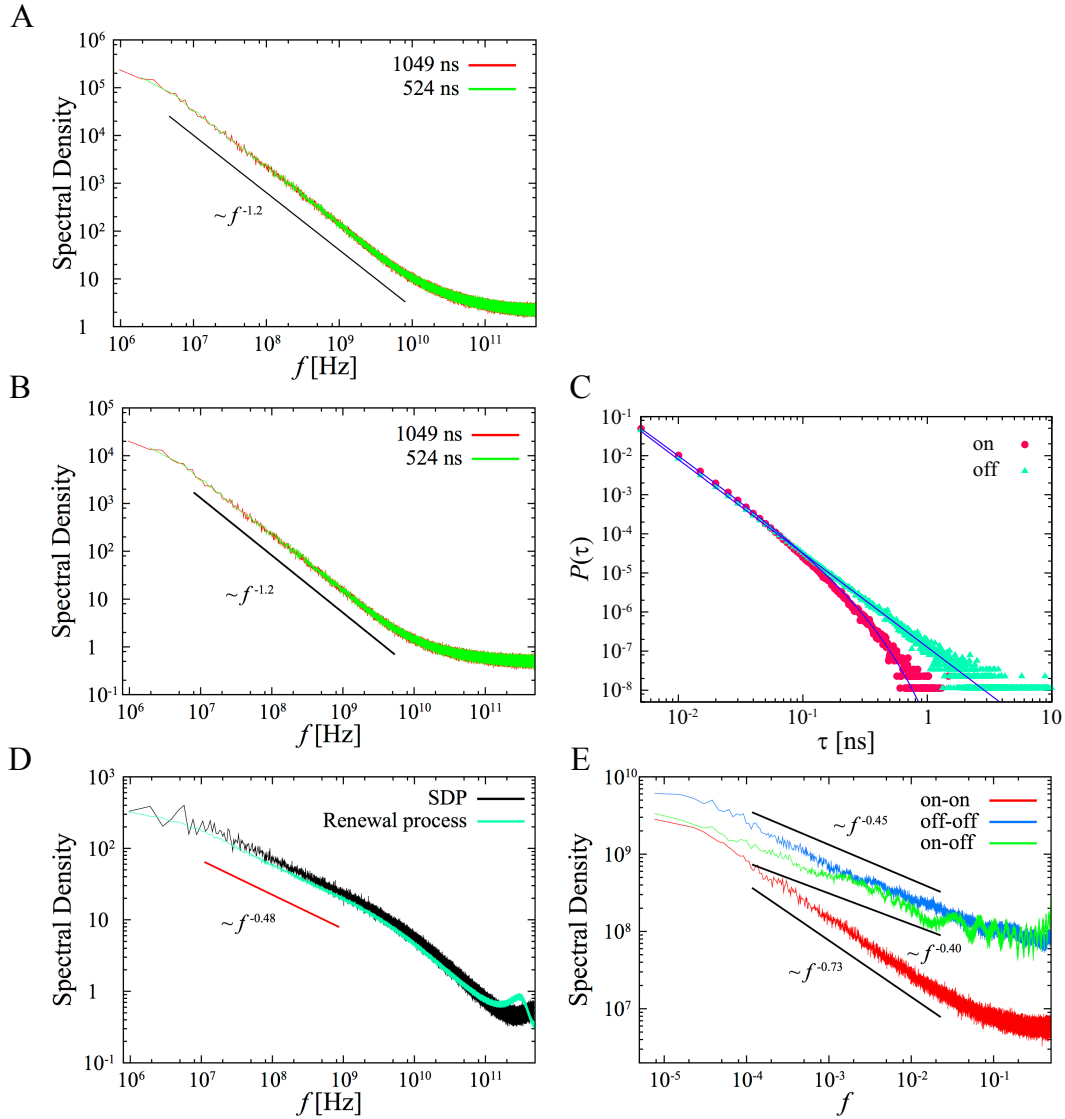


Fig. 5.12 Universality of the hydration dynamics with different force field, thermostat, and barostat. $1/f$ noise in the hydration dynamics on the POPC membrane with using GROMOS force field, SPC water model, Parrinello-Rahman barostat and velocity rescaling method for temperature controlling. (A) Ensemble-averaged PSD of number of water molecules on POPC lipid head group. We use 128 time series to obtain the ensemble-averaged PSD. The different colored lines represent different measurement times. The solid line is shown as a reference. (B) Ensemble-averaged PSD of the time series of the two states. The dichotomous process was generated in the same way as the POPC membrane in the main text. (C) PDFs of residence times of “on” and “off” states on POPC. Solid lines are fitted curves for power-law distributions with exponential cutoffs: $P(\tau) = A\tau^{-1-\alpha} \exp(-\tau/\tau_c)$ ($\alpha = 1.3$, on: $\tau_c = 196$ ps, off: $\alpha = 1.4$, $\tau_c = 100000$ ps). (D) Ensemble-averaged PSD of shuffled dichotomous processes (SDP) (black line). Numerical simulation of alternating renewal process; residence times are given by power-law distribution with exponential cutoff, where on: $\alpha = 1.3$, $\tau_c = 200$ ps, off: $\alpha = 1.4$, $\tau_c = 100000$ ps (green line). (E) Ensemble-averaged PSD of residence times of two states.

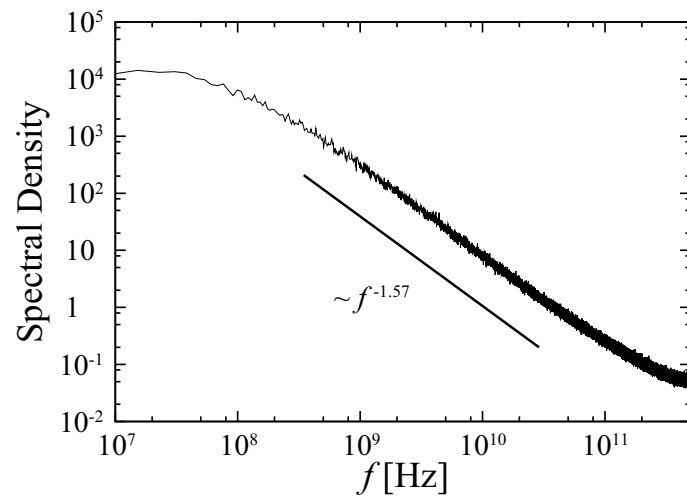


Fig. 5.13 Ensemble-averaged PSD of temporal fluctuations of perpendicular position of lipid molecules in the POPC membrane. The position of a lipid molecule is defined by the perpendicular distance between center of mass of the membrane and a phosphorus atom in the phosphate group of the lipid molecule. We use 128 time series (128 lipid molecules) to obtain the ensemble-averaged PSD. The PSD exhibits $1/f$ noise.

Chapter 6

$1/f$ fluctuations of amino acids regulate water permeation in AQP1

6.1 Introduction

As water molecules transit through AQPs, they are affected by neighboring water molecules and by AQP amino acids. Water-amino acid interactions occur chiefly in two characteristic domains, the NPA motif and the ar/R region [91]. Recently, Eriksson *et al.* reported that the water-water interactions within the yeast AQP are broken at the ar/R region, which prevents proton permeation [110]. Therefore, the ar/R region plays an important role in water permeation. However, the roles of fluctuations of the amino acids in these interactions are unclear. The relationship between conformational fluctuations of amino acids and water dynamics within AQPs may be of high biological importance.

During transit through the AQP pore, water molecules rotate as they encounter regions that heavily polarize their dipoles. In carbon nanotubes (CNTs), water molecules diffuse single file by a continuous-time random walk process with exponential waiting time distribution [220]. On the other hand, the statistical properties of first-passage water transport times in OmpF membrane protein channels are known to differ from those in homogeneous pores such as CNTs [129]. Therefore, little is known about AQP water dynamics because the channel steric conformations of AQPs are much more complicated than those in CNTs.

Here, we perform MD simulations of the AQP1 embedded in a POPE bilayer. The amino acids in AQP1 are found to undergo $1/f$ fluctuations. Moreover, the occurrence of water molecules crossing the ar/R region of AQP1 is a non-Poisson process. Analyzing water permeation through the channel is modeled by Langevin

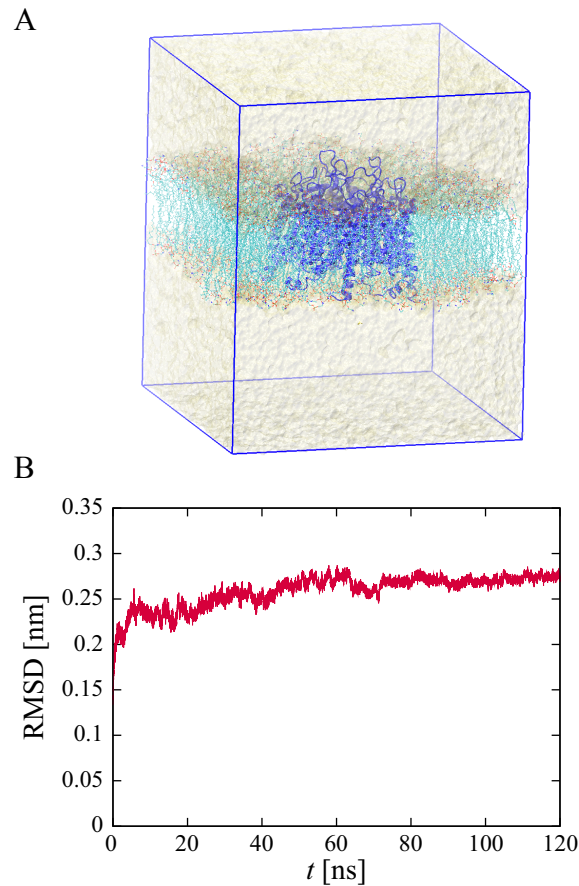


Fig. 6.1 (A) The system used for MD simulations of AQP1 in a POPE lipid bilayer. A single tetramer of AQP1 is embedded in the POPE lipid bilayer. The AQP1 is shown in cartoon (blue). Lipids are shown in green with their oxygen atoms in red. Explicit water molecules correspond to the upper and lower transparent coatings. The blue line of the box is a periodic boundary. (B) Root mean-square deviation (RMSD) of the AQP1. The RMSD fluctuates around a constant value after 70 ns, which means that the structure of the AQP1 is in an equilibrium.

stochastic simulations, we suggest that the $1/f$ fluctuations of amino acids may be implicated in water permeation control in AQPs.

6.2 Methods

6.2.1 Molecular dynamics simulations

To elucidate the water transport properties and fluctuations of amino acids in AQP1, we performed MD simulations of AQP1 (based on the X-ray crystallographic structure [83]) embedded in a POPE bilayer. The initial membrane system contained a homotetrameric assembly of free AQP1, 526 POPE molecules, and 74,738 TIP3P

water molecules [see Fig. 6.1A]. Before MD simulation, we minimized the energy of the system by the steepest descent method followed by the conjugate gradient method. A 120 ns MD simulation of the system was performed with a constant number of atoms at a pressure of 0.1 MPa and a temperature of 310 K. The MD simulation was carried out using Berendsen's algorithm with a coupling time of 0.2 ps. The time step was set at 1 fs. The lengths of hydrogen bonds were constrained to equilibrium lengths using the SHAKE method. Parm99 and gaff parameters were used for the protein and POPE lipids, respectively. This parameter for POPE has been used in previous studies of membranes or membrane proteins [5,13,62,96]. The particle mesh Ewald method was used, with a specified direct space cutoff distance of 1.0 nm. A three-dimensional periodic boundary condition was imposed on all systems. Because the system reached equilibrium at 70 ns, the trajectories of the final 50 ns were used in the analysis [see Fig. 6.1B].

Moreover, to investigate the effect of the $1/f$ fluctuations of amino acids on water permeation, we performed three MD simulations in which all amino acid residues of AQP1 were restrained within a harmonic potential in Cartesian space. The force constant was 10 kcal/mol \AA^2 . The initial structures in the restrained MD simulations were assumed from equilibrium structures of MD simulations at 80, 100, and 120 ns. Three independent restrained MD simulations were performed over 20 ns. All MD simulations were performed using AMBER10 software [140].

6.2.2 Detrended fluctuation analysis

Detrended fluctuation analysis (DFA) [221] is a method for detecting a long-range correlations embedded in a time series. First, we construct an integrated time series $y_i = \sum_{j=1}^i r_j$ and divide the series into bins of size n . The fluctuation function $F(n)$ is the root mean-square of the deviations from a local trend (determined by least-squares fitting), defined by

$$F(n) \equiv \sqrt{\frac{1}{mn} \sum_{j=1}^m \sum_{i=(j-1)n+1}^{jn} \{y_i - (a_j x_i + b_j)\}^2}, \quad (6.1)$$

where m represents the number of bins of size n . The fluctuation function exhibit a scaling $F(n) \simeq n^\beta$, and the scaling exponent β gives an information about the correlation properties of the time series. The cases $\beta < 0.5$ and $\beta > 0.5$ correspond to anti-correlated and correlated noise, respectively. Especially, certain exponents

β correspond to characteristic noises; $\beta \simeq 0.5$: white noise and $\beta \simeq 1$: $1/f$ noise. The exponent β and the exponent α of the power spectral density $S(f) \simeq f^{-\alpha}$ of the original time series are related by $\alpha = 2\beta - 1$.

6.3 Results and Discussion

6.3.1 Fluctuations of amino acids in AQP1

Channel steric conformation and solute binding sites in AQP1 facilitate the rapid and highly selective permeation of water molecules. As mentioned above, AQP1 contains two characteristic domains. One is the Asn-Pro-Ala (NPA) motif located at the two short helices in the center of the membrane, which contains amino acids N78 and N194 [83] [see Fig. 6.2A]. The NPA motif allows water molecules to form hydrogen bonds with two Asn residues, thereby reversing the orientation of the water molecules. The other domain is an ar/R region constituting the narrowest part of the pore, formed by Phe58, His182, Cys191, and Arg197 [93, 222] [see Fig. 6.2B]. The ar/R region performs a filtering role, blocking partially hydrated ions that are too large to pass through the narrow region [72, 96]. To evaluate the conformational fluctuations in AQP1, we analyze the distances between the centers of mass coordinates of amino acids in the ar/R region (H182 and R197) and in the NPA motif (N78 and N194) over a 50 ns simulation period [see Fig. 6.2C]. The distance fluctuations are characterized by the power spectral density of these distances [see Fig. 6.2D]. The amino acids in AQP1 show $1/f$ fluctuations. To improve the clarity of the results, we perform DFA [see Fig. 6.2E]. The $F(n)$ is linear about both H182-R197 and N78-N194, again suggesting that the distances between the amino acids undergo $1/f$ fluctuations. Figure 6.2F shows a PDF of the power law exponent α . The distances between amino acid pairs show $1/f^\alpha$ fluctuations in AQP1. The exponent α depends on the amino acid pairs.

These $1/f$ fluctuations of amino acids are intriguing. In biological systems, $1/f^\alpha$ noises have been reported for protein conformational dynamics [185, 186], DNA sequences [188], and ionic currents [190, 192, 193], implying that biological proteins generally undergo long-range correlated dynamics. Distance fluctuations between donors and acceptors have been modeled by the generalized Langevin equation with fractional Gaussian noise [186]. Thus, we expect that other transmembrane proteins will exhibit $1/f$ fluctuations. Our present finding has potentially important implications for biological functions.

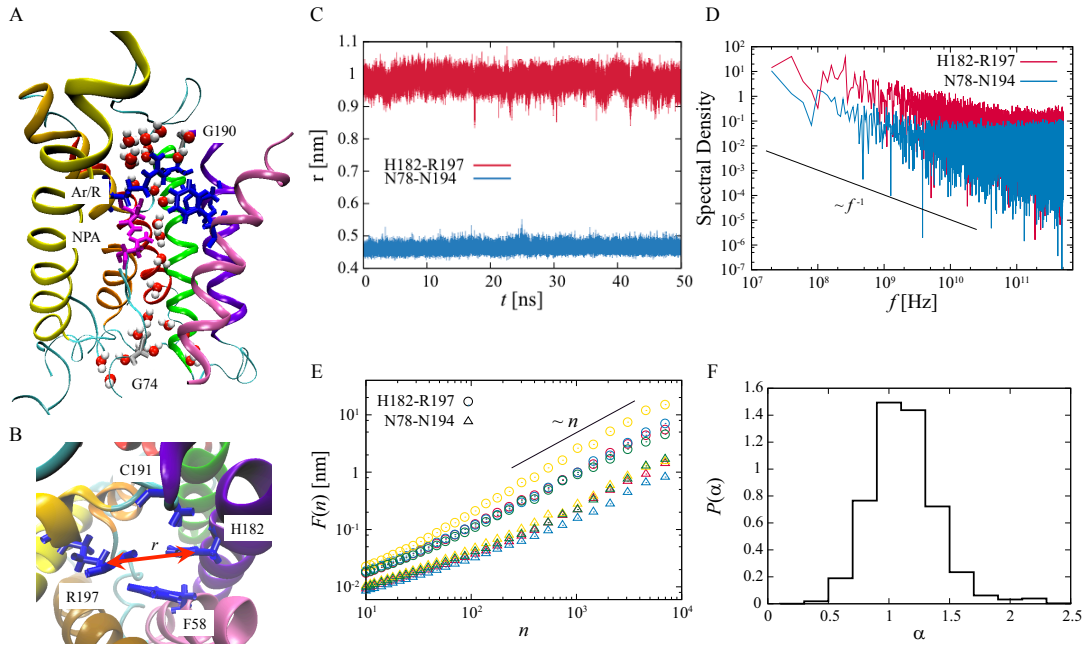


Fig. 6.2 Fluctuations of amino acids in AQP1. (A) Snapshot of AQP1 monomer channeling a single file of water molecules. (B) Snapshot of ar/R region in AQP1. Histidine and arginine contribute to the filter mechanism. The distance between H182 and R197 is analyzed. (C) Distances between amino acids in AQP1, as a function of time. Red and blue lines indicate H182-R197 and N78-N194 distances, respectively. (D) PSD of the distances between amino acids. The solid line has slope -1 . (E) DFA of distances between amino acids in AQP1. Different pores in the AQP1 tetramer are distinguished by colored symbols. Circles and triangles represent the H182-R197 and N78-N194 distances, respectively. The black line is shown for reference. (F) PDF of the exponent α of power spectral densities $S(f) \simeq f^{-\alpha}$ on amino acid distances. These are obtained from all amino acid pairs in a monomer.

6.3.2 Water dynamics within AQP1

To investigate the water dynamics in AQP1, we calculate the free energy difference $F_e(z)$ of water molecules in the AQP1 pore, given by $F_e(z) = -\ln \rho(z)$ [see Fig. 6.3A], where z and $\rho(z)$ are the coordinate and the PDF, respectively, of water molecules in the pore. We define units of energy by setting $k_B T = 1$. The PDFs are computed from all trajectories of water molecules in four different pores. There is a high energy barrier around the ar/R region ($z \cong 0.6 - 0.8$ nm). Water molecules are trapped in a free energy valley in AQP1. Trapped water molecules jump to neighboring sites at certain instances in time. Jumping events are evident in the trajectories of water molecules in the AQP1 [see Fig. 6.3B]. To investigate

the jumping event across the ar/R region, we define the z coordinate of this region as the center of mass of the H192 and R197 amino acids (the pink line in Fig. 6.3B). Because the ar/R region is the narrowest section of the pore, jumping events across the region are readily observed. We then calculate the PDFs of the interoccurrence times of the jumping events. To remove molecular vibrational effects from the PDF, an event is considered a jump only if its movement across the z coordinate of the ar/R region exceeds 0.1 nm. As shown in Fig. 6.3C, the PDFs follow non-exponential distributions, a non-Poisson process.

One important question remains unclear: what is the origin of the non-Poisson process? In other words, does the non-Poisson process come from effects by the complex configuration within the pore or $1/f$ fluctuation of amino acids? To address this question, we perform MD simulations in which the AQP1 structure is restrained using a harmonic potential. Three independent restrained MD simulations are performed over 20 ns. DFAs of the NPA motif (N78 and N194) and ar/R region (H182 and R197) are shown in Fig. 6.3A. The amino acid fluctuations are modified in the restrained MD simulations. Here, the line of slope 0.5 signifies white noise. Figure 6.3B shows $F_e(z)$ of water molecules in the restrained AQP1. The value of $F_e(z)$ depends on the first configuration used for the restrained MD simulations. The modified fluctuations from $1/f$ noise to white noise alter the water permeation dynamics within the AQP1. The jump events across the ar/R region are characterized by a Poisson process, where the interoccurrence times of the jumping events are distributed exponentially [see Fig. 6.3C]. This implies that water permeation is extensively affected by amino acid fluctuations. Because the water permeation depends largely on the pore size, the $1/f$ fluctuation of distances between amino acids within the AQP1 is important to regulate the water permeation. We note that the pore sizes in some restrained AQPs became too small to pass water molecules.

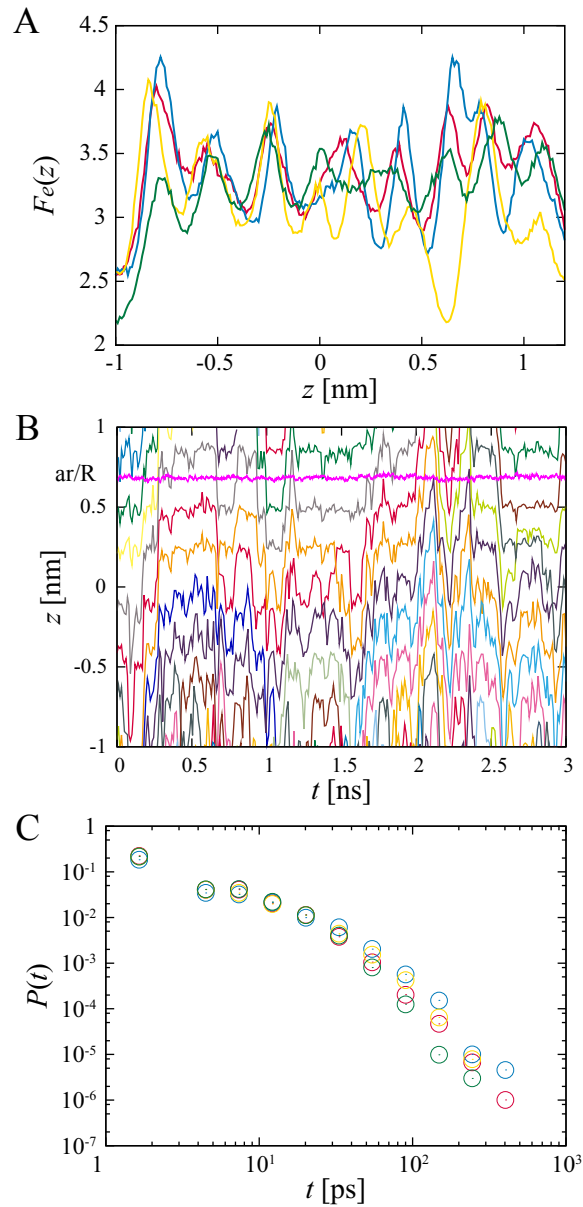


Fig. 6.3 Water permeation in AQP1. (A) Free energy variation of water molecules within AQP1. The NPA motif (center of N78 and N194) is located at $z = 0$. Colored lines represent the density of water molecules in different pores of the AQP1 tetramer. (B) Water translocation in AQP1 throughout the 3 ns time course of the MD simulation. The z coordinate of the NPA motif (located at $z = 0$) has been subtracted from all z coordinates. For enhanced clarity, results are averaged over 10 ps intervals. Individual water molecules are assigned different colors each time they enter or re-enter the channel. Pink line around $z = 0.7$ nm is the z coordinate of the ar/R region (center of H182 and R197). (C) PDFs of interoccurrence times of jump events of water molecules at the ar/R region. Different AQP1 pores are distinguished by colored symbols.

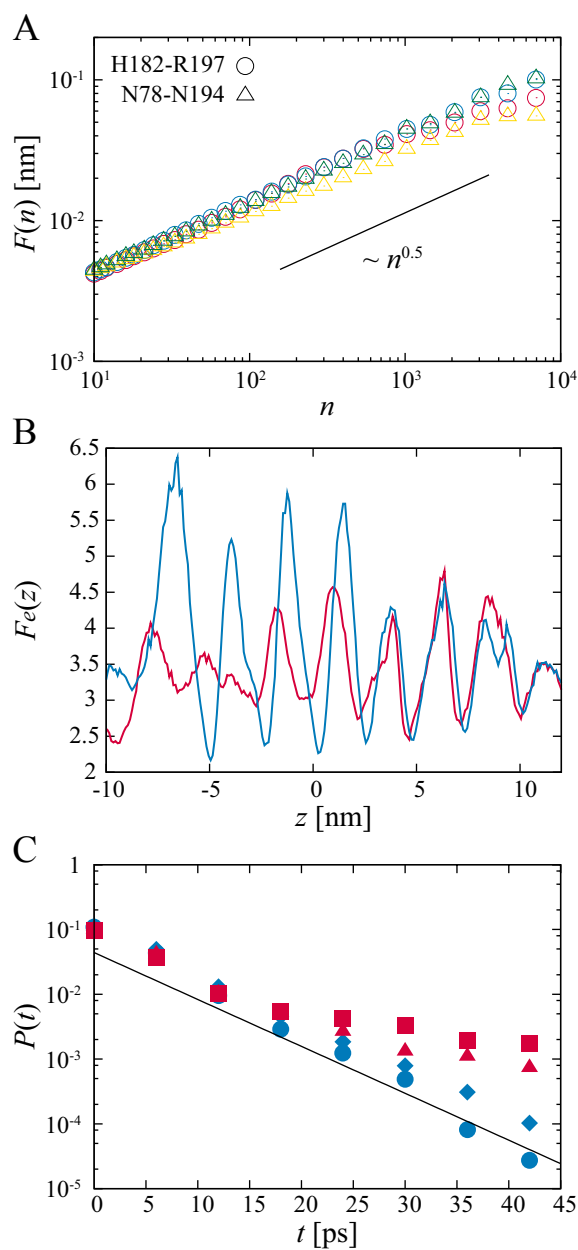


Fig. 6.4 Restrainted MD simulations of AQP1. (A) DFAs on distances of amino acids in AQP1. Colored symbols distinguish between different AQP1 pores. Circles and triangles represent H182-R197 and N78-N194 distances, respectively. The solid line represents $F(n) \sim n^{0.5}$. (B) Free energy variation of water molecules within restrained AQP1. The NPA motif is located at $z = 0$. Colored lines represent the density of water molecules in different pores. (C) PDFs of interoccurrence times of the jumping events of water molecules across the ar/R region. Red and blue symbols indicate the results of MD and restrained MD simulations, respectively. Different pores in the AQP1 tetramer are distinguished by different symbols. The solid line represents an exponential distribution.

6.3.3 Stochastic model of water permeation

The restrained MD simulations are somewhat artificial and difficult to obtain enough ensembles due to the dependence on the first configuration. To capture the essential feature of water permeation through AQPs, we propose a stochastic model that a particle is trapped in a potential and jump the potential height [see Fig. 6.5A]. As discussed in the previous subsection, events of water molecules crossing the ar/R region crucially depend on the pore size, which fluctuates with the $1/f$ distribution. The pore size corresponds to the height of the potential E , and the fluctuation of the amino acids represents the fluctuation of the potential height. We consider that the motion of water molecules is driven by white Gaussian noise. The water molecules are modeled as particles governed by a Langevin equation in a harmonic potential:

$$m \frac{d^2x(t)}{dt^2} = -m\gamma \frac{dx(t)}{dt} - kx(t) + R(t), \quad (6.2)$$

where m is the mass of water molecule, γ is a friction coefficient, and k is a spring constant. The random driving force $R(t)$ satisfies the fluctuation-dissipation relation, $\langle R(t)R(t') \rangle = 2m\gamma k_B T \delta(t-t')$, where k_B is the Boltzmann constant and T is a temperature. Parameter values used in simulations were $k = 5$ and $m = \gamma = 1$. Water permeation occurs when the particle exceeds a random fluctuating threshold. To mimic $1/f$ fluctuations, a fluctuating threshold $E(t)$,

$$E(t) = E_0 + E_N(t), \quad (6.3)$$

is generated by the following method [223], where E_0 specifies an average threshold:

$$E_N(t) = \sum_{i=0}^{N-1} \zeta_i(t) \quad (6.4)$$

$$\frac{d\zeta_i(t)}{dt} = -\nu_i \zeta_i(t) + \sqrt{2\nu_i \eta_i c_N} \xi_i(t) \quad (6.5)$$

where $\nu_i = \nu_0/b^i$ is the inverse autocorrelation time of the i th component and $\eta_i = [\eta_\alpha/\Gamma(1-\alpha)]C_\alpha(b)\nu_0^\alpha/b^{i\alpha}$ is its weight. The autocorrelation function of the noise is the sum of independent autocorrelation functions, $\langle \zeta_i(t)\zeta_j(0) \rangle = c_N \eta_i \delta_{ij} \exp(-\nu_i t)$,

$$\langle E_N(t)E_N(0) \rangle = \sum_{i=0}^{N-1} c_N \eta_i \exp(-\nu_i t),$$

which approximates $1/f^{1-\alpha}$ noise. Parameter values used in simulations were $E_0 = 1.35$, $\nu_0 = 50$, $b = 10$, $\eta_\alpha = 0.5$, $\alpha = 0.0001$, and $N = 16$. Power spectra of the $E_N(t)$ is shown in Fig. 6.5B. In the case of $N = 1$, the PDF of escape times follows an exponential distribution for different ν_1 [see Fig. 6.5C]. We note that the variances of $E_1(t)$ is adjusted to that of $N = 16$ by changing $\eta_1 c_1$. Figure 6.5D shows the PDF of escape times when the potential barrier fluctuates with $1/f$ noise ($N = 16$). In this case, the PDF follows a non-exponential distribution that strongly agrees with that of the interoccurrence times of the jumping events across the ar/R region. According to an increase of E_0 , PDF changes from non-exponential to exponential distribution (not shown). The non-exponential distribution originated from $1/f$ fluctuations is well consistent with that obtained by the MD simulation. Although this model lacks molecular details on water permeation in real AQPs, it avoids unwarranted assumptions about the detailed mechanisms and captures the essential features. This model implies that $1/f$ fluctuations of the potential barrier generate a non-Poisson feature of water permeation within the pore.

In summary, we have found that amino acids in AQP1 undergo $1/f$ fluctuations by performing MD simulations of membrane-embedded AQP1. Moreover, we have found that the interoccurrence times of water molecules crossing the ar/R region in AQP1 follow a non-exponential distribution. To investigate the significance of the $1/f$ fluctuations, we have performed restrained MD simulations of AQP1 and proposed a simple stochastic model of water permeation. The model predicts that water permeation depends on fluctuations of amino acids. These results suggest that $1/f$ fluctuations of amino acids regulate the water permeation in AQPs. Recently, design of using vibrating charge has been proposed for controlling the water transport through CNTs [224,225]. A continuous unidirectional water flow is driven by a vibration charge without osmotic pressure. Our finding would help in designing and developing nanoscale systems for desalination processes.

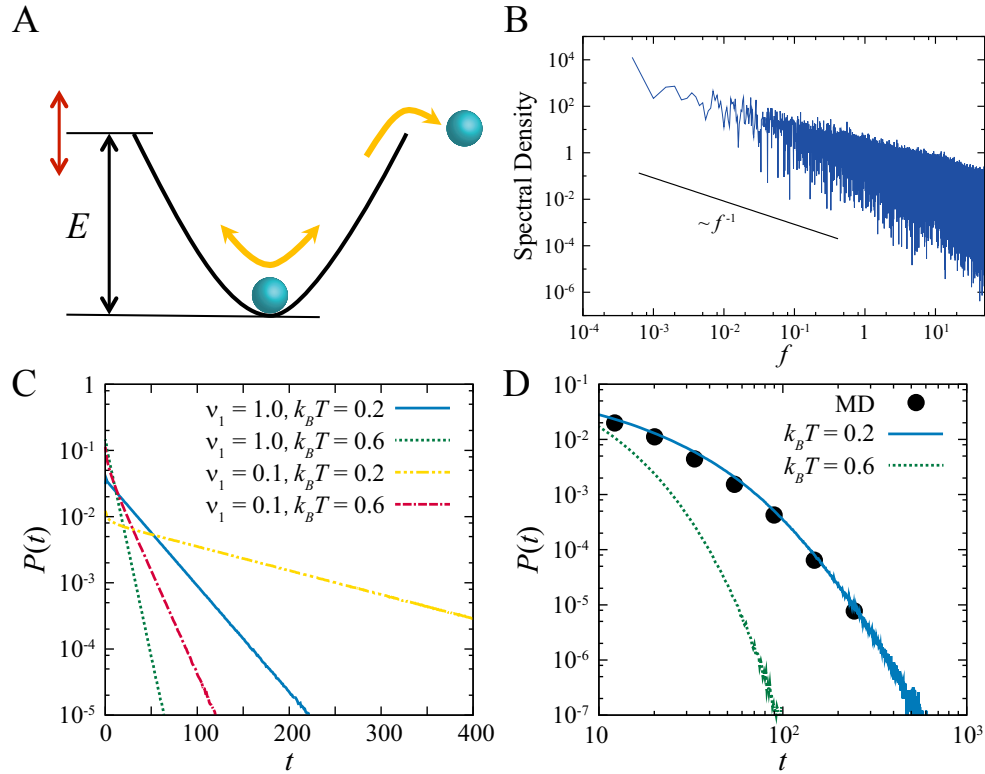


Fig. 6.5 Stochastic model of water permeation in AQP1. (A) Schematic of the model. A particle (blue circle) is trapped and fluctuates in a potential. The height of potential E fluctuates with $1/f$ noise (red arrow). At a certain moment, the particle escapes from the potential. (B) Power spectra of the $E_N(t)$. Parameters values used in the simulation were $\nu_0 = 50$, $b = 10$, $\alpha = 0.0001$, and $N = 16$. The solid line has slope -1. (C) PDF of escape times from the fluctuating-threshold potential follows Ornstein-Uhlenbeck noise ($N = 1$) or (D) $1/f$ noise ($N = 16$). The results for Ornstein-Uhlenbeck noise ($N = 1$) and $1/f$ noise ($N = 16$) are shown as single log and log-log plots, respectively. The lines are the results of Langevin simulations. The red circles are the MD simulation results.

Chapter 7

Conclusion

In summary, we have performed MD simulations to investigate the water dynamics around lipid membranes.

In chapter 3, we have shown that the temperature dependence of the water molecular motions on the lipid membrane surface is different from that in bulk. Decreasing temperature enhances the water retardation on the membrane surface, and the lateral motions of water molecules are correlated with the vertical motions. We have found that trapping times of water molecules onto membrane surfaces are distributed according to a power-law distribution and that the power-law exponents depend linearly on temperature, suggesting a random energy landscape picture.

In chapter 4, we have found that translational and rotational diffusion of water molecules on lipid membrane surfaces exhibit subdiffusion and aging. Moreover, we have provided evidence that both divergent mean trapping time (CTRW) and long-correlated noise (FBM) contribute to this subdiffusion.

In chapter 5, we have found that the fluctuation of the number of interfacial water molecules on the lipid membranes exhibits $1/f$ noise. Constructing a dichotomous process of the fluctuation, we have found that residence times in each state follow a power-law with exponential cutoff and that the process can be regarded as a correlated renewal process where interoccurrence times are correlated. The results imply that the origin of the $1/f$ noise in the hydration dynamics is a combination of a power-law distribution with cutoff of interoccurrence times of switching events and a long-term correlation between the interoccurrence times.

In chapter 6, we have analyzed water permeation and fluctuations of amino acids within AQP1. The amino acids exhibit $1/f$ fluctuations, indicating possession of long-term memory. Moreover, we have found that water molecules crossing the ar/R region obey a non-Poisson process. To investigate the effect of the $1/f$ fluctuations

on water permeation, we have performed restrained MD simulations of AQP1 and simple Langevin stochastic simulations. As a result, we have confirmed that the $1/f$ fluctuations of amino acids generate the non-Poisson feature of water permeation within AQP1.

What does the vast number of water molecules do in biological systems, though H_2O has innately simple configurations? Water in biology is not simply a solvent but plays more active and essential roles with biomolecules in complex and subtle ways. In this thesis, we have mainly focused on the movement of water molecules on the surface and through cell membranes. Water molecules cannot simply be regarded as “anomalous” but as a creator of a unique environment around the membranes. The observed anomalous diffusion and $1/f$ noise on the lipid membrane surfaces may contribute to the enhancement of membrane stability and provide a higher reaction efficiency. Moreover, the dynamics and structure of the interfacial water molecules are like a mirror reflecting the surrounding environment. The changes in the local diffusivities display the changes in the local structure and interaction with molecules.

Diffusion of biomolecules in cells are affected by the heterogeneous environment, which depends on the component, size, shape, and crowding of molecules. The cell membranes, also intracellular organelle membranes, are involved in a variety of biological process, where lipids, transmembrane proteins, peripheral membrane proteins move dynamically. On the surface of biomolecules, dynamics of water molecules is separated from bulk water. The diffusion of biomolecules change spatiotemporally and heterogeneously, and cannot be solely described by Brownian motion but with the addition of anomalous motion, where the latter is the more dominant mechanism. Are the anomalous motions merely a peculiarity of molecules, or can they be extended to biological benefits? Biomolecules are designed to target designated counterparts to play their physiological functions. The encounter and interaction of these biomolecules may be controlled by anomalous dynamics. Investigation of such intracellular transport events of biomolecules is indispensable to understand living organisms. Studying the mechanism of anomalous motion of biomolecules provides a deeper insight into biological systems.

In the future research, to understand more complex phenomena in living cells, larger scale simulations will be conducted based on the current atomistic results. Moreover, for the research, interdisciplinary approach and strong collaborations

between experimental, computational, and theoretical approaches, are required. This will accelerate mutual understanding, solve burning questions in biology, and open a new frontier in science.

Abbreviations and symbols

AQP	Aquaporin
ar/R	Aromatic/arginine
CTRW	Continuous time random walk
CNT	Carbon nanotube
DFA	Detrended fluctuation analysis
DMPC	Dimyristoyl-phosphatidylcholine
DPPC	Dihexadecanoyl-phosphatidylcholine
FBM	Fractional Brownian motion
MD	Molecular dynamics
MET	Mean exit time
MME	Mean maximal excursion
MSD	Mean squared displacement
NMR	Nuclear magnetic resonance
NPA	Asparagine-proline-alanine
ODNP	Overhauser dynamic nuclear polarization
PC	Phosphatidylcholine
PDF	Probability density function
PE	Phosphatidylethanolamine
PG	Phosphatidylglycerol
POPC	Palmitoyl-oleoyl-phosphatidylcholine
POPE	Palmitoyl-oleoyl-phosphatidylethanolamine
POPS	Palmitoyl-oleoyl-phosphatidylserine
PS	Phosphatidylserine
PSD	Power spectra density
RMSD	Root mean-square deviation
RSD	relative standard deviation
SAXS	Small angle X-ray scattering
SM	Sphingomyelin
TAMSD	Time-averaged mean square displacement
THz-TDS	Terahertz time-domain spectroscopy
VSFG	Vibrational sum frequency generation

Appendix

Publication list

Articles (related to this thesis)

- [1] Eiji Yamamoto, Takuma Akimoto, Masato Yasui, and Kenji Yasuoka, “Origin of $1/f$ noise in hydration dynamics on lipid membrane surfaces”, *Sci. Rep.* **5**, 8876 (2015).
- [2] Eiji Yamamoto, Takuma Akimoto, Masato Yasui, and Kenji Yasuoka, “Origin of subdiffusion of water molecules on cell membrane surfaces”, *Sci. Rep.* **4**, 4720 (2014).
- [3] Eiji Yamamoto, Takuma Akimoto, Yoshinori Hirano, Masato Yasui, and Kenji Yasuoka, “ $1/f$ fluctuations of amino acids regulate water transportation in AQP1”, *Phys. Rev. E* **89**, 022718 (2014).
- [4] Eiji Yamamoto, Takuma Akimoto, Yoshinori Hirano, Masato Yasui, and Kenji Yasuoka, “Power-law trapping of water molecules on the lipid-membrane surface induces water retardation”, *Phys. Rev. E* **87**, 052715 (2013).

Other articles

- [1] Eiji Yamamoto, Antreas C. Kalli, Takuma Akimoto, Kenji Yasuoka, and Mark S. P. Sansom, “Anomalous dynamics of a lipid recognition protein on a membrane surface”, *Sci. Rep.* **5**, 18245 (2015).
- [2] Winarto, Daisuke Takaiwa, Eiji Yamamoto, and Kenji Yasuoka, “Water-methanol separation with carbon nanotubes and electric fields”, *Nanoscale* **7**, 12659 (2015).
- [3] Winarto, Daisuke Takaiwa, Eiji Yamamoto, and Kenji Yasuoka, “Structures of water molecules in carbon nanotubes under electric fields”, *J. Chem. Phys.* **142**, 124701 (2015).
- [4] Katsufumi Tomobe, Eiji Yamamoto, Dusan Kojic, Masato Yasui, and Kenji Yasuoka, “Velocity auto-correlation function of ions and water molecules in different concentrations, anions and ion clusters”, *Mol. Sim.* **41**, 840 (2015).

-
- [5] Noriyoshi Arai, Takuma Akimoto, Eiji Yamamoto, Masato Yasui, and Kenji Yasuoka, “Direct observation of lipid flip-flop in membrane”, *J. Chem. Phys.* **140**, 064901 (2014).
- [6] Francesco Giangreco, Eiji Yamamoto, Yoshinori Hirano, Milan Hodoscek, Volker Knecht, Matteo di Giosia, Matteo Calvaresi, Francesco Zerbetto, Kenji Yasuoka, Tetsu Narumi, Masato Yasui, and Siegfried Höfner, “Common force field thermodynamics of cholesterol”, *Sci. World J.* **2013**, 207287 (2013).
- [7] Eiji Yamamoto, Takuma Akimoto, Hiroyuki Shimizu, Yoshinori Hirano, Masato Yasui, and Kenji Yasuoka, “Diffusive nature of xenon anesthetic changes properties of a lipid bilayer: Molecular dynamics simulations”, *J. Phys. Chem. B* **116**, 8989 (2012).
- [8] Siegfried Höfner, Eiji Yamamoto, Yoshinori Hirano, Francesco Zerbetto, Tetsu Narumi, Kenji Yasuoka, and Masato Yasui, “Structural features of aquaporin 4 supporting the formation of arrays and junctions in biomembranes”, *Biochim. Biophys. Acta* **1818**, 2234 (2012).
- [9] Takuma Akimoto, Eiji Yamamoto, Kenji Yasuoka, Yoshinori Hirano, and Masato Yasui, “Non-Gaussian fluctuations resulting from power-law trapping in a lipid bilayer”, *Phys. Rev. Lett.* **107**, 178103 (2011).

References

- [1] Kusumi, A., Suzuki, K. G. N., Kasai, R. S., Ritchie, K. & Fujiwara, T. K. Hierarchical mesoscale domain organization of the plasma membrane. *Trends Biochem. Sci.* **36**, 604 (2011).
- [2] van Meer, G., Voelker, D. R. & Feigenson, G. W. Membrane lipids: where they are and how they behave. *Nat. Rev. Mol. Cell Biol.* **9**, 112 (2008).
- [3] Koubi, L., Saiz, L., Tarek, M., Scharf, D. & Klein, M. L. Influence of anesthetic and nonimmobilizer molecules on the physical properties of a polyunsaturated lipid bilayers. *J. Phys. Chem. B* **107**, 14500 (2003).
- [4] Bemporad, D., Essex, J. W. & Luttmann, C. Permeation of small molecules through a lipid bilayer: A computer simulation study. *J. Phys. Chem. B* **108**, 4875 (2004).
- [5] Yamamoto, E. *et al.* Diffusive nature of xenon anesthetic changes properties of a lipid bilayer: Molecular dynamics simulations. *J. Phys. Chem. B* **116**, 8989 (2012).
- [6] Darvas, M., Hoang, P. N. M., Picaud, S., Sega, M. & Jedlovsky, P. Anesthetic molecules embedded in a lipid membrane: a computer simulation study. *Phys. Chem. Chem. Phys.* **14**, 12956 (2012).
- [7] Espinosa, G., López-Montero, I., Monroy, F. & Langevin, D. Shear rheology of lipid monolayers and insights on membrane fluidity. *Proc. Natl. Acad. Sci. USA* **108**, 6008 (2011).
- [8] Choi, S. Q., Steltenkamp, S., Zasadzinski, J. A. & Squires, T. M. Active microrheology and simultaneous visualization of sheared phospholipid monolayers. *Nat. Commun.* **2**, 312 (2011).
- [9] Sadoughi, A. H., Lopez, J. M. & Hirska, A. H. Transition from Newtonian to non-Newtonian surface shear viscosity of phospholipid monolayers. *Phys. Fluids* **25**, 032107 (2013).
- [10] Kim, K., Choi, S. Q., Zell, Z. A., Squires, T. M. & Zasadzinski, J. A. Effect

- of cholesterol nanodomains on monolayer morphology and dynamics. *Proc. Natl. Acad. Sci. USA* **110**, E3054 (2013).
- [11] Hermans, E. & Vermant, J. Interfacial shear rheology of DPPC under physiologically relevant conditions. *Soft Matter* **10**, 175 (2014).
- [12] Mason, T. G. & Weitz, D. A. Optical measurements of frequency-dependent linear viscoelastic moduli of complex fluids. *Phys. Rev. Lett.* **74**, 1250 (1995).
- [13] Akimoto, T., Yamamoto, E., Yasuoka, K., Hirano, Y. & Yasui, M. Non-gaussian fluctuations resulting from power-law trapping in a lipid bilayer. *Phys. Rev. Lett.* **107**, 178103 (2011).
- [14] Jeon, J.-H., Monne, H. M.-S., Javanainen, M. & Metzler, R. Anomalous diffusion of phospholipids and cholesterol in a lipid bilayer and its origins. *Phys. Rev. Lett.* **109**, 188103 (2012).
- [15] Lingwood, D. & Simons, K. Lipid rafts as a membrane-organizing principle. *Science* **327**, 46 (2010).
- [16] Contreras, F.-X. *et al.* Molecular recognition of a single sphingolipid species by a protein's transmembrane domains. *Nature* **481**, 525 (2012).
- [17] Barrera, N. P., Zhou, M. & Robinson, C. V. The role of lipids in defining membrane protein interactions: insights from mass spectrometry. *Trends Cell Biol.* **23**, 1 (2012).
- [18] Ball, P. Water as an active constituent in cell biology. *Chem. Rev.* **108**, 74 (2008).
- [19] Ball, P. More than a bystander. *Nature* **478**, 467 (2011).
- [20] Tsenkova, R. Introduction: Aquaphotomics: dynamic spectroscopy of aqueous and biological systems describes peculiarities of water. *J. Near Infrared Spectrosc.* **17**, 303 (2010).
- [21] Davidson, R. M., Lauritzen, A. & Seneff, S. Biological water dynamics and entropy: A biophysical origin of cancer and other diseases. *Entropy* **15**, 3822 (2013).
- [22] Milhaud, J. New insights into water–phospholipid model membrane interactions. *Biochim. Biophys. Acta* **1663**, 19 (2004).
- [23] Bagchi, B. Water dynamics in the hydration layer around proteins and micelles. *Chem. Rev.* **105**, 3197 (2005).
- [24] Disalvo, E. A. *et al.* Structural and functional properties of hydration and confined water in membrane interfaces. *Biochim. Biophys. Acta* **1778**, 2655

- (2008).
- [25] Pearson, R. H. & Pascher, I. The molecular structure of lecithin dihydrate. *Nature* **281**, 499 (1979).
- [26] Finer, E. G. & Darke, A. Phospholipid hydration studied by deuteron magnetic resonance spectroscopy. *Chem. Phys. lipids* **12**, 1 (1974).
- [27] Gawrisch, K. *et al.* Membrane dipole potentials, hydration forces, and the ordering of water at membrane surfaces. *Biophys. J.* **61**, 1213 (1992).
- [28] König, S. *et al.* Molecular dynamics of water in oriented DPPC multilayers studied by quasielastic neutron scattering and deuterium-nuclear magnetic resonance relaxation. *J. Chem. Phys.* **100**, 3307 (1994).
- [29] Swenson, J., Kargl, F., Berntsen, P. & Svanberg, C. Solvent and lipid dynamics of hydrated lipid bilayers by incoherent quasielastic neutron scattering. *J. Chem. Phys.* **129**, 045101 (2008).
- [30] Volkov, V. V. *et al.* Hydration and hydrogen bonding of carbonyls in dimyristoyl-phosphatidylcholine bilayer. *J. Am. Chem. Soc.* **128**, 9466 (2006).
- [31] Volkov, V. V., Palmer, D. J. & Righini, R. Heterogeneity of water at the phospholipid membrane interface. *J. Phys. Chem. B* **111**, 1377 (2007).
- [32] Binder, H. Water near lipid membranes as seen by infrared spectroscopy. *Euro. Biophys. J.* **36**, 265 (2007).
- [33] Tielrooij, K. J., Paparo, D., Piatkowski, L., Bakker, H. J. & Bonn, M. Dielectric relaxation dynamics of water in model membranes probed by terahertz spectroscopy. *Biophys. J.* **97**, 2484 (2009).
- [34] Hishida, M. & Tanaka, K. Long-range hydration effect of lipid membrane studied by terahertz time-domain spectroscopy. *Phys. Rev. Lett.* **106**, 158102 (2011).
- [35] Choi, D.-H. *et al.* Dielectric relaxation change of water upon phase transition of a lipid bilayer probed by terahertz time domain spectroscopy. *J. Chem. Phys.* **137**, 175101 (2012).
- [36] Zhao, W., Moilanen, D. E., Fenn, E. E. & Fayer, M. D. Water at the surfaces of aligned phospholipid multibilayer model membranes probed with ultrafast vibrational spectroscopy. *J. Am. Chem. Soc.* **130**, 13927 (2008).
- [37] Kausik, R. & Han, S. Ultrasensitive detection of interfacial water diffusion on lipid vesicle surfaces at molecular length scales. *J. Am. Chem. Soc.* **131**, 18254 (2009).

-
- [38] Song, J., Franck, J. M., Pincus, P., Kim, M. W. & Han, S. Specific ions modulate diffusion dynamics of hydration water on lipid membranes surfaces. *J. Am. Chem. Soc.* **136**, 2642 (2014).
- [39] Cheng, C.-Y., Olijve, L. L. C., Kausik, R. & Han, S. Cholesterol enhances surface water diffusion of phospholipid bilayers. *J. Chem. Phys.* **141**, 22D513 (2014).
- [40] Sovago, M., Vartiainen, E. & Bonn, M. Observation of buried water molecules in phospholipid membranes by surface sum-frequency generation spectroscopy. *J. Chem. Phys.* **131**, 161107 (2009).
- [41] Mondal, J. A., Nihonyanagi, S., Yamaguchi, S. & Tahara, T. Structure and orientation of water at charged lipid monolayer/water interfaces probed by heterodyne-detected vibrational sum frequency generation spectroscopy. *J. Am. Chem. Soc.* **132**, 10656 (2010).
- [42] Chen, X., Hua, W., Huang, Z. & Allen, H. C. Interfacial water structure associated with phospholipid membranes studied by phase-sensitive vibrational sum frequency generation spectroscopy. *J. Am. Chem. Soc.* **132**, 11336 (2010).
- [43] Mondal, J. A., Nihonyanagi, S., Yamaguchi, S. & Tahara, T. Three distinct water structures at a zwitterionic lipid/water interface revealed by heterodyne-detected vibrational sum frequency generation. *J. Am. Chem. Soc.* **134**, 7842 (2012).
- [44] Hua, W., Verreault, D. & Allen, H. C. Solvation of calcium–phosphate head-group complexes at the DPPC/aqueous interface. *ChemPhysChem* **16**, 3910 (2015).
- [45] Raghavan, K., Reddy, M. R. & Berkowitz, M. L. A molecular dynamics study of the structure and dynamics of water between dilauroylphosphatidylethanolamine bilayers. *Langmuir* **8**, 233 (1992).
- [46] Shinoda, W., Shimizu, M. & Okazaki, S. Molecular dynamics study on electrostatic properties of a lipid bilayer: polarization, electrostatic potential, and the effects on structure and dynamics of water near the interfaces. *J. Phys. Chem. B* **102**, 6647 (1998).
- [47] Nagata, Y. & Mukamel, S. Vibrational sum-frequency generation spectroscopy at the water/lipid interface: molecular dynamics simulation study. *J. Am. Chem. Soc.* **132**, 6434 (2010).
- [48] Roy, S., Gruenbaum, S. M. & Skinner, J. L. Theoretical vibrational sum-

- frequency generation spectroscopy of water near lipid and surfactant monolayer interfaces. *J. Chem. Phys.* **141**, 18C502 (2014).
- [49] Ohto, T. *et al.* Lipid carbonyl groups terminate the hydrogen bond network of membrane-bound water. *J. Phys. Chem. Lett.* **6**, 4499 (2015).
- [50] Ishiyama, T., Terada, D. & Morita, A. Hydrogen-bonding structure at zwitterionic lipid/water interface. *J. Phys. Chem. Lett.* **7**, 216 (2016).
- [51] Damodaran, K. V. & Merz Jr, K. M. Head group-water interactions in lipid bilayers: a comparison between DMPC-and DLPE-based lipid bilayers. *Langmuir* **9**, 1179 (1993).
- [52] Alper, H. E., Bassolino-Klimas, D. & Stouch, T. R. The limiting behavior of water hydrating a phospholipid monolayer: a computer simulation study. *J. Chem. Phys.* **99**, 5547 (1993).
- [53] Damodaran, K. V. & Merz Jr, K. M. A comparison of DMPC-and DLPE-based lipid bilayers. *Biophys. J.* **66**, 1076 (1994).
- [54] Pasenkiewicz-Gierula, M., Takaoka, Y., Miyagawa, H., Kitamura, K. & Kusumi, A. Hydrogen bonding of water to phosphatidylcholine in the membrane as studied by a molecular dynamics simulation: location, geometry, and lipid-lipid bridging via hydrogen-bonded water. *J. Phys. Chem. A* **101**, 3677 (1997).
- [55] Pasenkiewicz-Gierula, M., Róg, T., Kitamura, K. & Kusumi, A. Cholesterol effects on the phosphatidylcholine bilayer polar region: a molecular simulation study. *Biophys. J.* **78**, 1376 (2000).
- [56] Bhide, S. Y. & Berkowitz, M. L. Structure and dynamics of water at the interface with phospholipid bilayers. *J. Chem. Phys.* **123**, 224702 (2005).
- [57] Re, S., Nishima, W., Tahara, T. & Sugita, Y. A mosaic of water orientation structures at a neutral zwitterion lipid/water interface revealed by molecular dynamics simulations. *J. Phys. Chem. Lett.* **5**, 4343 (2014).
- [58] Róg, T., Murzyn, K. & Pasenkiewicz-Gierula, M. The dynamics of water at the phospholipid bilayer surface: a molecular dynamics simulation study. *Chem. Phys. Lett.* **352**, 323 (2002).
- [59] Murzyn, K., Zhao, W., Karttunen, M., Kurdziel, M. & Róg, T. Dynamics of water at membrane surfaces: Effect of headgroup structure. *Biointerphases* **1**, 98 (2006).
- [60] Debnath, A., Mukherjee, B., Ayappa, K. G., Maiti, P. K. & Lin, S.-T. Entropy

- and dynamics of water in hydration layers of a bilayer. *J. Chem. Phys.* **133**, 174704 (2010).
- [61] Stepniewski, M., Bunker, A., Pasenkiewicz-Gierula, M., Karttunen, M. & Róg, T. Effects of the lipid bilayer phase state on the water membrane interface. *J. Phys. Chem. B* **114**, 11784 (2010).
- [62] Kagawa, R., Hirano, Y., Taiji, M., Yasuoka, K. & Yasui, M. Dynamic interactions of cations, water and lipids influence on membrane fluidity. *J. Membr. Sci.* **435**, 130 (2013).
- [63] Preston, G. M., Carroll, T. P., Guggino, W. B. & Agre, P. Appearance of water channels in *Xenopus* oocytes expressing red cell CHIP28 protein. *Science* **256**, 385 (1992).
- [64] Ishibashi, K., Kondo, S., Hara, S. & Morishita, Y. The evolutionary aspects of aquaporin family. *Am. J. Physiol. Regul. Integr. Comp. Physiol.* **300**, R566 (2011).
- [65] King, L. S., Kozono, D. & Agre, P. From structure to disease: the evolving tale of aquaporin biology. *Nat. Rev. Mol. Cell Biol.* **5**, 687 (2004).
- [66] Verkman, A. S., Anderson, M. O. & Papadopoulos, M. C. Aquaporins: important but elusive drug targets. *Nat. Rev. Drug Discovery* **13**, 259 (2014).
- [67] Furman, C. S. *et al.* Aquaporin-4 square array assembly: opposing actions of M1 and M23 isoforms. *Proc. Natl. Acad. Sci. USA* **100**, 13609 (2003).
- [68] Höfninger, S. *et al.* Structural features of aquaporin 4 supporting the formation of arrays and junctions in biomembranes. *Biochim. Biophys. Acta* **1818**, 2234 (2012).
- [69] Rojek, A., Praetorius, J., FrØkiaer, J., Nielsen, S. & Fenton, R. A. A current view of the mammalian aquaglyceroporins. *Annu. Rev. Physiol.* **70**, 301 (2008).
- [70] Zeidel, M. L. *et al.* Ultrastructure, pharmacologic inhibition, and transport selectivity of aquaporin chip in proteoliposomes. *Biochemistry* **33**, 1606 (1994).
- [71] Wu, B. & Beitz, E. Aquaporins with selectivity for unconventional permeants. *Cell. Mol. Life Sci.* **64**, 2413 (2007).
- [72] Hub, J. S. & de Groot, B. L. Mechanism of selectivity in aquaporins and aquaglyceroporins. *Proc. Natl. Acad. Sci. USA* **105**, 1198 (2008).
- [73] Oliva, R., Calamita, G., Thornton, J. M. & Pellegrini-Calace, M. Electrostatics of aquaporin and aquaglyceroporin channels correlates with their transport

- selectivity. *Proc. Natl. Acad. Sci. USA* **107**, 4135 (2010).
- [74] Yasui, M. *et al.* Rapid gating and anion permeability of an intracellular aquaporin. *Nature* **402**, 184 (1999).
- [75] Holm, L. M. *et al.* NH_3 and NH_4^+ permeability in aquaporin-expressing *Xenopus* oocytes. *Pflugers Arch.* **450**, 415 (2005).
- [76] Ishibashi, K. New members of mammalian aquaporins: AQP10-AQP12. *Aquaporins* **190**, 251 (2009).
- [77] Gong, X. *et al.* A charge-driven molecular water pump. *Nat. Nanotechnol.* **2**, 709 (2007).
- [78] Corry, B. Water and ion transport through functionalised carbon nanotubes: implications for desalination technology. *Energy Environ. Sci.* **4**, 751 (2011).
- [79] García-Fandiño, R. & Sansom, M. S. P. Designing biomimetic pores based on carbon nanotubes. *Proc. Natl. Acad. Sci. USA* **109**, 6939 (2012).
- [80] Harries, W. E. C., Akhavan, D., Miercke, L. J. W., Khademi, S. & Stroud, R. M. The channel architecture of aquaporin 0 at a 2.2-Å resolution. *Proc. Natl. Acad. Sci. USA* **101**, 14045 (2004).
- [81] Gonen, T. *et al.* Lipid-protein interactions in double-layered two-dimensional AQP0 crystals. *Nature* **438**, 633 (2005).
- [82] Murata, K. *et al.* Structural determinants of water permeation through aquaporin-1. *Nature* **407**, 599 (2000).
- [83] Sui, H., Han, B. G., Lee, J. K., Walian, P. & Jap, B. K. Structural basis of water-specific transport through the AQP1 water channel. *Nature* **414**, 872 (2001).
- [84] Frick, A. *et al.* X-ray structure of human aquaporin 2 and its implications for nephrogenic diabetes insipidus and trafficking. *Proc. Natl. Acad. Sci. USA* **111**, 6305 (2014).
- [85] Ho, J. D. *et al.* Crystal structure of human aquaporin 4 at 1.8 Å and its mechanism of conductance. *Proc. Natl. Acad. Sci. USA* **106**, 7437 (2009).
- [86] Horsefield, R. *et al.* High-resolution X-ray structure of human aquaporin 5. *Proc. Natl. Acad. Sci. USA* **105**, 13327 (2008).
- [87] Savage, D. F., Egea, P. F., Robles-Colmenares, Y., O'Connell III, J. D. & Stroud, R. M. Architecture and selectivity in aquaporins: 2.5 Å X-ray structure of aquaporin Z. *PLoS Biol.* **1**, E72 (2003).
- [88] Fu, D. *et al.* Structure of a glycerol-conducting channel and the basis for its

- selectivity. *Science* **290**, 481 (2000).
- [89] Tajkhorshid, E. *et al.* Control of the selectivity of the aquaporin water channel family by global orientational tuning. *Science* **296**, 525 (2002).
- [90] Newby, Z. E. R. *et al.* Crystal structure of the aquaglyceroporin PfAQP from the malarial parasite *Plasmodium falciparum*. *Nat. Struct. Mol. Biol.* **15**, 619 (2008).
- [91] de Groot, B. L. & Grubmüller, H. Water permeation across biological membranes: mechanism and dynamics of aquaporin-1 and GlpF. *Science* **294**, 2353 (2001).
- [92] Jensen, M. Ø., Tajkhorshid, E. & Schulten, K. Electrostatic tuning of permeation and selectivity in aquaporin water channels. *Biophys. J.* **85**, 2884 (2003).
- [93] De Groot, B. L., Frigato, T., Helms, V. & Grubmüller, H. The mechanism of proton exclusion in the aquaporin-1 water channel. *J. Mol. Biol.* **333**, 279 (2003).
- [94] Zhu, F., Tajkhorshid, E. & Schulten, K. Theory and simulation of water permeation in aquaporin-1. *Biophys. J.* **86**, 50 (2004).
- [95] de Groot, B. L. & Grubmüller, H. The dynamics and energetics of water permeation and proton exclusion in aquaporins. *Curr. Opin. Struct. Biol.* **15**, 176 (2005).
- [96] Hirano, Y. *et al.* Molecular mechanisms of how mercury inhibits water permeation through aquaporin-1: understanding by molecular dynamics simulation. *Biophys. J.* **98**, 1512 (2010).
- [97] Alberga, D. *et al.* A new gating site in human aquaporin-4: Insights from molecular dynamics simulations. *Biochim. Biophys. Acta* **1838**, 3052 (2014).
- [98] Kitchen, P. & Conner, A. C. Control of the aquaporin-4 channel water permeability by structural dynamics of aromatic/arginine selectivity filter residues. *Biochemistry* **54**, 6753 (2015).
- [99] Yool, A. J. & Weinstein, A. M. New roles for old holes: ion channel function in aquaporin-1. *Physiology* **17**, 68 (2002).
- [100] Yu, J., Yool, A., Schulten, K. & Tajkhorshid, E. Mechanism of gating and ion conductivity of a possible tetrameric pore in aquaporin-1. *Structure* **14**, 1411 (2006).
- [101] Herrera, M. & Garvin, J. L. Aquaporins as gas channels. *Pflugers Arch. Eur.*

- J. Physiol.* **462**, 623 (2011).
- [102] Gravelle, S. *et al.* Optimizing water permeability through the hourglass shape of aquaporins. *Proc. Natl. Acad. Sci. USA* **110**, 16367 (2013).
- [103] Guan, X.-G. *et al.* NPA motifs play a key role in plasma membrane targeting of aquaporin-4. *IUBMB Life* **62**, 222 (2010).
- [104] Beitz, E., Wu, B., Holm, L. M., Schultz, J. E. & Zeuthen, T. Point mutations in the aromatic/arginine region in aquaporin 1 allow passage of urea, glycerol, ammonia, and protons. *Proc. Natl. Acad. Sci. USA* **103**, 269 (2006).
- [105] Burykin, A. & Warshel, A. What really prevents proton transport through aquaporin? Charge self-energy versus proton wire proposals. *Biophys. J.* **85**, 3696 (2003).
- [106] Ilan, B., Tajkhorshid, E., Schulten, K. & Voth, G. A. The mechanism of proton exclusion in aquaporin channels. *Proteins* **55**, 223 (2004).
- [107] Chakrabarti, N., Tajkhorshid, E., Roux, B. & Pomès, R. Molecular basis of proton blockage in aquaporins. *Structure* **12**, 65 (2004).
- [108] Jensen, M. Ø., Röthlisberger, U. & Rovira, C. Hydroxide and proton migration in aquaporins. *Biophys. J.* **89**, 1744 (2005).
- [109] Li, H. *et al.* Enhancement of proton conductance by mutations of the selectivity filter of aquaporin-1. *J. Mol. Biol.* **407**, 607 (2011).
- [110] Eriksson, U. K. *et al.* Subangstrom resolution X-ray structure details aquaporin-water interactions. *Science* **340**, 1346 (2013).
- [111] Verlet, L. Computer “experiments” on classical fluids. I. Thermodynamical properties of Lennard-Jones molecules. *Phys. Rev.* **159**, 98 (1967).
- [112] Swope, W. C., Andersen, H. C., Berens, P. H. & Wilson, K. R. A computer simulation method for the calculation of equilibrium constants for the formation of physical clusters of molecules: Application to small water clusters. *J. Chem. Phys.* **76**, 637 (1982).
- [113] Ryckaert, J. P., Ciccotti, G. & Berendsen, H. J. C. Numerical integration of the Cartesian equations of motion of a system with constraints: molecular dynamics of n-alkanes. *J. Comput. Phys.* **23**, 327 (1977).
- [114] Andersen, H. RATTLE: A “Velocity” version of the SHAKE algorithm for molecular dynamics calculations. *J. Comput. Phys.* **52**, 24–34 (1983).
- [115] Berendsen, H. J. C., Postma, J. P. M., van Gunsteren, W. F., DiNola, A. & Haak, J. R. Molecular dynamics with coupling to an external bath. *J. Chem.*

-
- Phys.* **81**, 3684 (1984).
- [116] Jones, J. E. On the determination of molecular fields. II. From the equation of state of a gas. *Proc. R. Soc. Lond. A* **106**, 463 (1924).
- [117] Ewald, P. P. Die berechnung optischer und elektrostatischer gitterpotentiale. *Ann. Phys.* **369**, 253 (1921).
- [118] Berntsen, P., Svanberg, C. & Swenson, J. Interplay between hydration water and headgroup dynamics in lipid bilayers. *J. Phys. Chem. B* **115**, 1825 (2011).
- [119] Debnath, A., Ayappa, K. G. & Maiti, P. K. Simulation of influence of bilayer melting on dynamics and thermodynamics of interfacial water. *Phys. Rev. Lett.* **110**, 018303 (2013).
- [120] Rocchi, C., Bizzarri, A. R. & Cannistraro, S. Water dynamical anomalies evidenced by molecular-dynamics simulations at the solvent-protein interface. *Phys. Rev. E* **57**, 3315 (1998).
- [121] García, A. E. & Hummer, G. Water penetration and escape in proteins. *Proteins* **38**, 261 (2000).
- [122] Oleinikova, A., Smolin, N., Brovchenko, I., Geiger, A. & Winter, R. Formation of spanning water networks on protein surfaces via 2D percolation transition. *J. Phys. Chem. B* **109**, 1988 (2005).
- [123] Brovchenko, I., Krukau, A., Oleinikova, A. & Mazur, A. K. Water clustering and percolation in low hydration DNA shells. *J. Phys. Chem. B* **111**, 3258 (2007).
- [124] Miyaguchi, T. Escape time statistics for mushroom billiards. *Phys. Rev. E* **75**, 066215 (2007).
- [125] Scher, H. & Montroll, E. W. Anomalous transit-time dispersion in amorphous solids. *Phys. Rev. B* **12**, 2455 (1975).
- [126] Brokmann, X. *et al.* Statistical aging and nonergodicity in the fluorescence of single nanocrystals. *Phys. Rev. Lett.* **90**, 120601 (2003).
- [127] Galland, C. *et al.* Two types of luminescence blinking revealed by spectro-electrochemistry of single quantum dots. *Nature* **479**, 203 (2011).
- [128] Wong, I. Y. *et al.* Anomalous diffusion probes microstructure dynamics of entangled F-Actin networks. *Phys. Rev. Lett.* **92**, 178101 (2004).
- [129] van Hijkoop, V. J., Dammers, A. J., Malek, K. & Coppens, M.-O. Water diffusion through a membrane protein channel: A first passage time approach. *J. Chem. Phys.* **127**, 085101 (2007).

- [130] Weigel, A. V., Simon, B., Tamkun, M. M. & Krapf, D. Ergodic and nonergodic processes coexist in the plasma membrane as observed by single-molecule tracking. *Proc. Natl. Acad. Sci. USA* **108**, 6438 (2011).
- [131] Bouchaud, J. P. Weak ergodicity breaking and aging in disordered systems. *J. Phys. I* **2**, 1705 (1992).
- [132] Bardou, F., Bouchaud, J. P., Aspect, A. & Tannoudji, C. C. *Lévy statistics and laser cooling: how rare events bring atoms to rest* (Cambridge University Press, 2002).
- [133] Bouchaud, J. P. & Georges, A. Anomalous diffusion in disordered media: statistical mechanisms, models and physical applications. *Phys. Rep.* **195**, 127 (1990).
- [134] Goychuk, I. & Hänggi, P. Ion channel gating: A first-passage time analysis of the Kramers type. *Proc. Natl. Acad. Sci. USA* **99**, 3552 (2002).
- [135] Goychuk, I. & Hänggi, P. Anomalous escape governed by thermal $1/f$ noise. *Phys. Rev. Lett.* **99**, 200601 (2007).
- [136] Rappolt, M., Hickel, A., Bringezu, F. & Lohner, K. Mechanism of the lamellar/inverse hexagonal phase transition examined by high resolution X-ray diffraction. *Biophys. J.* **84**, 3111 (2003).
- [137] Leekumjorn, S. & Sum, A. K. Molecular characterization of gel and liquid-crystalline structures of fully hydrated POPC and POPE bilayers. *J. Phys. Chem. B* **111**, 6026 (2007).
- [138] Gullingsrud, J. & Schulten, K. Lipid bilayer pressure profiles and mechanosensitive channel gating. *Biophys. J.* **86**, 3496 (2004).
- [139] Gurtovenko, A. A. & Vattulainen, I. Effect of NaCl and KCl on phosphatidylcholine and phosphatidylethanolamine lipid membranes: insight from atomic-scale simulations for understanding salt-induced effects in the plasma membrane. *J. Phys. Chem. B* **112**, 1953 (2008).
- [140] Case, D. A. *et al.* *AMBER 10* (Univ. Calif. San Francisco, 2008).
- [141] Redner, S. *A guide to first-passage processes* (Cambridge University Press, 2001).
- [142] Zhang, Z. & Berkowitz, M. L. Orientational dynamics of water in phospholipid bilayers with different hydration levels. *J. Phys. Chem. B* **113**, 7676 (2009).
- [143] Mazza, M. G., Giovambattista, N., Starr, F. W. & Stanley, H. E. Relation between rotational and translational dynamic heterogeneities in water. *Phys.*

-
- Rev. Lett.* **96**, 057803 (2006).
- [144] Weiss, M., Hashimoto, H. & Nilsson, T. Anomalous protein diffusion in living cells as seen by fluorescence correlation spectroscopy. *Biophys. J.* **84**, 4043 (2003).
- [145] Golding, I. & Cox, E. C. Physical nature of bacterial cytoplasm. *Phys. Rev. Lett.* **96**, 098102 (2006).
- [146] Jeon, J.-H. *et al.* *In Vivo* anomalous diffusion and weak ergodicity breaking of lipid granules. *Phys. Rev. Lett.* **106**, 048103 (2011).
- [147] Tabei, S. M. A. *et al.* Intracellular transport of insulin granules is a subordinated random walk. *Proc. Natl. Acad. Sci. USA* **110**, 4911 (2013).
- [148] Metzler, R., Jeon, J.-H., Cherstvy, A. G. & Barkai, E. Anomalous diffusion models and their properties: non-stationarity, non-ergodicity, and ageing at the centenary of single particle tracking. *Phys. Chem. Chem. Phys.* **16**, 24128 (2014).
- [149] Metzler, R. & Klafter, J. The random walk's guide to anomalous diffusion: a fractional dynamics approach. *Phys. Rep.* **339**, 1 (2000).
- [150] Kolmogorov, A. N. The wiener spiral and some other interesting curves in hilbert space. *Dokl Acad Sci USSR* **26**, 115 (1940).
- [151] Mandelbrot, B. B. & Van Ness, J. W. Fractional brownian motions, fractional noises and applications. *SIAM Rev.* **10**, 422 (1968).
- [152] Ben-Avraham, D. & Havlin, S. *Diffusion and reactions in fractals and disordered systems* (Cambridge Univ Pr, 2000).
- [153] He, Y., Burov, S., Metzler, R. & Barkai, E. Random time-scale invariant diffusion and transport coefficients. *Phys. Rev. Lett.* **101**, 058101 (2008).
- [154] Lubelski, A., Sokolov, I. M. & Klafter, J. Nonergodicity mimics inhomogeneity in single particle tracking. *Phys. Rev. Lett.* **100**, 250602 (2008).
- [155] Miyaguchi, T. & Akimoto, T. Ergodic properties of continuous-time random walks: Finite-size effects and ensemble dependences. *Phys. Rev. E* **87**, 032130 (2013).
- [156] Barkai, E. Aging in subdiffusion generated by a deterministic dynamical system. *Phys. Rev. Lett.* **90**, 104101 (2003).
- [157] Schulz, J. H. P., Barkai, E. & Metzler, R. Aging effects and population splitting in single-particle trajectory averages. *Phys. Rev. Lett.* **110**, 020602 (2013).

- [158] Miyaguchi, T. & Akimoto, T. Ultraslow convergence to ergodicity in transient subdiffusion. *Phys. Rev. E* **83**, 062101 (2011).
- [159] Weber, S. C., Spakowitz, A. J. & Theriot, J. A. Bacterial chromosomal loci move subdiffusively through a viscoelastic cytoplasm. *Phys. Rev. Lett.* **104**, 238102 (2010).
- [160] Deng, W. & Barkai, E. Ergodic properties of fractional brownian-langevin motion. *Phys. Rev. E* **79**, 011112 (2009).
- [161] Jeon, J.-H. & Metzler, R. Fractional brownian motion and motion governed by the fractional langevin equation in confined geometries. *Phys. Rev. E* **81**, 021103 (2010).
- [162] Jeon, J.-H. & Metzler, R. Inequivalence of time and ensemble averages in ergodic systems: Exponential versus power-law relaxation in confinement. *Phys. Rev. E* **85**, 021147 (2012).
- [163] Jeon, J.-H., Leijnse, N., Oddershede, L. B. & Metzler, R. Anomalous diffusion and power-law relaxation of the time averaged mean squared displacement in worm-like micellar solutions. *New J. Phys.* **15**, 045011 (2013).
- [164] Kursawe, J., Schulz, J. & Metzler, R. Transient aging in fractional brownian and langevin-equation motion. *Phys. Rev. E* **88**, 062124 (2013).
- [165] Jeon, J. H. & Metzler, R. Analysis of short subdiffusive time series: scatter of the time-averaged mean-squared displacement. *J. Phys. A: Math. Theor.* **43**, 252001 (2010).
- [166] Miyaguchi, T. & Akimoto, T. Intrinsic randomness of transport coefficient in subdiffusion with static disorder. *Phys. Rev. E* **83**, 031926 (2011).
- [167] Tejedor, V. & Metzler, R. Anomalous diffusion in correlated continuous time random walks. *J. Phys. A* **43**, 082002 (2010).
- [168] Magdziarz, M., Metzler, R., Szczotka, W. & Zebrowski, P. Correlated continuous-time random walks in external force fields. *Phys. Rev. E* **85**, 051103 (2012).
- [169] Cherstvy, A. G., Chechkin, A. V. & Metzler, R. Anomalous diffusion and ergodicity breaking in heterogeneous diffusion processes. *New J. Phys.* **15**, 083039 (2013).
- [170] Lomholt, M. A., Lizana, L., Metzler, R. & Ambjörnsson, T. Microscopic origin of the logarithmic time evolution of aging processes in complex systems. *Phys. Rev. Lett.* **110**, 208301 (2013).

-
- [171] Akimoto, T. & Miyaguchi, T. Distributional ergodicity in stored-energy-driven lévy flights. *Phys. Rev. E* **87**, 062134 (2013).
- [172] Das, J., Flenner, E. & Kosztin, I. Anomalous diffusion of water molecules in hydrated lipid bilayers. *J. Chem. Phys.* **139**, 065102 (2013).
- [173] von Hansen, Y., Gekle, S. & Netz, R. R. Anomalous anisotropic diffusion dynamics of hydration water at lipid membranes. *Phys. Rev. Lett.* **111**, 118103 (2013).
- [174] Klauda, J. B. *et al.* Update of the CHARMM all-atom additive force field for lipids: validation on six lipid types. *J. Phys. Chem. B* **114**, 7830 (2010).
- [175] MacKerell, A. D. *et al.* All-atom empirical potential for molecular modeling and dynamics studies of proteins. *J. Phys. Chem. B* **102**, 3586 (1998).
- [176] Jorgensen, W. L., Chandrasekhar, J., Madura, J. D., Impey, R. W. & Klein, M. L. Comparison of simple potential functions for simulating liquid water. *J. Chem. Phys.* **79**, 926 (1983).
- [177] Kalé, L. *et al.* NAMD2: Greater scalability for parallel molecular dynamics. *J. Comput. Phys.* **151**, 283 (1999).
- [178] Flenner, E., Das, J., Rheinstädter, M. C. & Kosztin, I. Subdiffusion and lateral diffusion coefficient of lipid atoms and molecules in phospholipid bilayers. *Phys. Rev. E* **79**, 011907 (2009).
- [179] Kneller, G. R., Baczynski, K. & Pasenkiewicz-Gierula, M. Communication: Consistent picture of lateral subdiffusion in lipid bilayers: Molecular dynamics simulation and exact results. *J. Chem. Phys.* **135**, 141105 (2011).
- [180] Yamamoto, E., Kalli, A. C., Akimoto, T., Yasuoka, K. & Sansom, M. S. P. Anomalous dynamics of a lipid recognition protein on a membrane surface. *Sci. Rep.* **5**, 18245 (2015).
- [181] Tejedor, V. *et al.* Quantitative analysis of single particle trajectories: Mean maximal excursion method. *Biophys. J.* **98**, 1364 (2010).
- [182] Jeon, J.-H., Barkai, E. & Metzler, R. Noisy continuous time random walks. *J. Chem. Phys.* **139**, 121916 (2013).
- [183] Grossman, M. *et al.* Correlated structural kinetics and retarded solvent dynamics at the metalloprotease active site. *Nat. Struct. Mol. Biol.* **18**, 1102 (2011).
- [184] Guigas, G. & Weiss, M. Sampling the cell with anomalous diffusion-the discovery of slowness. *Biophys. J.* **94**, 90 (2008).

- [185] Yang, H. *et al.* Protein conformational dynamics probed by single-molecule electron transfer. *Science* **302**, 262 (2003).
- [186] Min, W., Luo, G., Cherayil, B. J., Kou, S. C. & Xie, X. S. Observation of a power-law memory kernel for fluctuations within a single protein molecule. *Phys. Rev. Lett.* **94**, 198302 (2005).
- [187] Martínez, I. A., Raj, S. & Petrov, D. Colored noise in the fluctuations of an extended DNA molecule detected by optical trapping. *Euro. Biophys. J.* **41**, 99 (2012).
- [188] Li, W. & Kaneko, K. Long-range correlation and partial $1/f^\alpha$ spectrum in a noncoding DNA sequences. *Europhys. Lett.* **17**, 655 (1992).
- [189] Bizzarri, A. R. & Cannistraro, S. $1/f^\alpha$ noise in the dynamic force spectroscopy curves signals the occurrence of biorecognition. *Phys. Rev. Lett.* **110**, 048104 (2013).
- [190] Bezrukov, S. M. & Winterhalter, M. Examining noise sources at the single-molecule level: $1/f$ noise of an open maltoporin channel. *Phys. Rev. Lett.* **85**, 202 (2000).
- [191] Mercik, S. & Weron, K. Stochastic origins of the long-range correlations of ionic current fluctuations in membrane channels. *Phys. Rev. E* **63**, 051910 (2001).
- [192] Siwy, Z. & Fuliński, A. Origin of $1/f^\alpha$ noise in membrane channel currents. *Phys. Rev. Lett.* **89**, 158101 (2002).
- [193] Tasserit, C., Koutsioubas, A., Lairez, D., Zalczer, G. & Clochard, M.-C. Pink noise of ionic conductance through single artificial nanopores revisited. *Phys. Rev. Lett.* **105**, 260602 (2010).
- [194] Lowen, S. B. & Teich, M. C. Fractal renewal processes generate $1/f$ noises. *Phys. Rev. E* **47**, 992–1001 (1993).
- [195] Godrèche, C. & Luck, J. M. Statistics of the occupation time of renewal processes. *J. Stat. Phys.* **104**, 489 (2001).
- [196] Davidsen, J. & Schuster, H. G. Simple model for $1/f^\alpha$ noises. *Phys. Rev. E* **65**, 026120 (2002).
- [197] Manneville, P. Intermittency, self-similarity and $1/f$ spectrum in dissipative dynamical systems. *J. Physique* **41**, 1235 (1980).
- [198] Procaccia, I. & Schuster, H. Functional renormalization-group theory of universal $1/f$ noise in dynamical systems. *Phys. Rev. A* **28**, 1210 (1983).

-
- [199] Aizawa, Y. On the f^{-1} spectral chaos. *Prog. Theor. Phys.* **72**, 659 (1984).
- [200] Geisel, T., Nierwetberg, J. & Zacherl, A. Accelerated diffusion in josephson junctions and related chaotic systems. *Phys. Rev. Lett.* **54**, 616 (1985).
- [201] Kuno, M., Fromm, D. P., Hamann, H. F., Gallagher, A. & Nesbitt, D. J. Nonexponential “blinking” kinetics of single CdSe quantum dots: A universal power law behavior. *J. Chem. Phys.* **112**, 3117 (2000).
- [202] Margolin, G. & Barkai, E. Nonergodicity of a time series obeying Lévy statistics. *J. Stat. Phys.* **122**, 137 (2006).
- [203] Niemann, M., Kantz, H. & Barkai, E. Fluctuations of $1/f$ noise and the low-frequency cutoff paradox. *Phys. Rev. Lett.* **110**, 140603 (2013).
- [204] Akimoto, T. & Aizawa, Y. Subexponential instability in one-dimensional maps implies infinite invariant measure. *Chaos* **20**, 033110 (2010).
- [205] Akimoto, T. Generalized arcsine law and stable law in an infinite measure dynamical system. *J. Stat. Phys.* **132**, 171 (2008).
- [206] Berendsen, H. J. C., Postma, J. P. M., van Gunsteren, W. F. & Hermans, J. Interaction models for water in relation to protein hydration. *Intermolecular Forces* **14**, 331 (1981).
- [207] Hess, B., Kutzner, C., Van Der Spoel, D. & Lindahl, E. GROMACS 4: Algorithms for highly efficient, load-balanced, and scalable molecular simulation. *J. Chem. Theory Comput.* **4**, 435 (2008).
- [208] Oostenbrink, C., Villa, A., Mark, A. E. & Van Gunsteren, W. F. A biomolecular force field based on the free enthalpy of hydration and solvation: The GROMOS force-field parameter sets 53A5 and 53A6. *J. Comput. Chem.* **25**, 1656 (2004).
- [209] Parrinello, M. & Rahman, A. Polymorphic transitions in single crystals: A new molecular dynamics method. *J. Appl. Phys.* **52**, 7182 (1981).
- [210] Bussi, G., Donadio, D. & Parrinello, M. Canonical sampling through velocity rescaling. *J. Chem. Phys.* **126**, 014101 (2007).
- [211] Hess, B., Bekker, H., Berendsen, H. J. C. & Fraaije, J. G. E. M. LINCS: A linear constraint solver for molecular simulations. *J. Comput. Chem.* **18**, 1463 (1997).
- [212] Laage, D. & Hynes, J. A molecular jump mechanism of water reorientation. *Science* **311**, 832 (2006).
- [213] Sadegh, S., Barkai, E. & Krapf, D. $1/f$ noise for intermittent quantum dots

- exhibits non-stationarity and critical exponents. *New J. Phys.* **16**, 113054 (2014).
- [214] Akimoto, T., Hasumi, T. & Aizawa, Y. Characterization of intermittency in renewal processes: Application to earthquakes. *Phys. Rev. E* **81**, 031133 (2010).
- [215] Stefani, F. D., Zhong, X., Knoll, W., Han, M. & Kreiter, M. Memory in quantum-dot photoluminescence blinking. *New J. Phys.* **7**, 197 (2005).
- [216] Stefani, F. D., Hoogenboom, J. P. & Barkai, E. Beyond quantum jumps: Blinking nanoscale light emitters. *Phys. Today* **62**, 34 (2009).
- [217] Godec, A. & Merzel, F. Physical origin underlying the entropy loss upon hydrophobic hydration. *J. Am. Chem. Soc.* **134**, 17574 (2012).
- [218] Godec, A. c. v., Smith, J. C. & Merzel, F. Soft collective fluctuations governing hydrophobic association. *Phys. Rev. Lett.* **111**, 127801 (2013).
- [219] Gongadze, E. *et al.* Ions and water molecules in an electrolyte solution in contact with charged and dipolar surfaces. *Electrochim. Acta* **126**, 42 (2014).
- [220] Berezhkovskii, A. & Hummer, G. Single-file transport of water molecules through a carbon nanotube. *Phys. Rev. Lett.* **89**, 064503 (2002).
- [221] Peng, C.-K. *et al.* Mosaic organization of DNA nucleotides. *Phys. Rev. E* **49**, 1685 (1994).
- [222] Chen, H., Wu, Y. & Voth, G. A. Origins of proton transport behavior from selectivity domain mutations of the aquaporin-1 channel. *Biophys. J.* **90**, L73 (2006).
- [223] Goychuk, I. Viscoelastic subdiffusion: From anomalous to normal. *Phys. Rev. E* **80**, 046125 (2009).
- [224] Lu, H. *et al.* Controllable transport of water through nanochannel by ratchet-like mechanism. *J. Chem. Phys.* **136**, 174511 (2012).
- [225] Kou, J. *et al.* A vibration-charge-induced unidirectional transport of water molecules in confined nanochannels. *Soft Matter* **8**, 12111 (2012).